

A structure-preserving staggered semi-implicit finite volume scheme for continuum mechanics

W. Boscheri^a, M. Dumbser^{b,*}, M. Ioriatti^b, I. Peshkov^b, E. Romenski^{b,c}

^aDepartment of Mathematics and Computer Science, University of Ferrara, via Machiavelli 30, I-44121 Ferrara, Italy

^bDepartment of Civil, Environmental and Mechanical Engineering, University of Trento, Via Mesiano 77, I-38123 Trento, Italy

^cSobolev Institute of Mathematics, 4 Acad. Koptyug Avenue, 630090 Novosibirsk, Russia

Abstract

We propose a new *pressure-based* structure-preserving (SP) and quasi asymptotic preserving (AP) staggered semi-implicit finite volume scheme for the unified first order hyperbolic formulation of continuum mechanics [1], which goes back to the pioneering work of Godunov [2] and further work of Godunov and Romenski [3] and Peshkov & Romenski [4]. The unified model is based on the theory of symmetric-hyperbolic and thermodynamically compatible (SHTC) systems [2, 5] and includes the description of elastic and elasto-plastic solids in the nonlinear large-strain regime as well as viscous and inviscid heat-conducting fluids, which correspond to the stiff relaxation limit of the model. In the absence of relaxation source terms, the homogeneous PDE system is endowed with two stationary linear differential constraints (*involutions*), which require the curl of distortion field and the curl of the thermal impulse to be zero for all times. In the stiff relaxation limit, the unified model tends asymptotically to the compressible Navier-Stokes equations.

The new structure-preserving scheme presented in this paper can be proven to be *exactly curl-free* for the homogeneous part of the PDE system, i.e. in the absence of relaxation source terms. We furthermore prove that the scheme is quasi asymptotic preserving in the stiff relaxation limit, in the sense that the numerical scheme reduces to a consistent second order accurate discretization of the compressible Navier-Stokes equations when the relaxation times tend to zero. Last but not least, the proposed scheme is suitable for the simulation of all Mach number flows thanks to its conservative formulation and the implicit discretization of the pressure terms.

Keywords: staggered semi-implicit finite volume schemes, structure-preserving curl-free schemes, asymptotic preserving schemes, pressure-based all Mach number flow solver, computational fluid and solid mechanics, symmetric hyperbolic and thermodynamically compatible systems (SHTC)

1. Introduction

The need of structure-preserving schemes for hyperbolic conservation laws with involution constraints is very well known in the context of numerical methods for the solution of the Maxwell and MHD equations in the time domain. There, the involution consists in the divergence-free condition of the magnetic field, which is a stationary extra conservation law that is automatically satisfied by the governing PDE system for all times if the initial magnetic field was divergence-free. Exactly divergence-free schemes (so-called constrained transport schemes) usually employ a *staggered mesh*, see the pioneering work of Yee [6], where in two space-dimensions the edge-normal components of the magnetic field are directly stored and evolved on the edges of the primary control volumes at the aid of an electric field that is defined in the vertices of each edge. For further developments in the context of constrained transport schemes, see e.g. the following list of references, which does not pretend to be complete, [7, 8, 9, 10, 11, 12]. An

*Corresponding author

Email addresses: walter.boscheri@unife.it (W. Boscheri), michael.dumbser@unitn.it (M. Dumbser), matteo.ioriatti@unitn.it (M. Ioriatti), ilya.peshkov@unitn.it (I. Peshkov), evrom@math.nsc.ru (E. Romenski)

alternative to the use of exactly divergence-free schemes is the use of *divergence cleaning* techniques, which add extra terms to the governing PDE system. This can be either achieved by the so-called Powell terms [13], which are actually based on the symmetric form of the MHD equations found by Godunov in 1972, see [14], or the hyperbolic generalized Lagrangian multiplier (GLM) approach of Munz *et al.* [15, 16].

The governing PDE system discussed in the present paper goes back to [2, 3, 4, 1] and in the absence of relaxation source terms it is also endowed with two involution constraints, but here the *curl* of some quantities is required to be zero for all times rather than the *divergence*. Much less is known about exactly or approximately curl preserving finite volume schemes, probably because this type of involution is not yet as frequent as the well-known divergence constraints on the magnetic and electric field in computational electromagnetics. It definitely arises in nonlinear hyperelasticity, see e.g. the discussions in [5, 17, 18]. A rather general framework for the construction of structure-preserving schemes (including curl-preserving methods) was developed by Hyman and Shashkov [19] and Jeltsch and Torrilhon [20, 21]. Further work on mimetic and structure-preserving finite difference schemes can be found e.g. in [22, 23, 24]. For curl-free wavelets the reader is referred to [25], while compatible finite elements are discussed, for example, in [26, 27, 28, 29, 30, 31, 32]. The GLM approach of Munz *et al.* has been very recently also generalized to PDE with curl involutions in [33, 34], while a comparison of different approaches to treat curl-free PDE has been provided in [35].

Common to almost all the previously-mentioned exactly structure-preserving schemes is the fact that they require the use of a *staggered grid* in order to provide natural and compatible definitions of the discrete curl, gradient and divergence operators. But staggered grids are not only used in the context of structure-preserving schemes. They are also widely used in the context of semi-implicit schemes for the solution of the incompressible Navier-Stokes equations since the pioneering work of Harlow and Welch [36]. For a non-exhaustive overview of some of the most important contributions concerning pressure-based staggered semi-implicit finite difference schemes for the Navier-Stokes and shallow water equations the reader is referred to [37, 38, 39, 40, 41, 42, 43, 44, 45, 46, 47, 48, 49]. For a new family of staggered hybrid finite volume / finite element schemes for incompressible and weakly compressible flows, see e.g. [50, 51] and references therein. It is therefore a very natural choice to employ staggered meshes when constructing a new semi-implicit structure-preserving scheme, which is the declared objective of this paper.

As already stated before, staggered semi-implicit schemes are typically used in the context of incompressible or low Mach number flows. The first semi-implicit scheme for the compressible Euler equations was the method of Casulli and Greenspan [52], but this scheme was not conservative and thus not suitable for the simulation of shock waves. For the compressible high Mach number flows, usually explicit density-based Godunov-type finite volume schemes are employed, see [53, 54, 55, 56, 57, 58, 59, 60, 61, 62], because of their intrinsic conservation property that allows the correct computation of shock waves. Up to now, semi-implicit methods are only rarely used for the simulation of compressible flows with shock waves, but some recent developments can be found in [63, 64, 65, 66, 67, 68, 69], where new families of *conservative* pressure-based semi-implicit schemes were introduced and which are therefore also suitable for shock waves and compressible flows at all Mach numbers. However, to the best knowledge of the authors currently there exists no numerical scheme for the model [1] (called GPR model in the following) that satisfies all involution constraints exactly on the discrete level, which is furthermore asymptotic preserving (AP) for vanishing relaxation times and which is suitable for all Mach number flows. A very recent all speed scheme for nonlinear hyperelasticity can be found in [70]. For a review about Lagrangian and Eulerian schemes for nonlinear hyperelasticity, see [3, 71, 5, 72, 73, 74, 75, 76, 4, 77, 1, 78, 79, 80, 81, 82, 83, 84, 85, 86, 87, 88, 89].

The declared aim of this paper is therefore to develop a new, conservative, pressure-based semi-implicit finite volume method on staggered meshes for the solution of the model (1), which is at the same time structure-preserving (SP) for all involution constraints, (quasi) asymptotic-preserving (AP) in the stiff relaxation limit and suitable for all Mach number flows. It is well-known that explicit density-based solvers become inefficient and inaccurate in the low Mach number regime and for these reasons an implicit time discretization is needed. However, discretizing all terms implicitly would in general lead to a *highly nonlinear* non-symmetric system with a large number of unknowns (density, velocity, pressure, distortion field and thermal impulse), for which convergence is very difficult to control. Therefore, the new structure-preserving semi-implicit finite volume (SPSIFV) method proposed in this paper uses instead (i) an explicit discretization for all nonlinear convective terms, (ii) a compatible and structure-preserving explicit discretization for the distortion field and the thermal impulse on a *vertex-based* staggered mesh, (iii) while an

implicit discretization is only employed for the pressure terms and for the stiff algebraic relaxation source terms. This judicious combination leads in the end to only one *mildly-nonlinear* and *symmetric positive definite* system for the fluid pressure as the only unknown. The properties of the resulting pressure system allow the use of the Newton-type techniques of Casulli *et al.* [90, 91, 92, 93], for which convergence has been *rigorously proven*. Due to the implicit pressure terms, the time step of our new scheme is only restricted by the fluid velocity and characteristic wave speeds of shear and heat wave propagation, and not by the adiabatic sound speed. For this reason, the method proposed in this paper is a true structure-preserving *all Mach number* flow solver.

We underline that a new family of *explicit* high order curl-preserving Godunov-type finite volume schemes, which makes use of an *edge-based* staggering in combination with a high order curl-preserving WENO reconstruction and multi-dimensional Riemann solvers, has been very recently introduced by Balsara *et al.* in [94], while the method proposed in the present paper makes use of a *vertex-based* staggering and a *semi-implicit* pressure-based formulation.

The rest of the paper is organized as follows: in Section 2 we briefly recall the unified first order hyperbolic GPR model of continuum mechanics. In Section 3 we present the new staggered semi-implicit structure-preserving finite volume scheme. The mathematical properties of the numerical method are analyzed in Section 4 and computational results for a large set of test problems are shown in Section 5. The paper closes with Section 6, in which we give some concluding remarks and an outlook to future work.

2. Unified first order hyperbolic model of continuum mechanics

2.1. Governing PDE system

The unified first order hyperbolic GPR model of continuum mechanics including heat conduction reads as follows, see also [5, 4, 1]

$$\frac{\partial \rho}{\partial t} + \frac{\partial(\rho v_k)}{\partial x_k} = 0, \quad (1a)$$

$$\frac{\partial \rho v_i}{\partial t} + \frac{\partial(\rho v_i v_k + p \delta_{ik} - \sigma_{ik})}{\partial x_k} = 0, \quad (1b)$$

$$\frac{\partial A_{ik}}{\partial t} + \frac{\partial(A_{im} v_m)}{\partial x_k} + v_m \left(\frac{\partial A_{ik}}{\partial x_m} - \frac{\partial A_{im}}{\partial x_k} \right) = -\frac{\psi_{ik}}{\theta_1(\tau_1)}, \quad (1c)$$

$$\frac{\partial J_k}{\partial t} + \frac{\partial(J_m v_m + T)}{\partial x_k} + v_m \left(\frac{\partial J_k}{\partial x_m} - \frac{\partial J_m}{\partial x_k} \right) = -\frac{H_k}{\theta_2(\tau_2)}, \quad (1d)$$

$$\frac{\partial \rho E}{\partial t} + \frac{\partial(v_k \rho E + v_i(p \delta_{ik} - \sigma_{ik}) + q_k)}{\partial x_k} = 0. \quad (1e)$$

Here, ρ is the mass density, v_i is the velocity field, A_{ik} is the distortion field (which is a basis triad and thus transforms as a set of three vectors and not as a tensor under coordinate transforms), J_k is the thermal impulse density (it has the SI units $\text{K} \cdot \frac{\text{s}}{\text{m}}$), ρE is the total energy density, p is the fluid pressure, σ_{ik} is the stress tensor that contains shear stress as well as thermal stresses, and q_k is the heat flux.

Furthermore, the energy potential E plays the role of the closure for system (1). Thus, thermodynamic consistency of (1) requires that the pressure be $p = \rho^2 E_\rho$, the temperature $T = E_S$, the stress tensor

$$\sigma_{ik} = -\rho A_{ji} E_{A_{jk}} - \rho J_i E_{J_k} = -\rho A_{ji} \psi_{jk} - \rho J_i H_k, \quad (2)$$

$\psi_{ik} := E_{A_{ik}}$, $H_k := E_{J_k}$, and the heat flux

$$q_k = \rho E_S E_{J_k} = \rho T H_k, \quad (3)$$

where E_ρ , E_S , $E_{A_{ik}}$, etc. denote partial derivative of E with respect to the state variables $E_\rho = \partial E / \partial \rho$, $E_S = \partial E / \partial S$, $E_{A_{ik}} = \partial E / \partial A_{ik}$, etc. Therefore, to close system (1), one has to provide the specific expression for the energy E .

We remark that the thermal impulse equation (1d) is different from the one used in our previous papers [1, 95]. Both equations, although they look slightly different, are compatible with the Fourier law of heat conduction in the equilibrium limit (small relaxation times $\tau_2 \rightarrow 0$). The thermal impulse equation [1, 95] has a convenient divergence form (i.e. it can be written as four-divergence of a vector field) and free of involution constraints which is good for numerical purposes, while the equation (1d) can not be represented in a fully conservative flux divergence form. Nevertheless, the heat conduction equation (1d) proposed by Romenski in [5] should be considered more preferable from the theoretical standpoint. First of all, it admits a variational formulation [79], while the thermal impulse equation from [1, 95] does not. Second, (1d) is consistent with the Hamiltonian formulation for non-equilibrium thermodynamics known as GENERIC [96, 97], see [79]. This implies that (1d) should be more advantageous for describing heat transfer in non-equilibrium settings. Last, the equations with exactly the same structure of differential terms as (1d) and thus, with the curl involution appear in many other physical settings, e.g. multi-phase flows [98], continuum modeling of surface tension [99], and hyperbolic reformulation of the nonlinear Schrödinger's equation [100].

2.2. Consistency with thermodynamics

The model is also endowed with the following evolution equation for the entropy density ρS

$$\frac{\partial \rho S}{\partial t} + \frac{\partial (\rho S v_k + \rho H_k)}{\partial x_k} = \frac{\rho}{\theta_1(\tau_1)T} \psi_{ik} \psi_{ik} + \frac{\rho}{\theta_2(\tau_2)T} H_i H_i \geq 0 \quad (4)$$

which establishes the *second law of thermodynamics* for system (1).

System (1) belongs to the class of so-called Symmetric Hyperbolic and Thermodynamically Compatible (SHTC) systems [79] proposed by Godunov and Romenski in a series of papers [2, 14, 101, 5, 102]. In particular, this means that the over-determined¹ system (1) is compatible that is, the energy equation (1e), in fact, can be obtained as the linear combination of the remaining equations multiplied by certain factors (e.g. see [79])

$$(1e) = (\rho E)_\rho \cdot (1a) + (\rho E)_{\rho v_i} \cdot (1b) + (\rho E)_{A_{ik}} \cdot (1c) + (\rho E)_{J_k} \cdot (1d) + (\rho E)_{\rho S} \cdot (4) \quad (5)$$

In particular, the source terms in (1c) and (1d) are designed in such a way that, on one hand energy is conserved (there is no source term in (1e)) and, on the other hand the physical entropy is non-decreasing (see the *entropy inequality* in (4)).

2.3. Involution constraints

An important feature of the distortion and thermal impulse equations is that, e.g. see [79, 103],

$$\frac{\partial}{\partial t} (\nabla \times \mathbf{A} - \mathbf{B}) = 0, \quad \frac{\partial}{\partial t} (\nabla \times \mathbf{J} - \mathbf{\Omega}) = 0, \quad (6)$$

where $\mathbf{B} = [B_{ij}]$ and $\mathbf{\Omega} = [\Omega_i]$ are the solutions to

$$\frac{\partial B_{ij}}{\partial t} + \frac{\partial}{\partial x_k} (B_{ij} v_k - v_j B_{ik} + \varepsilon_{jkm} \theta_1^{-1} \psi_{im}) + v_j \frac{\partial B_{ik}}{\partial x_k} = 0, \quad (7a)$$

$$\frac{\partial \Omega_j}{\partial t} + \frac{\partial}{\partial x_k} (\Omega_j v_k - v_j \Omega_k + \varepsilon_{jkm} \theta_2^{-1} H_m) + v_j \frac{\partial \Omega_k}{\partial x_k} = 0, \quad (7b)$$

¹This system is over-determined because we have more equations than unknowns.

which can be derived from (1c) and (1d) by applying the curl operator “ $\nabla \times$ ” to them. It follows from these equations that, in the absence of source terms ($\theta_1 \sim \tau_1 \rightarrow \infty$ and $\theta_2 \sim \tau_2 \rightarrow \infty$), the solution to (1) satisfies the following two stationary linear constraints (involutions)

$$\frac{\partial A_{ik}}{\partial x_m} - \frac{\partial A_{im}}{\partial x_k} = 0, \quad \text{and} \quad \frac{\partial J_k}{\partial x_m} - \frac{\partial J_m}{\partial x_k} = 0, \quad (8)$$

if these constraints are satisfied by the initial data at $t = 0$. For finite values of τ_1 and τ_2 these curls are not zero in general, but satisfy the time evolution equations (7).

It is important to emphasize that even if the source terms in (1c) and (1d) are absent and thus, $\partial_m A_{ik} - \partial_k A_{im} = 0$ and $\partial_m J_k - \partial_k J_m = 0$, the PDEs (1c) and (1d) should not be replaced with equations in a conservative form such as

$$\frac{\partial A_{ik}}{\partial t} + \frac{\partial(A_{im} v_m)}{\partial x_k} = 0, \quad \frac{\partial J_k}{\partial t} + \frac{\partial(J_m v_m + T)}{\partial x_k} = 0, \quad (9)$$

because this would immediately destroy both the thermodynamic consistency, as well as the Galilean invariance. For example, equations (9) are *not* compatible with the energy conservation law (1e) in the sense of (5). Also, the conservative equations (9) have a characteristic structure that is not compatible with Galilean invariance of the PDE system, similar to the equations of magnetohydrodynamics (MHD) [104], which also belong to the SHTC class of equations [105].

Finally, we note that, generally speaking, an involution preserving scheme should in principle guarantee that the numerical solution to the full GPR model (i.e. with the dissipative source terms in (1c) and (1d)) should also satisfy equations (6) and (7). So far, we are not there yet, hence we only propose a numerical scheme which guarantees the fulfillment of the *stationary* involution constraints (8) in the absence of dissipative source terms.

2.4. Structural aspects of the governing PDEs

The SHTC theory starts from the question on the admissible structure of mechanically and thermodynamically consistent equations in continuum mechanics, e.g. see [79]. Therefore, there are several *structural aspects* of the governing equations that, ideally, have to be respected also at the discrete level. In what follows, we summarize three main structural features (SF) of the SHTC equations, the fulfillment of which at the discrete level may potentially be beneficial for the quality of the numerical solution.

SF1. Overdetermination: Equations (1), (4) form an overdetermined system of PDEs, that is there is one more equation than unknowns. But in fact, the total energy E is not an unknown but a potential $E = E(\rho, S, v_i, A_{ik}, J_k)$ while the entropy is a true unknown. However, usually it is not the entropy PDE (4) but the energy conservation law (1e) which is considered within the equations to be discretized in order to guaranty the energy conservation at the discrete level. Nevertheless, one may think of a new class of numerical schemes that explicitly takes into account the summation property (5) also at the discrete level. Such a scheme would discretize the entropy inequality (4) instead of the energy conservation law (1e), but due to the fulfillment of the summation property (5) at the discrete level it would automatically also guarantee the discrete energy conservation. We note that a general purpose scheme usually cannot automatically guarantee (5) at the discrete level.

SF2. Involution constraints: Homogeneous SHTC equations are usually endowed with stationary involution constraints of the type (8) which are usually just a part of a more general *integrability condition* like (7), e.g. see [79]. In this paper, we deal directly with stationary involution constraints of SHTC equations, while the general case of an integrability condition compatible scheme will be covered in future publications.

SF3. Equilibrium subsystem: SHTC equations possess two limiting PDE structures formally corresponding to $\tau_1 \rightarrow \infty, \tau_2 \rightarrow \infty$ (short wave-length limit) and $\tau_1 \rightarrow 0, \tau_2 \rightarrow 0$ (long wave-length limit). The former has the full SHTC structure and corresponds to the most non-equilibrium state of the system and is described by the homogeneous part of (1) with involution constraints (8), while the later has the reduced structure of five

Euler equations of ideal fluid² ($\tau_1 = \tau_2 = 0$, global thermodynamic equilibrium) or five Navier-Stokes-Fourier equations ($\tau_1 \ll 1, \tau_2 \ll 1$, local thermodynamic equilibrium). Thus, a proper structure preserving scheme should be able to reproduce both limits of SHTC equations as is the case with the proposed novel SPSIFV scheme.

SF4. Hamiltonian structure and symplectic integrators: as it was shown recently [79], the SHTC equations have an underlying Hamiltonian and thus geometrical structure. This means that the reversible part of the time evolution (i.e. all the differential terms in the left hand-side of (1), (4)) is actually generated by corresponding Poisson brackets. In fact, in Hamiltonian mechanics, there is a class of methods, called *symplectic integrators* [106], which aims in retaining the underlying geometrical structure of the governing equations. Adoption of a similar strategy for the numerical solution of the SHTC equations may, at least in principle, improve the overall quality and physical consistency of the numerical solution.

2.5. Equation of state

Throughout this paper we assume that the specific total energy can be written as a sum of three contributions as

$$E(\rho, v_i, p, A_{ik}, J_k) = E_1(\rho, p) + E_2(A_{ik}, J_k) + E_3(v_i), \quad (10)$$

with the specific internal energy given by the ideal gas equation of state

$$E_1(\rho, p) = \frac{p}{\rho(\gamma - 1)}, \quad \text{or} \quad E_1(\rho, s) = \frac{c_0^2}{\gamma(\gamma - 1)}, \quad c_0^2 = \gamma\rho^{\gamma-1}e^{s/c_v} \quad (11)$$

in the case of gases, and given by the so-called stiffened gas equation of state

$$E_1(\rho, p) = \frac{c_0^2}{\gamma(\gamma - 1)} \left(\frac{\rho}{\rho_0} \right)^{\gamma-1} e^{s/c_v} + \frac{\rho_0 c_0^2 - \gamma p_0}{\gamma\rho} \quad (12)$$

in the case of solids (c_v is the specific heat at constant volume, γ is the ration of specific heats, and p_0 and ρ_0 are the reference pressure and mass density, respectively). The specific energy stored in material deformations and in the thermal impulse is

$$E_2(A_{ik}, J_k) = \frac{1}{4}c_s^2 \mathring{G}_{ij} \mathring{G}_{ij} + \frac{1}{2}\alpha^2 J_k J_k, \quad (13)$$

where c_s is the characteristic velocity (assumed to be constant in this paper) of propagation of shear perturbations, while α (also constant) relates to the characteristic velocity of thermal perturbations c_h as $c_h^2 \sim \alpha^2 T / c_v$ (the SI units of α are $\frac{\text{m}^2}{\text{s}^2} \cdot \text{K}^{-1} \sim [c_v]$). Furthermore, $G_{ij} = A_{ki} A_{kj}$ is the Riemannian metric tensor induced by the mapping from Eulerian coordinates to the current stress-free reference configuration and \mathring{G}_{ij} is its trace-free part, defined as usual by

$$\mathring{G}_{ij} = G_{ij} - \frac{1}{3} G_{kk} \delta_{ij}. \quad (14)$$

For an alternative equation of state in nonlinear hyperelasticity, see [77]. The specific kinetic energy is contained in the third contribution to the total energy and reads

$$E_3(v_k) = \frac{1}{2} v_i v_i. \quad (15)$$

With the equation of state chosen above, we get the following expressions for the stress tensor, the heat flux and the functions $\psi_{ik} = E_{A_{ik}}$ and $H_k = E_{J_k}$ present in the relaxation source terms:

$$\sigma_{ik} = \rho c_s^2 G_{ij} \mathring{G}_{jk} + \rho \alpha^2 J_i J_k, \quad q_k = \rho T \alpha^2 J_k, \quad (16)$$

²Or eight equations of ideal magnetohydrodynamics [95] if coupled with the electromagnetic fields.

$$\psi_{ik} = c_s^2 A_{ij} \mathring{G}_{jk}, \quad H_k = \alpha^2 J_k. \quad (17)$$

The functions θ_1 and θ_2 are chosen in such a way that a *constant* shear viscosity μ and thermal conductivity κ are obtained in the stiff relaxation limit, see [1] for a formal asymptotic analysis:

$$\theta_1(\tau_1) = \frac{1}{3} \tau_1 c_s^2 |\mathbf{A}|^{\frac{5}{3}}, \quad \theta_2(\tau_2) = \tau_2 \frac{\alpha^2}{\rho T}, \quad (18)$$

Following the procedure detailed in [1], one can show via formal asymptotic expansion that in the stiff relaxation limit $\tau_1 \rightarrow 0$, $\tau_2 \rightarrow 0$ (i.e. small but fixed relaxation times $\tau_1 \ll 1$, $\tau_2 \ll 1$), the stress tensor and the heat flux reduce to

$$\boldsymbol{\sigma} = -\frac{1}{6} \rho_0 c_s^2 \tau_1 \left(\nabla \mathbf{v} + \nabla \mathbf{v}^T - \frac{2}{3} (\nabla \cdot \mathbf{v}) \mathbf{I} \right) - \frac{\alpha^2}{\rho T^2} \tau_2^2 \nabla T \otimes \nabla T, \quad (19)$$

and

$$\mathbf{q} = -\alpha^2 \tau_2 \nabla T, \quad (20)$$

so that

$$\mu = \frac{1}{6} \rho_0 \tau_1 c_s^2, \quad \kappa = \tau_2 \alpha^2. \quad (21)$$

One can see that the leading terms in the asymptotic expansions of the heat flux and stress tensor correspond to the Fourier law and Navier-Stokes viscous stress respectively. The second order with respect to τ_2 term in (19) is negligible for small $\tau_2 \ll 1$.

3. Numerical method

System (1) can be written more compactly in the following matrix-vector notation

$$\partial_t \mathbf{Q} + \nabla \cdot \mathbf{F}(\mathbf{Q}) + \mathbf{B}(\mathbf{Q}) \cdot \nabla \mathbf{Q} = \mathbf{S}(\mathbf{Q}), \quad (22)$$

with the state vector $\mathbf{Q} = (\rho, \rho v_i, A_{ik}, J_k, \rho E)^T$, the flux tensor $\mathbf{F}(\mathbf{Q})$, the non-conservative product $\mathbf{B}(\mathbf{Q}) \cdot \nabla \mathbf{Q}$ containing the curl terms and the vector of potentially stiff algebraic relaxation source terms $\mathbf{S}(\mathbf{Q})$. As proposed in [67, 69] we now *split* the flux tensor into a convective part and a pressure part. However, the equations for the new objects A_{ik} , J_k as well as their respective contributions to the momentum equation and to the total energy conservation law need a special *compatible* and structure-preserving discretization using a vertex-based grid staggering. Hence, eqn. (22) is rewritten as

$$\partial_t \mathbf{Q} + \nabla \cdot \left(\mathbf{F}_c(\mathbf{Q}) + \mathbf{F}_p(\mathbf{Q}) + \mathbf{F}_v(\mathbf{Q}) \right) + \nabla \mathbf{G}_v(\mathbf{Q}) + \mathbf{B}_v(\mathbf{Q}) \cdot \nabla \mathbf{Q} = \mathbf{S}(\mathbf{Q}), \quad (23)$$

where $\mathbf{F}_c(\mathbf{Q})$ refers to purely convective fluxes that will be discretized explicitly and $\mathbf{F}_p(\mathbf{Q})$ are the pressure fluxes that will be discretized implicitly using an edge-based staggered grid. The resulting splitting into pressure and convective fluxes is identical to the flux-vector splitting scheme of Toro and Vázquez-Cendón recently forwarded in [107]. The remaining terms $\mathbf{F}_v(\mathbf{Q})$, $\nabla \mathbf{G}_v(\mathbf{Q})$ and $\mathbf{B}_v(\mathbf{Q}) \cdot \nabla \mathbf{Q}$ will be carefully discretized in a structure-preserving manner using an explicit scheme on an appropriate vertex-based staggered grid. The relaxation source terms $\mathbf{S}(\mathbf{Q})$ can become stiff and thus require an implicit discretization on the vertex-based staggered mesh.

The split fluxes read

$$\mathbf{F}_c = \begin{pmatrix} \rho v_k \\ \rho v_i v_k \\ 0 \\ 0 \\ \rho v_k (E_2 + E_3) \end{pmatrix}, \quad \mathbf{F}_p = \begin{pmatrix} 0 \\ p \delta_{ik} \\ 0 \\ 0 \\ h \rho v_k \end{pmatrix}, \quad \mathbf{F}_v = \begin{pmatrix} 0 \\ -\sigma_{ik} \\ 0 \\ 0 \\ -v_i \sigma_{ik} + q_k \end{pmatrix}, \quad (24)$$

with the specific enthalpy $h = E_1 + p/\rho$. The terms involving the gradient operator $\nabla \mathbf{G}_v(\mathbf{Q})$ and the non-conservative product containing the curl terms read

$$\mathbf{G}_v(\mathbf{Q}) = \begin{pmatrix} 0 \\ 0 \\ A_{im}v_m \\ J_m v_m + T \\ 0 \end{pmatrix}, \quad \mathbf{B}_v(\mathbf{Q}) \cdot \nabla \mathbf{Q} = \begin{pmatrix} 0 \\ 0 \\ v_m \left(\frac{\partial A_{ik}}{\partial x_m} - \frac{\partial A_{im}}{\partial x_k} \right) \\ v_m \left(\frac{\partial J_k}{\partial x_m} - \frac{\partial J_m}{\partial x_k} \right) \\ 0 \end{pmatrix}. \quad (25)$$

The following subsystem

$$\partial_t \mathbf{Q} + \nabla \cdot (\mathbf{F}_c(\mathbf{Q}) + \mathbf{F}_v(\mathbf{Q})) + \nabla \mathbf{G}_v(\mathbf{Q}) + \mathbf{B}_v(\mathbf{Q}) \cdot \nabla \mathbf{Q} = \mathbf{S}(\mathbf{Q}), \quad (26)$$

will be discretized explicitly, apart from the potentially stiff algebraic source terms in \mathbf{S} , which are discretized implicitly with a simple backward Euler scheme. The discretization method presented in the next section will consist in a combination of a classical second order MUSCL-Hancock type [62] TVD finite volume scheme for the convective fluxes \mathbf{F}_c , a curl-free discretization for the terms \mathbf{G}_v and $\mathbf{B}_v \cdot \nabla \mathbf{Q}$ using compatible gradient and curl operators as well as a vertex-based discretization of the terms \mathbf{F}_v . The eigenvalues of subsystem (26) in x direction are

$$\lambda_{1,2}^{c,v} = \frac{1}{2}u \pm \frac{1}{2}\sqrt{\frac{4T}{c_v}\alpha^2 + u^2}, \quad \lambda_{3,4}^{c,v} = u \pm \frac{2}{3}\sqrt{3}c_s, \quad \lambda_{5,6,7,8}^{c,v} = u \pm c_s, \quad \lambda_{9,10,\dots,17}^{c,v} = u. \quad (27)$$

The remaining pressure subsystem, which will be discretized implicitly, reads as follows:

$$\partial_t \mathbf{Q} + \nabla \cdot \mathbf{F}_p(\mathbf{Q}) = 0. \quad (28)$$

As already mentioned before, the resulting pressure subsystem is formally identical to the Toro-Vázquez pressure system [107], hence its eigenvalues in x direction are

$$\lambda_{1,2}^p = \frac{1}{2}\left(u \pm \sqrt{u^2 + 4c_0^2}\right), \quad \lambda_{3,4,5,\dots,17}^p = 0, \quad (29)$$

with the adiabatic sound speed c_0 , e.g. for the ideal gas EOS we have, as usual, $c_0^2 = \gamma p/\rho$.

3.1. Staggered mesh and discrete divergence, curl and gradient operators

To simplify the description of the numerical scheme, we restrict the discussion to two-dimensional motion, i.e. we assume that $\frac{\partial}{\partial x_3}$ vanishes for all fields and thus, we assume a two-dimensional physical domain Ω spread in $x_1 = x$ and $x_2 = y$ and which is covered by a set of equidistant and non-overlapping Cartesian control volumes $\Omega^{p,q} = [x^{p-\frac{1}{2}}, x^{p+\frac{1}{2}}] \times [y^{q-\frac{1}{2}}, y^{q+\frac{1}{2}}]$ with uniform mesh spacings $\Delta x = x^{p+\frac{1}{2}} - x^{p-\frac{1}{2}}$ and $\Delta y = y^{q+\frac{1}{2}} - y^{q-\frac{1}{2}}$ in x and y direction, respectively, and with $x^{p\pm\frac{1}{2}} = x^p \pm \Delta x/2$ and $y^{q\pm\frac{1}{2}} = y^q \pm \Delta y/2$. Nevertheless, we keep all 3-*rd* components of vectors and tensors in the discussion. The 3D extension of the scheme is straightforward. We will furthermore use the notation $\mathbf{e}_x = (1, 0, 0)$, $\mathbf{e}_y = (0, 1, 0)$ and $\mathbf{e}_z = (0, 0, 1)$ for the unit vectors pointing into the directions of the Cartesian coordinate axes.

To avoid confusion between tensor indices and discretization indices, throughout this paper we will use the *subscripts* i, j, k, l, m for *tensor indices* and the *superscripts* n, p, q, r, s for the *discretization indices* in time and space, respectively. The discrete spatial coordinates will be denoted by x^p and y^q , while the set of discrete times will be denoted by t^n . For a sketch of the employed staggered grid arrangement of the main quantities, see Fig. 1.

The main ingredients of the new structure-preserving staggered semi-implicit scheme proposed in this paper are the definitions of appropriate discrete divergence, gradient and curl operators acting on quantities that are arranged in different and judiciously chosen locations on the staggered mesh. The discrete pressure field at time t^n is denoted by $p^{h,n}$ and its degrees of freedom are located in the center of each control volume as $p^{p,q,n} = p(x^p, y^q, t^n)$. Throughout this paper we denote with the superscript h the set of all degrees of freedom of the discrete solution and all degrees of

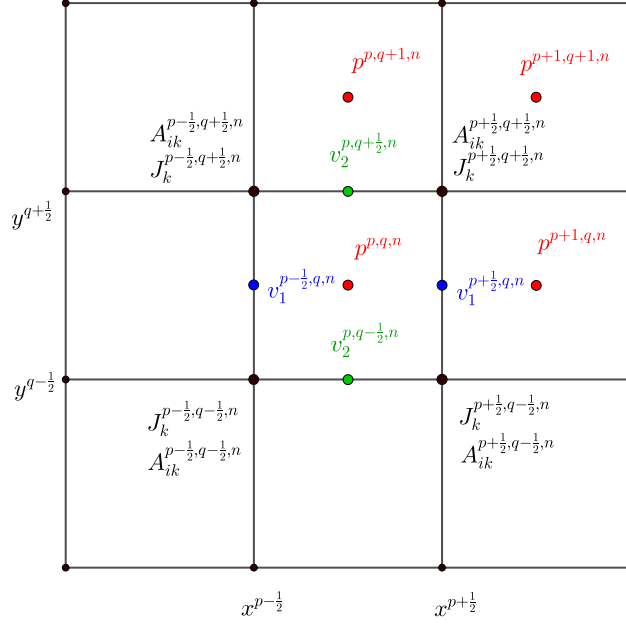


Figure 1: Staggered mesh configuration with the pressure field $p^{p,q,n}$ defined in the cell barycenters, the velocity field components $v_1^{p+1/2,q,n}$ and $v_2^{p,q+1/2,n}$ defined on the edge-based staggered dual grids, respectively, and the distortion field $A_{ik}^{p+1/2,q+1/2,n}$ as well as the specific thermal impulse $J_k^{p+1/2,q+1/2,n}$ defined on the vertices of the main grid.

freedom generated by a discrete operator, in order to ease notation. The discrete velocities $v_1^{h,n}$ and $v_2^{h,n}$ are arranged in an edge-based staggered fashion, i.e. $u^{p+1/2,q,n} := v_1^{p+1/2,q,n} = v_1(x^{p+1/2}, y^q, t^n)$ and $v^{p,q+1/2,n} := v_2^{p,q+1/2,n} = v_2(x^p, y^{q+1/2}, t^n)$. The discrete distortion field $\mathbf{A}^{h,n} = A_{ik}^{h,n}$ and the discrete thermal impulse $\mathbf{J}^{h,n} = J_k^{h,n}$ are defined on the *vertices* of each spatial control volume as $A_{ik}^{p+1/2,q+1/2,n} = A_{ik}(x^{p+1/2}, y^{q+1/2}, t^n)$ and $J_k^{p+1/2,q+1/2,n} = J_k(x^{p+1/2}, y^{q+1/2}, t^n)$, respectively. For clarity, see again Fig. 1.

The *discrete divergence operator*, $\nabla^h \cdot$, acting on a discrete vector field $\mathbf{v}^{h,n}$ is abbreviated by $\nabla^h \cdot \mathbf{v}^{h,n}$ and its degrees of freedom are given by

$$\nabla^{p,q} \cdot \mathbf{v}^{h,n} = \partial_k^{p,q} v_k^{h,n} = \frac{v_1^{p+1/2,q,n} - v_1^{p-1/2,q,n}}{\Delta x} + \frac{v_2^{p,q+1/2,n} - v_2^{p,q-1/2,n}}{\Delta y}, \quad (30)$$

i.e. it is based on the *edge-based* staggered values of the field $\mathbf{v}^{h,n}$. It defines a discrete divergence on the control volume $\Omega^{p,q}$ via the Gauss theorem,

$$\nabla^{p,q} \cdot \mathbf{v}^{h,n} = \frac{1}{\Delta x \Delta y} \int_{\Omega^{p,q}} \nabla \cdot \mathbf{v} dx = \frac{1}{\Delta x \Delta y} \int_{\partial \Omega^{p,q}} \mathbf{v} \cdot \mathbf{n} dS, \quad (31)$$

based on the mid-point rule for the computation of the integrals along each edge of $\Omega^{p,q}$. In (31) the outward pointing unit normal vector to the boundary $\partial \Omega^{p,q}$ of $\Omega^{p,q}$ is denoted by \mathbf{n} . In a similar manner, the *z* component of the *discrete curl*, $\nabla^h \times$, of a discrete vector field $\mathbf{J}^{h,n}$ is denoted by $(\nabla^h \times \mathbf{J}^{h,n}) \cdot \mathbf{e}_z$ and its degrees of freedom are naturally defined

as

$$\begin{aligned}
(\nabla^{p,q} \times \mathbf{J}^{h,n}) \cdot \mathbf{e}_z &= \epsilon_{3jk} \partial_j^{p,q} J_k^{h,n} \\
&= \frac{1}{2} \left(\frac{J_2^{p+\frac{1}{2},q+\frac{1}{2},n} - J_2^{p-\frac{1}{2},q+\frac{1}{2},n}}{\Delta x} + \frac{J_2^{p+\frac{1}{2},q-\frac{1}{2},n} - J_2^{p-\frac{1}{2},q-\frac{1}{2},n}}{\Delta x} \right) - \\
&\quad \frac{1}{2} \left(\frac{J_1^{p+\frac{1}{2},q+\frac{1}{2},n} - J_1^{p+\frac{1}{2},q-\frac{1}{2},n}}{\Delta y} + \frac{J_1^{p-\frac{1}{2},q+\frac{1}{2},n} - J_1^{p-\frac{1}{2},q-\frac{1}{2},n}}{\Delta y} \right), \tag{32}
\end{aligned}$$

making use of the *vertex-based* staggered values of the field $\mathbf{J}^{h,n}$, see the right panel in Fig. 2. In Eqn. (32) the symbol ϵ_{ijk} is the usual Levi-Civita tensor. Eqn. (32) defines a discrete curl on the control volume $\Omega^{p,q}$ via the Stokes theorem

$$(\nabla^h \times \mathbf{J}^{h,n}) \cdot \mathbf{e}_z = \frac{1}{\Delta x \Delta y} \int_{\Omega^{p,q}} (\nabla \times \mathbf{J}) \cdot \mathbf{e}_z \, d\mathbf{x} = \frac{1}{\Delta x \Delta y} \int_{\partial \Omega^{p,q}} \mathbf{J} \cdot \mathbf{t} \, dS, \tag{33}$$

based on the trapezoidal rule for the computation of the integrals along each edge of $\Omega^{p,q}$. Since the distortion field \mathbf{A} transforms as a vector and not as a rank 2 tensor (\mathbf{A} is a triad and thus a set of three vectors), the degrees of freedom of the z component of the discrete curl of $\mathbf{A}^{h,n}$ simply read

$$\begin{aligned}
(\nabla^{p,q} \times \mathbf{A}^{h,n}) \cdot \mathbf{e}_z &= \epsilon_{3jk} \partial_j^{p,q} A_{ik}^{h,n} \\
&= \frac{1}{2} \left(\frac{A_{i2}^{p+\frac{1}{2},q+\frac{1}{2},n} - A_{i2}^{p-\frac{1}{2},q+\frac{1}{2},n}}{\Delta x} + \frac{A_{i2}^{p+\frac{1}{2},q-\frac{1}{2},n} - A_{i2}^{p-\frac{1}{2},q-\frac{1}{2},n}}{\Delta x} \right) - \\
&\quad \frac{1}{2} \left(\frac{A_{i1}^{p+\frac{1}{2},q+\frac{1}{2},n} - A_{i1}^{p+\frac{1}{2},q-\frac{1}{2},n}}{\Delta y} + \frac{A_{i1}^{p-\frac{1}{2},q+\frac{1}{2},n} - A_{i1}^{p-\frac{1}{2},q-\frac{1}{2},n}}{\Delta y} \right). \tag{34}
\end{aligned}$$

Last but not least, we need to define a discrete gradient operator that is compatible with the discrete curl, so that the continuous identity

$$\nabla \times \nabla \phi = 0 \tag{35}$$

also holds on the discrete level. If we define a scalar field in the barycenters of the control volumes $\Omega^{p,q}$ as $\phi^{p,q,n} = \phi(x^p, y^q, t^n)$ then the corner gradient generates a natural discrete gradient operator ∇^h of the discrete scalar field $\phi^{h,n}$ that defines a discrete gradient in all vertices of the mesh. The corresponding degrees of freedom generated by $\nabla^h \phi^{h,n}$ read (see the left panel of Fig. 2)

$$\nabla^{p+\frac{1}{2},q+\frac{1}{2}} \phi^{h,n} = \partial_k^{p+\frac{1}{2},q+\frac{1}{2}} \phi^{h,n} = \begin{pmatrix} \frac{1}{2} \left(\frac{\phi^{p+1,q+1,n} - \phi^{p,q+1,n}}{\Delta x} + \frac{\phi^{p+1,q,n} - \phi^{p,q,n}}{\Delta x} \right) \\ \frac{1}{2} \left(\frac{\phi^{p+1,q+1,n} - \phi^{p+1,q,n}}{\Delta y} + \frac{\phi^{p,q+1,n} - \phi^{p,q,n}}{\Delta y} \right) \\ 0 \end{pmatrix}. \tag{36}$$

It is then straightforward to verify that an immediate consequence of (32) and (36) is

$$\nabla^h \times \nabla^h \phi^{h,n} = 0, \tag{37}$$

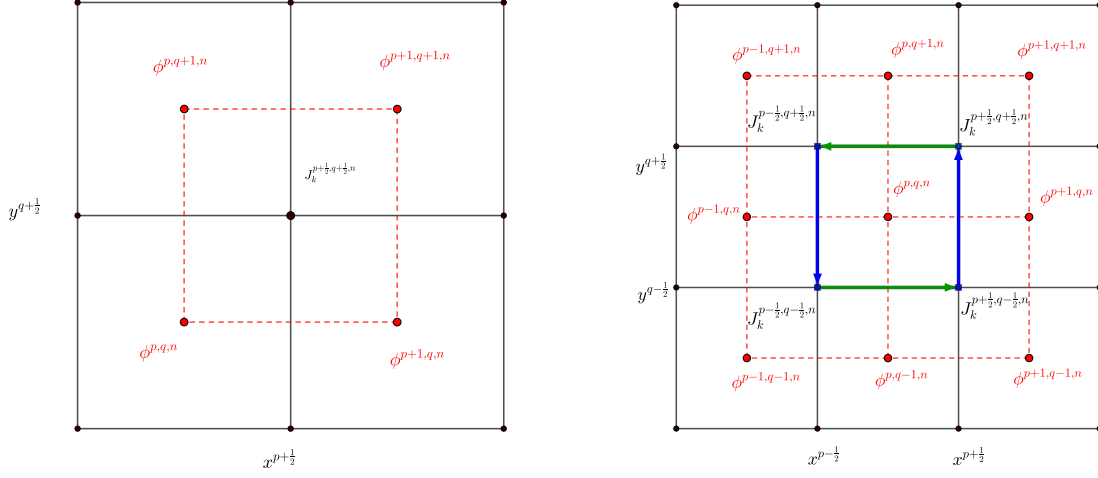


Figure 2: Left: stencil of the discrete gradient operator, which computes the corner gradient of a scalar field defined in the cell barycenter. Right: stencil of the discrete curl operator, which defines the curl inside the cell barycenter using the vector field components defined in the corners of the primary control volume. In the right panel we also show the total 9-point stencil that is needed for the discrete identity $\nabla^h \times \nabla^h \phi^{h, n} = 0$.

i.e. one obtains a discrete analogue of (35). This can be easily seen by computing

$$\begin{aligned}
& \left(\nabla^{p, q} \times \nabla^{p+\frac{1}{2}, q+\frac{1}{2}} \phi^{h, n} \right) \cdot \mathbf{e}_z = \\
& \frac{1}{4} \frac{(\phi^{p+1, q+1, n} - \phi^{p+1, q, n} + \phi^{p, q+1, n} - \phi^{p, q, n}) + (\phi^{p+1, q, n} - \phi^{p+1, q-1, n} + \phi^{p, q, n} - \phi^{p, q-1, n})}{\Delta x \Delta y} - \\
& \frac{1}{4} \frac{(\phi^{p, q+1, n} - \phi^{p, q, n} + \phi^{p-1, q+1, n} - \phi^{p-1, q, n}) + (\phi^{p, q, n} - \phi^{p, q-1, n} + \phi^{p-1, q, n} - \phi^{p-1, q-1, n})}{\Delta x \Delta y} - \\
& \frac{1}{4} \frac{(\phi^{p+1, q+1, n} - \phi^{p, q+1, n} + \phi^{p+1, q, n} - \phi^{p, q, n}) + (\phi^{p, q+1, n} - \phi^{p-1, q+1, n} + \phi^{p, q, n} - \phi^{p-1, q, n})}{\Delta y \Delta x} + \\
& \frac{1}{4} \frac{(\phi^{p+1, q, n} - \phi^{p, q, n} + \phi^{p+1, q-1, n} - \phi^{p, q-1, n}) + (\phi^{p, q, n} - \phi^{p-1, q, n} + \phi^{p, q-1, n} - \phi^{p-1, q-1, n})}{\Delta y \Delta x} = 0. \quad (38)
\end{aligned}$$

We furthermore define the following averaging operators from the three different staggered meshes to the cell barycenter (x^p, y^q) :

$$\begin{aligned}
J_k^{p, q, n} &= \frac{1}{4} \left(J_k^{p-\frac{1}{2}, q-\frac{1}{2}, n} + J_k^{p+\frac{1}{2}, q-\frac{1}{2}, n} + J_k^{p-\frac{1}{2}, q+\frac{1}{2}, n} + J_k^{p+\frac{1}{2}, q+\frac{1}{2}, n} \right), \\
v_1^{p, q, n} &= \frac{1}{2} \left(v_1^{p-\frac{1}{2}, q, n} + v_1^{p+\frac{1}{2}, q, n} \right), \\
v_2^{p, q, n} &= \frac{1}{2} \left(v_2^{p, q-\frac{1}{2}, n} + v_2^{p, q+\frac{1}{2}, n} \right). \quad (39)
\end{aligned}$$

3.2. Explicit, compatible discretization of the distortion field and of the thermal impulse

The key ingredient of the numerical method proposed in this paper is the proper discretization of the terms $\nabla \mathbf{G}_v(\mathbf{Q})$ and $\mathbf{B}_v(\mathbf{Q})\nabla \mathbf{Q}$ present in (23). We propose the following compatible discretization for the thermal impulse equation:

$$\begin{aligned} \mathbf{J}_k^{p+\frac{1}{2},q+\frac{1}{2},n+1} &= \mathbf{J}_k^{p+\frac{1}{2},q+\frac{1}{2},n} - \Delta t \partial_k^{p+\frac{1}{2},q+\frac{1}{2}} \left(J_m^{h,n} v_m^{h,n} + T^{h,n} \right) \\ &\quad - \Delta t \frac{1}{4} \sum_{r=0}^1 \sum_{s=0}^1 v_m^{p+r,q+s,n} \left(\partial_m^{p+r,q+s} J_k^{h,n} - \partial_k^{p+r,q+s} J_m^{h,n} \right) \\ &\quad - \Delta t \frac{\rho^{p+\frac{1}{2},q+\frac{1}{2},n} T^{p+\frac{1}{2},q+\frac{1}{2},n}}{\tau_2} J_k^{p+\frac{1}{2},q+\frac{1}{2},n+1}. \end{aligned} \quad (40)$$

It is easy to check that in the homogeneous case (when $\tau_2 \rightarrow \infty$ and therefore the algebraic source term vanishes) for an initially curl-free vector field $\mathbf{J}^{h,n}$ that satisfies $\nabla^h \times \mathbf{J}^{h,n} = 0$ also $\nabla^h \times \mathbf{J}^{h,n+1} = 0$ holds. To see this, one needs to apply the discrete curl operator $\nabla^h \times$ to Eqn. (40). One realizes that the second row of (40), which contains the discrete curl of $\mathbf{J}^{h,n}$ vanishes immediately, due to $\nabla^h \times \mathbf{J}^{h,n} = 0$. The third row vanishes because $\tau_2 \rightarrow \infty$. The curl of the first term on the right hand side in the first row of Eqn. (40) is zero because of $\nabla^h \times \mathbf{J}^{h,n} = 0$ and the curl of the second term is zero because of $\nabla^h \times \nabla^h \phi^{h,n} = 0$, with the auxiliary scalar field $\phi^{h,n} = J_m^{h,n} v_m^{h,n} + T^{h,n}$, whose degrees of freedom are computed as $\phi^{p,q,n} = J_m^{p,q,n} v_m^{p,q,n} + T^{p,q,n}$ after averaging of the velocity vector and the thermal impulse vector into the barycenters of the control volumes $\Omega^{p,q}$. The key ingredient of our compatible discretization for the \mathbf{J} equation is indeed the use of a discrete gradient operator that is compatible with the discrete curl operator, see Eq. (38).

The discrete form of the evolution equation of the distortion field is very similar to (40) and reads

$$\begin{aligned} A_{ik}^{p+\frac{1}{2},q+\frac{1}{2},n+1} &= A_{ik}^{p+\frac{1}{2},q+\frac{1}{2},n} - \Delta t \partial_k^{p+\frac{1}{2},q+\frac{1}{2}} \left(A_{im}^{h,n} v_m^{h,n} \right) \\ &\quad - \Delta t \frac{1}{4} \sum_{r=0}^1 \sum_{s=0}^1 v_m^{p+r,q+s,n} \left(\partial_m^{p+r,q+s} A_{ik}^{h,n} - \partial_k^{p+r,q+s} A_{im}^{h,n} \right) \\ &\quad - \Delta t \frac{\left| A_{ij}^{p+\frac{1}{2},q+\frac{1}{2},n+1} \right|^{\frac{5}{3}}}{\tau_1} A_{ij}^{p+\frac{1}{2},q+\frac{1}{2},n+1} G_{jk}^{p+\frac{1}{2},q+\frac{1}{2},n+1}. \end{aligned} \quad (41)$$

Following exactly the same reasoning as for the discrete thermal impulse equation, it is easy to check that in the homogeneous case (when $\tau_1 \rightarrow \infty$) for an initially curl-free distortion field $\mathbf{A}^{h,n}$ that satisfies $\nabla^h \times \mathbf{A}^{h,n} = 0$ also $\nabla^h \times \mathbf{A}^{h,n+1} = 0$ holds.

3.3. Compatible numerical viscosity

The previous discretizations were all *central* and thus without artificial numerical viscosity. In order to add a *compatible numerical viscosity* operator, we need to recall the definition of the vector Laplacian at the continuous level, which reads:

$$\nabla^2 \mathbf{J} = \nabla (\nabla \cdot \mathbf{J}) - \nabla \times \nabla \times \mathbf{J} \quad (42)$$

In order to define a discrete analogue of (42) we define another discrete divergence operator as follows:

$$\begin{aligned} \nabla^{p+\frac{1}{2},q+\frac{1}{2}} \cdot \mathbf{J}^{h,n} &= \partial_k^{p+\frac{1}{2},q+\frac{1}{2}} J_k^{h,n} = \\ &= \frac{1}{2} \left(\frac{J_1^{p+1,q+1,n} - J_1^{p,q+1,n}}{\Delta x} + \frac{J_1^{p+1,q,n} - J_1^{p,q,n}}{\Delta x} \right) + \\ &= \frac{1}{2} \left(\frac{J_2^{p+1,q+1,n} - J_2^{p+1,q,n}}{\Delta y} + \frac{J_2^{p,q+1,n} - J_2^{p,q,n}}{\Delta y} \right). \end{aligned} \quad (43)$$

The discrete vector Laplacian then simply reads

$$\nabla^{p+\frac{1}{2},q+\frac{1}{2}} \cdot \nabla^h \mathbf{J}^{h,n} = \nabla^{p+\frac{1}{2},q+\frac{1}{2}} \left(\nabla^h \cdot \mathbf{J}^{h,n} \right) - \nabla^{p+\frac{1}{2},q+\frac{1}{2}} \times \nabla^h \times \mathbf{J}^{h,n}, \quad (44)$$

i.e. it is composed of a grad-div contribution minus a curl-curl term. Taking (44) into account, a compatible discretization of \mathbf{J} with numerical viscosity then reads

$$\begin{aligned} J_k^{p+\frac{1}{2},q+\frac{1}{2},n+1} &= J_k^{p+\frac{1}{2},q+\frac{1}{2},n} - \Delta t \partial_k^{p+\frac{1}{2},q+\frac{1}{2}} \left(J_m^{h,n} v_m^{h,n} + T^{h,n} - h c_a \partial_k^h J_k^{h,n} \right) - \Delta t h c_a \epsilon_{kj3} \partial_j^{p+\frac{1}{2},q+\frac{1}{2}} \epsilon_{3lm} \partial_l^h J_m^{h,n} \\ &\quad - \Delta t \frac{1}{4} \sum_{r=0}^1 \sum_{s=0}^1 v_m^{p+r,q+s,n} \left(\partial_m^{p+r,q+s} J_k^{h,n} - \partial_k^{p+r,q+s} J_m^{h,n} \right) \\ &\quad - \Delta t \frac{\rho^{p+\frac{1}{2},q+\frac{1}{2},n} T^{p+\frac{1}{2},q+\frac{1}{2},n}}{\tau_2} J_k^{p+\frac{1}{2},q+\frac{1}{2},n+1}, \end{aligned} \quad (45)$$

where $h = \max(\Delta x, \Delta y)$ is a characteristic mesh spacing and c_a is a characteristic velocity related to the artificial viscosity that one would like to add to the scheme, e.g. $c_a = c_s$. For the sake of clarity, the additional numerical viscosity terms have been highlighted in red. It is obvious that also (45) satisfies the curl-free property $\nabla^h \times \mathbf{J}^{h,n+1} = 0$ under the assumptions that $\tau_2 \rightarrow \infty$ and $\nabla^h \times \mathbf{J}^{h,n} = 0$. In analogy, the final evolution equation for \mathbf{A} including the compatible numerical viscosity reads

$$\begin{aligned} A_{ik}^{p+\frac{1}{2},q+\frac{1}{2},n+1} &= A_{ik}^{p+\frac{1}{2},q+\frac{1}{2},n} - \Delta t \partial_k^{p+\frac{1}{2},q+\frac{1}{2}} \left(A_{im}^{h,n} v_m^{h,n} - h c_a \partial_k^h A_{ik}^{h,n} \right) - \Delta t h c_a \epsilon_{kj3} \partial_j^{p+\frac{1}{2},q+\frac{1}{2}} \epsilon_{3lm} \partial_l^h A_{im}^{h,n} \\ &\quad - \Delta t \frac{1}{4} \sum_{r=0}^1 \sum_{s=0}^1 v_m^{p+r,q+s,n} \left(\partial_m^{p+r,q+s} A_{ik}^{h,n} - \partial_k^{p+r,q+s} A_{im}^{h,n} \right) \\ &\quad - \Delta t \frac{\left| A_{ij}^{p+\frac{1}{2},q+\frac{1}{2},n+1} \right|^{\frac{5}{3}}}{\tau_1} A_{ij}^{p+\frac{1}{2},q+\frac{1}{2},n+1} G_{jk}^{p+\frac{1}{2},q+\frac{1}{2},n+1}. \end{aligned} \quad (46)$$

It is easy to check that one has $\nabla^h \times \mathbf{A}^{h,n+1} = 0$ as a consequence of (46) for $\tau_1 \rightarrow \infty$ and $\nabla^h \times \mathbf{A}^{h,n} = 0$. In order to reduce the numerical dissipation, it is possible to employ a piecewise linear reconstruction and insert the barycenter extrapolated values into the discrete divergence operator under the discrete gradient.

3.4. Explicit discretization of the nonlinear convective terms and of the corner fluxes

The semi-implicit scheme proposed in this paper applies an explicit discretization of the nonlinear convective terms contained in $\mathbf{F}_c = (\mathbf{f}_c(\mathbf{Q}), \mathbf{g}_c(\mathbf{Q}))$ and of the corner (vertex) fluxes $\mathbf{F}_v = (\mathbf{f}_v(\mathbf{Q}), \mathbf{g}_v(\mathbf{Q}))$, starting from the known solution $\mathbf{Q}^{p,q,n}$ at time t^n . The result is a new intermediate state vector $\mathbf{Q}^{p,q,*}$ that is computed via a conservative finite volume formulation

$$\mathbf{Q}^{p,q,*} = \mathbf{Q}^{p,q,n} - \frac{\Delta t}{\Delta x} \left(\mathbf{f}_{c,v}^{p+\frac{1}{2},q} - \mathbf{f}_{c,v}^{p-\frac{1}{2},q} \right) - \frac{\Delta t}{\Delta y} \left(\mathbf{g}_{c,v}^{p,q+\frac{1}{2}} - \mathbf{g}_{c,v}^{p,q-\frac{1}{2}} \right), \quad (47)$$

with the numerical fluxes defined as

$$\begin{aligned} \mathbf{f}_{c,v}^{p+\frac{1}{2},q} &= \frac{1}{2} \left(\mathbf{f}_c \left(\mathbf{Q}_-^{p+\frac{1}{2},q,n+\frac{1}{2}} \right) + \mathbf{f}_c \left(\mathbf{Q}_+^{p+\frac{1}{2},q,n+\frac{1}{2}} \right) \right) - \frac{1}{2} s_{\max}^x \left(\mathbf{Q}_+^{p+\frac{1}{2},q,n+\frac{1}{2}} - \mathbf{Q}_-^{p+\frac{1}{2},q,n+\frac{1}{2}} \right) \\ &\quad + \frac{1}{2} \left(\mathbf{f}_v \left(\mathbf{Q}^{p+\frac{1}{2},q+\frac{1}{2},n} \right) + \mathbf{f}_v \left(\mathbf{Q}^{p+\frac{1}{2},q-\frac{1}{2},n} \right) \right), \end{aligned} \quad (48)$$

and

$$\begin{aligned} \mathbf{g}_{c,v}^{p,q+\frac{1}{2}} &= \frac{1}{2} \left(\mathbf{g}_c \left(\mathbf{Q}_-^{p,q+\frac{1}{2},n+\frac{1}{2}} \right) + \mathbf{g}_c \left(\mathbf{Q}_+^{p,q+\frac{1}{2},n+\frac{1}{2}} \right) \right) - \frac{1}{2} s_{\max}^y \left(\mathbf{Q}_+^{p,q+\frac{1}{2},n+\frac{1}{2}} - \mathbf{Q}_-^{p,q+\frac{1}{2},n+\frac{1}{2}} \right) \\ &\quad + \frac{1}{2} \left(\mathbf{g}_v \left(\mathbf{Q}^{p+\frac{1}{2},q+\frac{1}{2},n} \right) + \mathbf{g}_v \left(\mathbf{Q}^{p-\frac{1}{2},q+\frac{1}{2},n} \right) \right). \end{aligned} \quad (49)$$

Note that the fluxes above contain the nonlinear convective terms as well as the vertex fluxes \mathbf{f}_v and \mathbf{g}_v , which contain the stress tensor $\boldsymbol{\sigma}$ and the heat flux \mathbf{q} . In Eqns. (48) and (49) the maximum signal speeds are computed as

$$\begin{aligned} s_{\max}^x &= \max\left(|\Lambda_x^{c,v}(\mathbf{Q}_-^{p+\frac{1}{2},q,n+\frac{1}{2}})|, |\Lambda_x^{c,v}(\mathbf{Q}_+^{p+\frac{1}{2},q,n+\frac{1}{2}})|\right), \\ s_{\max}^y &= \max\left(|\Lambda_y^{c,v}(\mathbf{Q}_-^{p,q+\frac{1}{2},n+\frac{1}{2}})|, |\Lambda_y^{c,v}(\mathbf{Q}_+^{p,q+\frac{1}{2},n+\frac{1}{2}})|\right), \end{aligned} \quad (50)$$

with $\Lambda_k^{c,v}$ the diagonal matrix of eigenvalues of the explicit subsystem (26) in direction x and y , respectively.

The boundary-extrapolated values are simply computed via a standard MUSCL-Hancock scheme (see [62]) as follows:

$$\begin{aligned} \mathbf{Q}_-^{p+\frac{1}{2},q,n+\frac{1}{2}} &= \mathbf{Q}^{p,q,n} + \frac{1}{2}\Delta x \partial_x^h \mathbf{Q}^{p,q,n} + \frac{1}{2}\Delta t \partial_t^h \mathbf{Q}^{p,q,n}, \\ \mathbf{Q}_+^{p+\frac{1}{2},q,n+\frac{1}{2}} &= \mathbf{Q}^{p+1,q,n} - \frac{1}{2}\Delta x \partial_x^h \mathbf{Q}^{p+1,q,n} + \frac{1}{2}\Delta t \partial_t^h \mathbf{Q}^{p+1,q,n}, \end{aligned}$$

and

$$\begin{aligned} \mathbf{Q}_-^{p,q+\frac{1}{2},n+\frac{1}{2}} &= \mathbf{Q}^{p,q,n} + \frac{1}{2}\Delta y \partial_y^h \mathbf{Q}^{p,q,n} + \frac{1}{2}\partial_t \mathbf{Q}^{p,q,n}, \\ \mathbf{Q}_+^{p,q+\frac{1}{2},n+\frac{1}{2}} &= \mathbf{Q}^{p,q+1,n} - \frac{1}{2}\Delta y \partial_y^h \mathbf{Q}^{p,q+1,n} + \frac{1}{2}\partial_t \mathbf{Q}^{p,q+1,n}, \end{aligned}$$

with the discrete gradients in space and time computed via

$$\begin{aligned} \partial_x^h \mathbf{Q}^{p,q,n} &= \text{minmod}\left(\frac{\mathbf{Q}^{p+1,q,n} - \mathbf{Q}^{p,q,n}}{\Delta x}, \frac{\mathbf{Q}^{p,q,n} - \mathbf{Q}^{p-1,q,n}}{\Delta x}\right), \\ \partial_y^h \mathbf{Q}^{p,q,n} &= \text{minmod}\left(\frac{\mathbf{Q}^{p+1,q,n} - \mathbf{Q}^{p,q,n}}{\Delta y}, \frac{\mathbf{Q}^{p,q,n} - \mathbf{Q}^{p-1,q,n}}{\Delta y}\right), \end{aligned}$$

and

$$\begin{aligned} \partial_t^h \mathbf{Q}^{p,q,n} &= -\frac{\mathbf{f}_c\left(\mathbf{Q}^{p,q,n} + \frac{1}{2}\Delta x \partial_x^h \mathbf{Q}^{p,q,n}\right) - \mathbf{f}_c\left(\mathbf{Q}^{p,q,n} - \frac{1}{2}\Delta x \partial_x^h \mathbf{Q}^{p,q,n}\right)}{\Delta x} \\ &\quad -\frac{\mathbf{g}_c\left(\mathbf{Q}^{p,q,n} + \frac{1}{2}\Delta y \partial_y^h \mathbf{Q}^{p,q,n}\right) - \mathbf{g}_c\left(\mathbf{Q}^{p,q,n} - \frac{1}{2}\Delta y \partial_y^h \mathbf{Q}^{p,q,n}\right)}{\Delta y}. \end{aligned}$$

3.5. Implicit solution of the pressure equation

Up to now, the contribution of the pressure to the momentum and to the total energy conservation laws has been excluded, i.e. the terms contained in the pressure fluxes \mathbf{F}_p . The discrete momentum equations including the pressure terms read

$$\begin{aligned} (\rho v)_1^{p+\frac{1}{2},q,n+1} &= (\rho v)_1^{p+\frac{1}{2},q,*} - \frac{\Delta t}{\Delta x} (p^{p+1,q,n+1} - p^{p,q,n+1}), \\ (\rho v)_2^{p,q+\frac{1}{2},n+1} &= (\rho v)_2^{p,q+\frac{1}{2},*} - \frac{\Delta t}{\Delta y} (p^{p,q+1,n+1} - p^{p,q,n+1}), \end{aligned} \quad (51)$$

where pressure is taken *implicitly*, while all nonlinear convective terms and the vertex fluxes have already been discretized *explicitly* via the operators $(\rho v)_1^{p+\frac{1}{2},q,*}$ and $(\rho v)_2^{p,q+\frac{1}{2},*}$ given in (47) and after averaging of the obtained quantities back to the edge-based staggered dual grid. A preliminary form of the discrete total energy equation reads

$$\begin{aligned} \rho E_1(p^{p,q,n+1}) + \rho E_2^{p,q,n+1} + \rho \tilde{E}_3^{p,q,n+1} &= \rho E^{p,q,*} \\ -\frac{\Delta t}{\Delta x} \left(\tilde{h}^{p+\frac{1}{2},q,n+1} (\rho v)_1^{p+\frac{1}{2},q,n+1} - \tilde{h}^{p-\frac{1}{2},q,n+1} (\rho v)_1^{p-\frac{1}{2},q,n+1} \right) \\ -\frac{\Delta t}{\Delta y} \left(\tilde{h}^{p,q+\frac{1}{2},n+1} (\rho v)_2^{p,q+\frac{1}{2},n+1} - \tilde{h}^{p,q-\frac{1}{2},n+1} (\rho v)_2^{p,q-\frac{1}{2},n+1} \right). \end{aligned} \quad (52)$$

Here, we have used the abbreviation $\rho E_1(p^{p,q,n+1}) = \rho^{p,q,n+1} E_1(p^{p,q,n+1}, \rho^{p,q,n+1})$. Inserting the discrete momentum equations (51) into the discrete energy equation (52) and making tilde symbols explicit via a simple Picard iteration (using the lower index r in the following), as suggested in [67, 69], leads to the following discrete wave equation for the unknown pressure:

$$\begin{aligned} & \rho^{p,q,n+1} E_1(p_{r+1}^{p,q,n+1}, \rho^{p,q,n+1}) \\ & - \frac{\Delta t^2}{\Delta x^2} \left(h_r^{p+\frac{1}{2},q,n+1} (p_{r+1}^{p+1,j,n+1} - p_{r+1}^{p,q,n+1}) - h_r^{p-\frac{1}{2},q,n+1} (p_{r+1}^{p,q,n+1} - p_{r+1}^{p-1,q,n+1}) \right) \\ & - \frac{\Delta t^2}{\Delta y^2} \left(h_r^{p,q+\frac{1}{2},n+1} (p_{r+1}^{p,q+1,n+1} - p_{r+1}^{p,q,n+1}) - h_r^{p,q-\frac{1}{2},n+1} (p_{r+1}^{p,q,n+1} - p_{r+1}^{p,q-1,n+1}) \right) = b_r^{p,q,n}, \end{aligned} \quad (53)$$

with the known right hand side

$$\begin{aligned} b_{i,j}^r &= \rho E^{p,q,*} - \rho E_2^{p,q,n+1} - \rho E_{3,r}^{p,q,n+1} \\ & - \frac{\Delta t}{\Delta x} \left(h_r^{p+\frac{1}{2},q,n+1} (\rho v)_1^{p+\frac{1}{2},q,*} - h_r^{p-\frac{1}{2},q,n+1} (\rho v)_1^{p-\frac{1}{2},q,*} \right) \\ & - \frac{\Delta t}{\Delta y} \left(h_r^{p,q+\frac{1}{2},n+1} (\rho v)_2^{p,q+\frac{1}{2},*} - h_r^{p,q-\frac{1}{2},n+1} (\rho v)_2^{p,q-\frac{1}{2},*} \right). \end{aligned} \quad (54)$$

The density at the new time $\rho^{p,q,n+1} = \rho^{p,q,*}$ is already known from (47), and also the energy contribution $\rho E_2^{p,q,n+1}$ of the distortion field $\mathbf{A}^{h,n+1}$ and of the thermal impulse $\mathbf{J}^{h,n+1}$ is already known, after averaging onto the main grid of the staggered field components that have been evolved in the vertices via the compatible discretization (41) and (40). The final system for the pressure (53) forms a *mildly nonlinear system* of the form

$$\rho \mathbf{E}_1(\mathbf{p}_{r+1}^{n+1}) + \mathbf{M}_r \cdot \mathbf{p}_{r+1}^{n+1} = \mathbf{b}_r^n \quad (55)$$

with a linear part contained in \mathbf{M} that is symmetric and at least positive semi-definite. Hence, with the usual assumptions on the nonlinearity detailed in [93], it can be again efficiently solved with the nested Newton method of Casulli and Zanolli [92, 93]. Note that in the incompressible limit $M \rightarrow 0$, following the asymptotic analysis performed in [108, 109, 110, 111, 112], the pressure tends to a constant and the contribution of the kinetic energy ρE_3 can be neglected w.r.t. ρE_1 . Therefore, in the incompressible limit the system (53) tends to the usual pressure Poisson equation of incompressible flow solvers. In each Picard iteration, after the solution of the pressure system (53), the enthalpies at the interfaces are recomputed and the momentum is updated by

$$(\rho v)_{1,r+1}^{p+\frac{1}{2},q,n+1} = (\rho v)_1^{p+\frac{1}{2},q,*} - \frac{\Delta t}{\Delta x} (p_{r+1}^{p+1,q,n+1} - p_{r+1}^{p,q,n+1}), \quad (56)$$

$$(\rho v)_{2,r+1}^{p,q+\frac{1}{2},n+1} = (\rho v)_2^{p,q+\frac{1}{2},*} - \frac{\Delta t}{\Delta y} (p_{r+1}^{p,q+1,n+1} - p_{r+1}^{p,q,n+1}), \quad (57)$$

from which the new kinetic energy density $(\rho E)_{3,r+1}^{p,q,n+1}$ can be computed after averaging the momentum onto the main grid. At the end of the Picard iterations, the total energy is updated as

$$\begin{aligned} (\rho E)^{p,q,n+1} &= (\rho E)^{p,q,*} - \frac{\Delta t}{\Delta x} \left(h^{p+\frac{1}{2},q,n+1} (\rho v)_1^{p+\frac{1}{2},q,n+1} - h^{p-\frac{1}{2},q,n+1} (\rho v)_1^{p-\frac{1}{2},q,n+1} \right) \\ & - \frac{\Delta t}{\Delta y} \left(h^{p,q+\frac{1}{2},n+1} (\rho v)_2^{p,q+\frac{1}{2},n+1} - h^{p,q-\frac{1}{2},n+1} (\rho v)_2^{p,q-\frac{1}{2},n+1} \right), \end{aligned} \quad (58)$$

while the final momentum is averaged back onto the main grid. This completes the description of our new curl-free semi-implicit finite volume scheme for the GPR model of continuum mechanics in the two-dimensional case. In the following Section 4 we provide a detailed analysis of the properties of the new algorithm.

3.6. No-slip wall boundary conditions for fluids

In the case of a viscous fluid, we want to impose $\mathbf{v} = \mathbf{v}_w$ for all $\mathbf{x} \in \partial\Omega_w$, where \mathbf{v}_w is a given velocity at the wall and $\partial\Omega_w$ is the part of the boundary occupied by the wall. In order to evolve the distortion field \mathbf{A} properly at wall boundary points, we rewrite its governing equation as

$$\partial_t A_{ik} + v_m \partial_m A_{ik} + A_{im} \partial_k v_m = -\frac{c_s^2 A_{ij} \mathring{G}_{jk}}{\theta_1(\tau_1)}, \quad (59)$$

which can be written in matrix-notation as

$$\partial_t \mathbf{A} + \mathbf{v} \cdot \nabla \mathbf{A} + \mathbf{A} \nabla \mathbf{v} = -\frac{c_s^2}{\theta_1(\tau_1)} \mathbf{A} \mathring{\mathbf{G}}. \quad (60)$$

In the following, we illustrate the procedure for a no-slip wall on the upper boundary, see also Fig. 3. Analogous formulas can be derived also for the lower boundary as well as for a boundary on the left and right of the domain, respectively. At the wall, the velocity field is known as $\mathbf{v}_w^{p+\frac{1}{2},q+\frac{1}{2},n} = \mathbf{v}_w(x^{p+\frac{1}{2}}, y^{q+\frac{1}{2}}, t^n)$ and the velocity gradient at the boundary $\nabla \mathbf{v}^{p+\frac{1}{2},q+\frac{1}{2},n} = (\partial_x \mathbf{v}^{p+\frac{1}{2},q+\frac{1}{2},n}, \partial_y \mathbf{v}^{p+\frac{1}{2},q+\frac{1}{2},n})^T$ is computed as in a classical Navier-Stokes code, making use of one-sided differences and the known velocity field at the wall:

$$\partial_x \mathbf{v}^{p+\frac{1}{2},q+\frac{1}{2},n} = \frac{\mathbf{v}_w^{p+1,q+\frac{1}{2},n} - \mathbf{v}_w^{p,q+\frac{1}{2},n}}{\Delta x}, \quad \partial_y \mathbf{v}^{p+\frac{1}{2},q+\frac{1}{2},n} = \frac{\mathbf{v}_w^{p+\frac{1}{2},q+1,n} - \mathbf{v}_w^{p+\frac{1}{2},q,n}}{\Delta y/2}, \quad (61)$$

with $\mathbf{v}_w^{p+\frac{1}{2},q+\frac{1}{2},n} = \frac{1}{2} (\mathbf{v}_w^{p,q+\frac{1}{2},n} + \mathbf{v}_w^{p+1,q+\frac{1}{2},n})$ computed from the known wall velocities on the boundary and $\mathbf{v}^{p+\frac{1}{2},q,n} = \frac{1}{2} (\mathbf{v}^{p,q,n} + \mathbf{v}^{p+1,q,n})$, where $\mathbf{v}^{p,q,n}$ and $\mathbf{v}^{p+1,q,n}$ are the known velocity vectors inside the computational domain and defined at the barycenter of a primary control volume.

For completeness, we also give the formula for a wall boundary at the right x boundary of the domain:

$$\partial_x \mathbf{v}^{p+\frac{1}{2},q+\frac{1}{2},n} = \frac{\mathbf{v}_w^{p+\frac{1}{2},q+\frac{1}{2},n} - \mathbf{v}_w^{p,q+\frac{1}{2},n}}{\Delta x/2}, \quad \partial_y \mathbf{v}^{p+\frac{1}{2},q+\frac{1}{2},n} = \frac{\mathbf{v}_w^{p+\frac{1}{2},q+1,n} - \mathbf{v}_w^{p+\frac{1}{2},q,n}}{\Delta y}, \quad (62)$$

with the analogous definitions $\mathbf{v}_w^{p+\frac{1}{2},q+\frac{1}{2},n} = \frac{1}{2} (\mathbf{v}_w^{p+\frac{1}{2},q,n} + \mathbf{v}_w^{p+\frac{1}{2},q+1,n})$ and $\mathbf{v}^{p,q+\frac{1}{2},n} = \frac{1}{2} (\mathbf{v}^{p,q,n} + \mathbf{v}^{p,q+1,n})$.

Once the velocity gradients have been computed the distortion field at the boundary points is evolved via the following implicit formula:

$$\mathbf{A}^{p+\frac{1}{2},q+\frac{1}{2},n+1} + \Delta t \mathbf{A}^{p+\frac{1}{2},q+\frac{1}{2},n+1} \nabla \mathbf{v}^{p+\frac{1}{2},q+\frac{1}{2},n} + \frac{\Delta t c_s^2}{\theta_1(\tau_1)} \mathbf{A}^{p+\frac{1}{2},q+\frac{1}{2},n+1} \mathring{\mathbf{G}}^{p+\frac{1}{2},q+\frac{1}{2},n+1} = \mathbf{A}^{p+\frac{1}{2},q+\frac{1}{2},n} - \Delta t \mathbf{v}_w^{p+\frac{1}{2},q+\frac{1}{2},n} \cdot \nabla_h^{p+\frac{1}{2},q+\frac{1}{2},n} \mathbf{A}_h, \quad (63)$$

where $\nabla_h^{p+\frac{1}{2},q+\frac{1}{2},n} \mathbf{A}_h$ is a suitable upwind discretization of the convective term, based on the known velocity field $\mathbf{v}_w^{p+\frac{1}{2},q+\frac{1}{2},n}$ at the wall. For a wall at rest, this term obviously vanishes. In the interior of the domain, the formula (46) remains valid.

4. Analysis of the scheme

While the discrete curl-free property of the scheme in the case $\tau_1 \rightarrow \infty$ and $\tau_2 \rightarrow \infty$ is very easy to see directly from the structure of the discrete equations (40) and (41) together with the discrete property (38), the behaviour of the scheme in the stiff relaxation limit $\tau_1 \rightarrow 0$ and $\tau_2 \rightarrow 0$ deserves more attention and is analyzed in the following. For the sake of simplicity, we start with the analysis of the fully discrete equation for the specific thermal impulse \mathbf{J} , showing that in this case the proposed method is *asymptotic preserving* (AP). Then, we also study the stiff relaxation limit of the semi-discrete equation for \mathbf{A} , which is much more complicated.

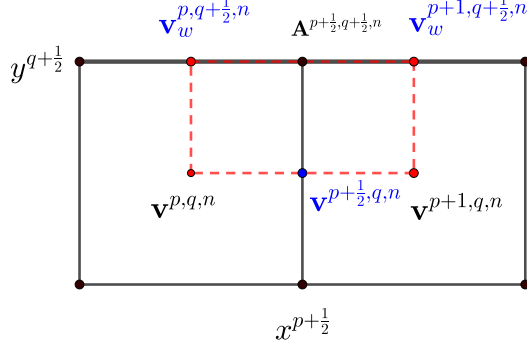


Figure 3: Calculation of the velocity gradient for a wall boundary condition at the upper y boundary of a rectangular domain Ω .

4.1. Asymptotic relaxation limit for the heat flux for $\tau_2 \rightarrow 0$

Without numerical viscosity, the fully-discrete equation for \mathbf{J} reads (see (40))

$$\begin{aligned}
J_k^{p+\frac{1}{2},q+\frac{1}{2},n+1} - J_k^{p+\frac{1}{2},q+\frac{1}{2},n} + \Delta t \partial_k^{p+\frac{1}{2},q+\frac{1}{2}} \left(J_m^{h,n} v_m^{h,n} \right) + \Delta t \partial_k^{p+\frac{1}{2},q+\frac{1}{2}} T^{h,n} \\
+ \Delta t \frac{1}{4} \sum_{r=0}^1 \sum_{s=0}^1 v_m^{p+r,q+s,n} \left(\partial_m^{p+r,q+s} J_k^{h,n} - \partial_k^{p+r,q+s} J_m^{h,n} \right) \\
= -\Delta t \frac{\rho^{p+\frac{1}{2},q+\frac{1}{2},n} T^{p+\frac{1}{2},q+\frac{1}{2},n}}{\tau_2} J_k^{p+\frac{1}{2},q+\frac{1}{2},n+1}.
\end{aligned} \tag{64}$$

Formal asymptotic expansion of the discrete solution J_m^h in powers of τ_2 yields

$$J_k^{p+\frac{1}{2},q+\frac{1}{2},n+1} = J_{k,(0)}^{p+\frac{1}{2},q+\frac{1}{2},n+1} + \tau_2 J_{k,(1)}^{p+\frac{1}{2},q+\frac{1}{2},n+1} + \dots \tag{65}$$

Inserting (65) into (64), collecting terms of equal powers in τ_2 and retaining only the leading order terms yields

$$\begin{aligned}
J_{k,(0)}^{p+\frac{1}{2},q+\frac{1}{2},n+1} - J_{k,(0)}^{p+\frac{1}{2},q+\frac{1}{2},n} + \Delta t \partial_k^{p+\frac{1}{2},q+\frac{1}{2}} \left(J_{m,(0)}^{h,n} v_m^{h,n} \right) + \Delta t \partial_k^{p+\frac{1}{2},q+\frac{1}{2}} T^{h,n} \\
+ \Delta t \frac{1}{4} \sum_{r=0}^1 \sum_{s=0}^1 v_m^{p+r,q+s,n} \left(\partial_m^{p+r,q+s} J_{k,(0)}^{h,n} - \partial_k^{p+r,q+s} J_{m,(0)}^{h,n} \right) \\
= -\Delta t \frac{1}{\tau_2} \rho^{p+\frac{1}{2},q+\frac{1}{2},n} T^{p+\frac{1}{2},q+\frac{1}{2},n} J_{k,(0)}^{p+\frac{1}{2},q+\frac{1}{2},n+1} - \Delta t \rho^{p+\frac{1}{2},q+\frac{1}{2},n} T^{p+\frac{1}{2},q+\frac{1}{2},n} J_{k,(1)}^{p+\frac{1}{2},q+\frac{1}{2},n+1}.
\end{aligned} \tag{66}$$

From the leading order term τ_2^{-1} one can conclude that the leading order contribution to \mathbf{J} must vanish, i.e.

$$J_{k,(0)}^{p+\frac{1}{2},q+\frac{1}{2},n+1} = 0. \tag{67}$$

Inserting (67) into (66) and assuming that due to (67) also $J_{k,(0)}^{p+\frac{1}{2},q+\frac{1}{2},n} = 0$ (well-prepared initial data) leads to the following result for the terms of order τ_2^0

$$J_{k,(1)}^{p+\frac{1}{2},q+\frac{1}{2},n+1} = -\frac{1}{\rho^{p+\frac{1}{2},q+\frac{1}{2},n} T^{p+\frac{1}{2},q+\frac{1}{2},n}} \partial_k^{p+\frac{1}{2},q+\frac{1}{2}} T^{h,n}. \tag{68}$$

Inserting (67) and (68) into (65) yields the following final result for the discrete specific thermal impulse when $\tau_2 \rightarrow 0$:

$$J_k^{p+\frac{1}{2},q+\frac{1}{2},n+1} = -\frac{\tau_2}{\rho^{p+\frac{1}{2},q+\frac{1}{2},n} T^{p+\frac{1}{2},q+\frac{1}{2},n}} \partial_k^{p+\frac{1}{2},q+\frac{1}{2}} T^{h,n}. \tag{69}$$

As a result, in the stiff relaxation limit $\tau_2 \rightarrow 0$ the discrete heat flux vector $\mathbf{q} = \rho T \mathbf{J}$ becomes

$$q_k^{p+\frac{1}{2}, q+\frac{1}{2}, n} = -\tau_2 \alpha^2 \partial_k^{p+\frac{1}{2}, q+\frac{1}{2}} T^{h, n}, \quad (70)$$

which is the discrete analogue of the Fourier law (20). As a consequence, for the heat flux the proposed staggered semi-implicit finite volume scheme is *asymptotic preserving*, see [113, 114, 115, 116, 117, 118, 119, 120], i.e. in the stiff relaxation limit the classical parabolic Navier-Stokes heat flux is retrieved also at the fully discrete level. The same AP result is also obtained in the presence of numerical viscosity, since all extra terms with respect to (40) scale with \mathbf{J} and thus are of order τ_2 , see (45).

Note that in (70), the gradient of the temperature is computed in the vertices of the primary control volumes (corner gradient), which is a rather common choice for the discretization of the compressible Navier-Stokes equations.

4.2. Asymptotic relaxation limit of the stress tensor for $\tau_1 \rightarrow 0$

The asymptotic analysis for the stress tensor is much more complex than the previous one for the heat flux. In the following, we consider only the following *semi-discrete* scheme for \mathbf{A} , without numerical viscosity and restricting the discussion to the two-dimensional case, i.e. $\partial_3 = 0$ and $v_3 = 0$:

$$\begin{aligned} \partial_r A_{ik}^{p+\frac{1}{2}, q+\frac{1}{2}, n+1} + \partial_k^{p+\frac{1}{2}, q+\frac{1}{2}} (A_{im}^h v_m^h) + \frac{1}{4} \sum_{r=0}^1 \sum_{s=0}^1 v_m^{p+r, q+s} (\partial_m^{p+r, q+s} A_{ik}^h - \partial_k^{p+r, q+s} A_{im}^h) \\ = -\frac{|A_{ij}^{p+\frac{1}{2}, q+\frac{1}{2}}|^{\frac{5}{3}}}{\tau_1} A_{ij}^{p+\frac{1}{2}, q+\frac{1}{2}} G_{jk}^{p+\frac{1}{2}, q+\frac{1}{2}}. \end{aligned} \quad (71)$$

For the sake of clarity, in the following, we give the explicit expansion of several terms appearing in (71):

$$\partial_1^{p+\frac{1}{2}, q+\frac{1}{2}} (A_{im}^h v_m^h) = \frac{1}{2} \frac{A_{im}^{p+1, q+1} v_m^{p+1, q+1} + A_{im}^{p+1, q} v_m^{p+1, q} - A_{im}^{p, q+1} v_m^{p, q+1} - A_{im}^{p, q} v_m^{p, q}}{\Delta x}, \quad (72)$$

$$\partial_2^{p+\frac{1}{2}, q+\frac{1}{2}} (A_{im}^h v_m^h) = \frac{1}{2} \frac{A_{im}^{p+1, q+1} v_m^{p+1, q+1} + A_{im}^{p, q+1} v_m^{p, q+1} - A_{im}^{p+1, q} v_m^{p+1, q} - A_{im}^{p, q} v_m^{p, q}}{\Delta y}, \quad (73)$$

with the quantity $A_{im}^{p, q}$ at the barycenter computed via averaging from the four surrounding vertices as

$$A_{im}^{p, q} = \frac{1}{4} \left(A_{im}^{p+\frac{1}{2}, q+\frac{1}{2}} + A_{im}^{p+\frac{1}{2}, q-\frac{1}{2}} + A_{im}^{p-\frac{1}{2}, q+\frac{1}{2}} + A_{im}^{p-\frac{1}{2}, q-\frac{1}{2}} \right). \quad (74)$$

We furthermore expand the second term in the double sum in x and y direction as follows:

$$-\frac{1}{4} \sum_{r=0}^1 \sum_{s=0}^1 v_m^{p+r, q+s} \partial_1^{p+r, q+s} A_{im}^h = -\frac{1}{8} \sum_{r=0}^1 \sum_{s=0}^1 v_m^{p+r, q+s} \frac{A_{im}^{p+\frac{1}{2}+r, q+\frac{1}{2}+s} + A_{im}^{p+\frac{1}{2}+r, q-\frac{1}{2}+s} - A_{im}^{p-\frac{1}{2}+r, q+\frac{1}{2}+s} - A_{im}^{p-\frac{1}{2}+r, q-\frac{1}{2}+s}}{\Delta x}, \quad (75)$$

$$-\frac{1}{4} \sum_{r=0}^1 \sum_{s=0}^1 v_m^{p+r, q+s} \partial_2^{p+r, q+s} A_{im}^h = -\frac{1}{8} \sum_{r=0}^1 \sum_{s=0}^1 v_m^{p+r, q+s} \frac{A_{im}^{p+\frac{1}{2}+r, q+\frac{1}{2}+s} + A_{im}^{p-\frac{1}{2}+r, q+\frac{1}{2}+s} - A_{im}^{p+\frac{1}{2}+r, q-\frac{1}{2}+s} - A_{im}^{p-\frac{1}{2}+r, q-\frac{1}{2}+s}}{\Delta y}. \quad (76)$$

After some calculations one obtains the following intermediate results, where all Taylor series expansions are carried out about the point (x^p, y^q) :

$$\begin{aligned}
\partial_1^{p+\frac{1}{2}, q+\frac{1}{2}} (A_{im}^h v_m^h) - \frac{1}{4} \sum_{r=0}^1 \sum_{s=0}^1 v_m^{p+r, q+s} \partial_1^{p+r, q+s} A_{im}^h &= A_{im}^{p+\frac{1}{2}, q+\frac{1}{2}} \cdot \frac{1}{2} \frac{v_m^{p+1, q+1} + v_m^{p+1, q} - v_m^{p, q+1} - v_m^{p, q}}{\Delta x} \\
&+ \frac{1}{4} \left(A_{im}^{p+\frac{1}{2}, q+\frac{3}{2}} - A_{im}^{p+\frac{1}{2}, q+\frac{1}{2}} \right) \frac{v_m^{p+1, q+1} - v_m^{p, q+1}}{\Delta x} \\
&- \frac{1}{4} \left(A_{im}^{p+\frac{1}{2}, q+\frac{1}{2}} - A_{im}^{p+\frac{1}{2}, q-\frac{1}{2}} \right) \frac{v_m^{p+1, q} - v_m^{p, q}}{\Delta x} \\
&= A_{im}^{p+\frac{1}{2}, q+\frac{1}{2}} \partial_1^{p+\frac{1}{2}, q+\frac{1}{2}} v_m^h + \frac{1}{4} \Delta y^2 \left(\partial_y A_{im} \partial_{xy} v_m + \partial_{yy} A_{im} \partial_x v_m \right), \\
&= A_{im}^{p+\frac{1}{2}, q+\frac{1}{2}} \partial_1^{p+\frac{1}{2}, q+\frac{1}{2}} v_m^h + \mathcal{O}(\Delta y^2), \tag{77}
\end{aligned}$$

$$\begin{aligned}
\partial_2^{p+\frac{1}{2}, q+\frac{1}{2}} (A_{im}^h v_m^h) - \frac{1}{4} \sum_{r=0}^1 \sum_{s=0}^1 v_m^{p+r, q+s} \partial_2^{p+r, q+s} A_{im}^h &= A_{im}^{p+\frac{1}{2}, q+\frac{1}{2}} \cdot \frac{1}{2} \frac{v_m^{p+1, q+1} + v_m^{p, q+1} - v_m^{p+1, q} - v_m^{p, q}}{\Delta y} \\
&+ \frac{1}{4} \left(A_{im}^{p+\frac{3}{2}, q+\frac{1}{2}} - A_{im}^{p+\frac{1}{2}, q+\frac{1}{2}} \right) \frac{v_m^{p+1, q+1} - v_m^{p+1, q}}{\Delta y} \\
&- \frac{1}{4} \left(A_{im}^{p+\frac{1}{2}, q+\frac{1}{2}} - A_{im}^{p-\frac{1}{2}, q+\frac{1}{2}} \right) \frac{v_m^{p, q+1} - v_m^{p, q}}{\Delta y} \\
&= A_{im}^{p+\frac{1}{2}, q+\frac{1}{2}} \partial_2^{p+\frac{1}{2}, q+\frac{1}{2}} v_m^h + \frac{1}{4} \Delta x^2 \left(\partial_x A_{im} \partial_{xy} v_m + \partial_{xx} A_{im} \partial_y v_m \right), \\
&= A_{im}^{p+\frac{1}{2}, q+\frac{1}{2}} \partial_2^{p+\frac{1}{2}, q+\frac{1}{2}} v_m^h + \mathcal{O}(\Delta x^2), \tag{78}
\end{aligned}$$

The convective term appears from the first term under the double sum expands as

$$\begin{aligned}
\frac{1}{4} \sum_{r=0}^1 \sum_{s=0}^1 (v_m^{p+r, q+s} \partial_m^{p+r, q+s} A_{ik}^h) &= \frac{1}{8} \sum_{r=0}^1 \sum_{s=0}^1 v_1^{p+r, q+s} \frac{A_{im}^{p+\frac{1}{2}+r, q+\frac{1}{2}+s} + A_{im}^{p+\frac{1}{2}+r, q-\frac{1}{2}+s} - A_{im}^{p-\frac{1}{2}+r, q+\frac{1}{2}+s} - A_{im}^{p-\frac{1}{2}+r, q-\frac{1}{2}+s}}{\Delta x} + \\
&\frac{1}{8} \sum_{r=0}^1 \sum_{s=0}^1 v_2^{p+r, q+s} \frac{A_{im}^{p+\frac{1}{2}+r, q+\frac{1}{2}+s} + A_{im}^{p-\frac{1}{2}+r, q+\frac{1}{2}+s} - A_{im}^{p+\frac{1}{2}+r, q-\frac{1}{2}+s} - A_{im}^{p-\frac{1}{2}+r, q-\frac{1}{2}+s}}{\Delta y} \\
&= v_m^{p+\frac{1}{2}, q+\frac{1}{2}} \partial_m^{p+\frac{1}{2}, q+\frac{1}{2}} A_{ik}^h + \frac{1}{8} \Delta x^2 \left(2\partial_{xx} A_{ik} \partial_x v_1 + 2\partial_{xy} A_{ik} \partial_x v_2 + \partial_x A_{ik} \partial_{xx} v_1 + \partial_y A_{ik} \partial_{xx} v_2 \right) \\
&\quad + \frac{1}{8} \Delta y^2 \left(2\partial_{xy} A_{ik} \partial_y v_1 + 2\partial_{yy} A_{ik} \partial_y v_2 + \partial_x A_{ik} \partial_{yy} v_1 + \partial_y A_{ik} \partial_{yy} v_2 \right) \\
&= v_m^{p+\frac{1}{2}, q+\frac{1}{2}} \partial_m^{p+\frac{1}{2}, q+\frac{1}{2}} A_{ik}^h + \mathcal{O}(\Delta x^2, \Delta y^2). \tag{79}
\end{aligned}$$

Combining the previous results and rearranging terms, one can finally rewrite (71) as follows:

$$\partial_t A_{ik}^{p+\frac{1}{2}, q+\frac{1}{2}} + v_m^{p+\frac{1}{2}, q+\frac{1}{2}} \partial_m^{p+\frac{1}{2}, q+\frac{1}{2}} A_{ik}^h + A_{im}^{p+\frac{1}{2}, q+\frac{1}{2}} \partial_k^{p+\frac{1}{2}, q+\frac{1}{2}} v_m^h + \mathcal{O}(\Delta x^2, \Delta y^2) = - \frac{\left| A_{ij}^{p+\frac{1}{2}, q+\frac{1}{2}} \right|^{\frac{5}{3}}}{\tau_1} A_{ij}^{p+\frac{1}{2}, q+\frac{1}{2}} G_{jk}^{p+\frac{1}{2}, q+\frac{1}{2}}. \tag{80}$$

Using the definition of the material derivative $Dq/Dt = \partial q/\partial t + \mathbf{v} \cdot \nabla q$ we can rewrite the previous equation in the following semi-discrete form based on the material derivative:

$$\frac{D}{Dt} A_{ik}^{p+\frac{1}{2}, q+\frac{1}{2}} + A_{im}^{p+\frac{1}{2}, q+\frac{1}{2}} \partial_k^{p+\frac{1}{2}, q+\frac{1}{2}} v_m^h + \mathcal{O}(\Delta x^2, \Delta y^2) = - \frac{\left| A_{ij}^{p+\frac{1}{2}, q+\frac{1}{2}} \right|^{\frac{5}{3}}}{\tau_1} A_{ij}^{p+\frac{1}{2}, q+\frac{1}{2}} G_{jk}^{p+\frac{1}{2}, q+\frac{1}{2}}. \tag{81}$$

Multiplication of the above equation with \mathbf{A}^T from the left and adding the transposed equation multiplied by \mathbf{A} from the right yields the semi-discrete Lagrangian evolution equation for the metric tensor \mathbf{G} :

$$\frac{D}{Dt} G_{ik}^{p+\frac{1}{2},q+\frac{1}{2}} + G_{im}^{p+\frac{1}{2},q+\frac{1}{2}} \partial_k^{p+\frac{1}{2},q+\frac{1}{2}} v_m^h + G_{mk}^{p+\frac{1}{2},q+\frac{1}{2}} \partial_i^{p+\frac{1}{2},q+\frac{1}{2}} v_m^h + \mathcal{O}(\Delta x^2, \Delta y^2) = -2 \frac{|A_{ij}^{p+\frac{1}{2},q+\frac{1}{2}}|^{\frac{5}{3}}}{\tau_1} G_{ij}^{p+\frac{1}{2},q+\frac{1}{2}} G_{jk}^{p+\frac{1}{2},q+\frac{1}{2}}. \quad (82)$$

Formal asymptotic expansion of the metric tensor in terms of τ_1 provides the ansatz

$$G_{ij}^{p+\frac{1}{2},q+\frac{1}{2}} = G_{ij,(0)}^{p+\frac{1}{2},q+\frac{1}{2}} + \tau_1 G_{ij,(1)}^{p+\frac{1}{2},q+\frac{1}{2}} + \dots \quad (83)$$

which can now be inserted into (82). The leading order term τ_1^{-1} leads to the first result

$$G_{ij,(0)}^{p+\frac{1}{2},q+\frac{1}{2}} = 0, \quad (84)$$

i.e. at leading order the discrete metric tensor $\mathbf{G}^{p+\frac{1}{2},q+\frac{1}{2}}$ becomes trace-free. Applying the “dev” operator, with $\text{dev}(\mathbf{G}) = \mathbf{G} - \frac{1}{3} \text{tr}(\mathbf{G}) \mathbf{I}$, to (82) and repeating the calculations already presented in [1] for the continuous case, leads to the following asymptotic result for the discrete stress tensor in the absence of heat conduction ($\alpha = 0$), from which we can conclude that for $\tau_1 \rightarrow 0$ the compressible Navier-Stokes stress tensor is retrieved up to second order of accuracy in space:

$$\sigma_{ik}^{p+\frac{1}{2},q+\frac{1}{2}} = \rho c_s^2 G_{ij}^{p+\frac{1}{2},q+\frac{1}{2}} G_{jk}^{p+\frac{1}{2},q+\frac{1}{2}} = \frac{1}{6} \rho_0 c_s^2 \tau_1 \left(\partial_i^{p+\frac{1}{2},q+\frac{1}{2}} v_k^h + \partial_k^{p+\frac{1}{2},q+\frac{1}{2}} v_i^h - \frac{2}{3} \delta_{ik} \partial_m^{p+\frac{1}{2},q+\frac{1}{2}} v_m^h \right) + \mathcal{O}(\Delta x^2, \Delta y^2). \quad (85)$$

Note that in (85) the gradient of the velocity field is computed in the vertices of the primary control volumes (corner gradient), which is a very common choice for the discretization of the compressible Navier-Stokes equations.

Unfortunately, the second order error terms $\mathcal{O}(\Delta x^2, \Delta y^2)$ remain in the asymptotic relaxation limit of the discrete stress tensor (85) and do *not* vanish for $\tau_1 \rightarrow 0$. Hence, the scheme is *not* rigorously asymptotic preserving (AP) for the viscous stress when $\tau_1 \rightarrow 0$, in contrast to the discrete heat flux discussed in the previous section, which reduces to a perfect discrete analogue of the Fourier law for $\tau_2 \rightarrow 0$. Instead, for σ the method proposed in this paper is only *quasi* asymptotic preserving, up to the second order error terms in (85). However, when inserting the discrete stress tensor (85) into the discrete momentum equation (51) with (47) the errors $\mathcal{O}(\Delta x^2, \Delta y^2)$ will add to the numerical errors already made in the discretization of the nonlinear convective terms, see (47), which, in general, are of second order in space and time when a second order MUSCL-Hancock-type upwind scheme is used. Since the numerical errors of the discretization of the nonlinear convective terms also do *not* scale with τ_1 , overall the above result can still be considered as satisfactory for our practical purposes, despite its obvious limitations and shortcomings.

The difference in the asymptotic behaviour of the stress tensor compared to the one of the heat flux is mainly due to the highly nonlinear nature of the equation for \mathbf{A} due to the nonlinearity of its relaxation source term, compared to the simple quasi linear relaxation source term in the equation for \mathbf{J} . Further research on this topic needs to be carried out in the future, investigating the possibility to find a compatible curl-free discretization of the PDE for \mathbf{A} that is also rigorously asymptotic preserving with the Navier-Stokes limit of σ .

4.3. Behavior of the scheme at low Mach numbers

Assuming no viscosity and no heat conduction (e.g. by simply setting $c_s = \alpha = 0$ and thus $E_2 = 0$), in the low Mach number limit the pressure tends to a constant in space and the velocity field will asymptotically satisfy the classical divergence-free condition of incompressible inviscid flows, see [108, 109, 112]. As a result of the divergence-free condition of the velocity field, the mass conservation equation can be rewritten as

$$\frac{\partial \rho}{\partial t} + \mathbf{v} \cdot \nabla \rho = 0, \quad (86)$$

which is a simple scalar transport equation for the density. If the initial condition satisfies $\rho(\mathbf{x}, 0) = \rho_0 = \text{const}$ then $\rho(\mathbf{x}, t) = \rho_0 = \text{const}$ for all times. Assuming therefore ρ and p constant in space and time at the leading order and the contribution of the kinetic energy negligible, we have $h = \text{const}$ and $\rho E_1 = \text{const}$ and therefore with $E_2 = 0$ the pressure equation (53) tends to the classical pressure Poisson equations for incompressible flows:

$$-\frac{\Delta t^2}{\Delta x^2} \left((p^{p+1,q,n+1} - p^{p,q,n+1}) - (p^{p,q,n+1} - p^{p-1,q,n+1}) \right) - \frac{\Delta t^2}{\Delta y^2} \left((p^{p,q+1,n+1} - p^{p,q,n+1}) - (p^{p,q,n+1} - p^{p,q-1,n+1}) \right) = -\frac{\Delta t}{\Delta x} \left((\rho v)_1^{p+\frac{1}{2},q,*} - (\rho v)_1^{p-\frac{1}{2},q,*} \right) - \frac{\Delta t}{\Delta y} \left((\rho v)_2^{p,q+\frac{1}{2},*} - (\rho v)_2^{p,q-\frac{1}{2},*} \right). \quad (87)$$

This behavior was expected, since the method presented in this paper is a staggered pressure-based scheme.

5. Numerical results

In all the following test problems, whenever a viscosity coefficient μ is specified together with a shear sound speed c_s , the corresponding relaxation time τ_1 in the GPR model is computed from (21) as $\tau_1 = 6\mu/(\rho_0 c_s^2)$, according to the results of the asymptotic analysis carried out in [1] for $E_2(A_{ik}, J_k)$ given by (13). If another form of the energy E_2 is used the expression for the viscosity may change, while staying of the form $\mu \sim \tau c_s^2$.

5.1. Solid rotor problem and numerical verification of the discrete curl-free property

In this first test problem we carry out a numerical verification of the discrete curl-free property of the new structure-preserving semi-implicit finite volume scheme proposed in this paper. The main objective here is to check whether the practical implementation of the new method is correct and if the scheme properly achieves the curl-free property that was proven in the previous section 4. For this purpose we solve the homogeneous system (1) by setting $\tau_1 = \tau_2 = 10^{20}$ which corresponds to a hyperelastic solid. The computational domain is chosen as $\Omega = [-1, +1]^2$ with periodic boundary conditions everywhere. The initial data is given by $\rho = 1$, $p = 1$, $\mathbf{A} = \mathbf{I}$ and $\mathbf{J} = \mathbf{0}$. The initial condition for the velocity field is chosen as $u = -y/R$, $v = +x/R$ and $w = 0$ within the circular region $r \leq R$, where $r = \|\mathbf{x}\|_2$ and $R = 0.2$, while $\mathbf{v} = \mathbf{0}$ for $r > R$. The remaining parameters of the model are chosen as $\gamma = 1.4$, $c_s = 1.0$ and $\alpha = 0.5$. The setup of the test problem is similar, but not identical, to the one proposed in [121]. We solve the problem with the new structure-preserving semi-implicit finite volume scheme until $t = 0.3$ on a grid composed of 500×500 elements. For comparison, the same problem is also solved on the same grid with a standard second-order accurate explicit MUSCL-Hancock finite volume scheme, see [62] for details. The results are compared with each other in Fig. 4, where the contour colors of the velocity component u and the distortion field component A_{11} are shown. In the color contours of Fig. 4, there are essentially no differences between the two solutions. However, if we compare the time evolution of the L_1 errors of the curl of \mathbf{A} and \mathbf{J} of the two schemes, see Fig. 5, we observe that the SPSIFV scheme is able to maintain the curl errors close to machine zero, while the L_1 norms of the curl errors produced by the standard MUSCL-Hancock method are more than ten orders of magnitude larger. These results for a non-trivial test case exhibiting all types of waves (shear and pressure waves) confirm the correct implementation of the new SPSIFV method, for which the curl-free property has been proven in the previous section 4.

5.2. Simple shear motion in solids and fluids

In this section we verify the new structure-preserving scheme for simple shear motion of fluids and solids. For this test we use the computational domain $\Omega = [-0.5; +0.5]^2$, with periodic boundary conditions in y direction and fixing the initial condition at the boundaries in x direction. The initial condition of the problem is given by $\rho = 1$, $u = 0$, $p = 1/\gamma$, $\mathbf{A} = \mathbf{I}$, $\mathbf{J} = \mathbf{0}$, while the velocity component v is $v = -v_0$ for $x < 0$ and $v = +v_0$ for $x \geq 0$. The parameters of this test are $v_0 = 0.1$, $\gamma = 1.4$, $c_v = 1$, $\rho_0 = 1$, $c_s = 1$ and $\alpha = 0$. The simulations are performed with the SPSIFV scheme on a grid composed of 1000×20 control volumes up to a final time of $t = 0.4$. In fluid mechanics, such an isolated, unsteady and infinitely long shear layer is also known as the first problem of Stokes, which admits an

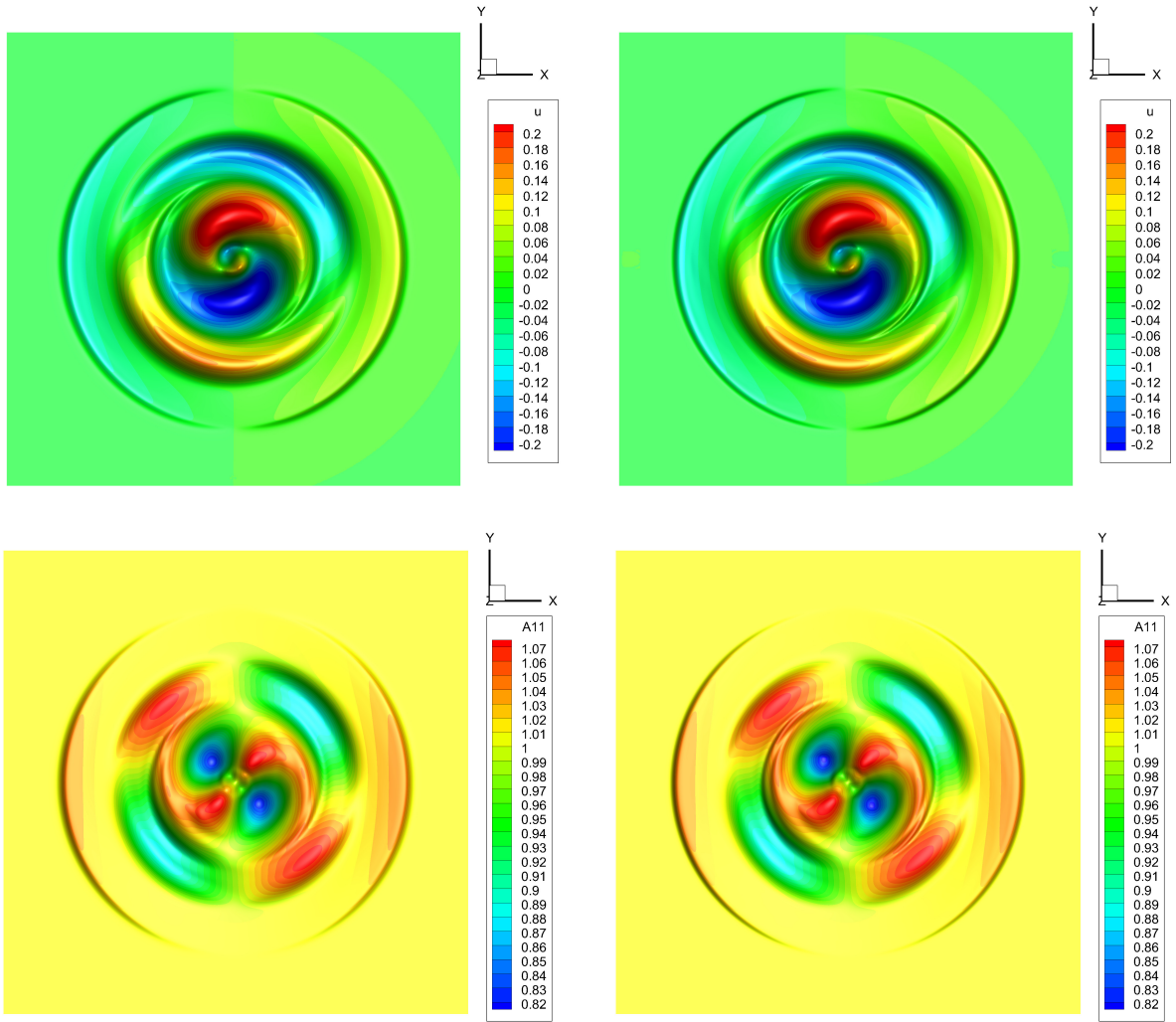


Figure 4: 2D solid rotor problem for the homogeneous GPR model with $\tau_1 = \tau_2 = 10^{20}$ at time $t = 0.30$. Color contours for the velocity component u (top) and the distortion field component A_{11} (bottom) computed with a classical explicit MUSCL TVD scheme (right) and with the new structure-preserving semi-implicit FV scheme (left).

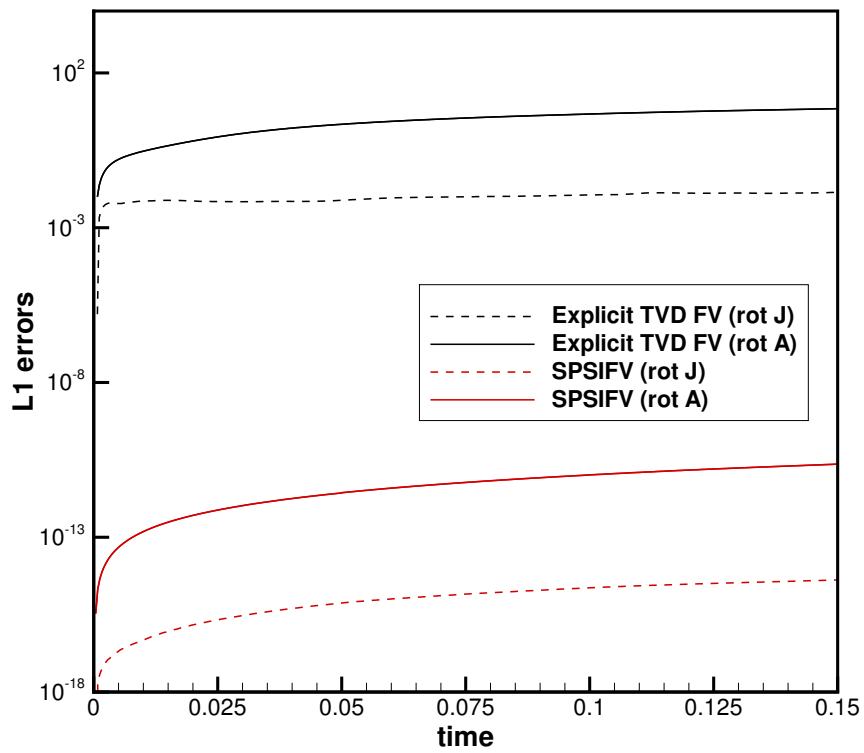


Figure 5: Time series of the L_1 error norms of the curl of \mathbf{A} and \mathbf{J} for the 2D solid rotor problem until time $t = 0.3$ using a standard second order MUSCL-Hancock-type TVD finite volume scheme (black) and the new structure-preserving semi-implicit finite volume scheme (red). The new structure-preserving method is able to preserve all curl-free conditions of the GPR model essentially up to machine precision.

exact solution of the incompressible Navier-Stokes equations, see e.g. [122]. The exact solution of the incompressible Navier-Stokes equations for the velocity component v is given by

$$v(x, t) = v_0 \operatorname{erf}\left(\frac{1}{2} \frac{x}{\sqrt{vt}}\right), \quad (88)$$

with $\nu = \mu/\rho_0$ and which can be used as a reference solution for the GPR model in the stiff relaxation limit. For solid materials, this initial data leads to two shear waves traveling outward with speed c_s .

The comparison between the Navier-Stokes reference solution (88) and the numerical results obtained with the new SPSIFV scheme for the GPR model are presented in Fig. 6, where one can observe an excellent agreement between the two for various viscosities μ . In the same Figure 6 we also present numerical results and a reference solution for the case of an ideal elastic solid, i.e. for the case when $\tau_1 \rightarrow \infty$ and thus the strain relaxation source term vanishes. Also in this case we obtain a very good agreement between the numerical solution and the reference solution, which was computed with an explicit second order MUSCL TVD finite volume scheme on a very fine mesh of 5000 cells.

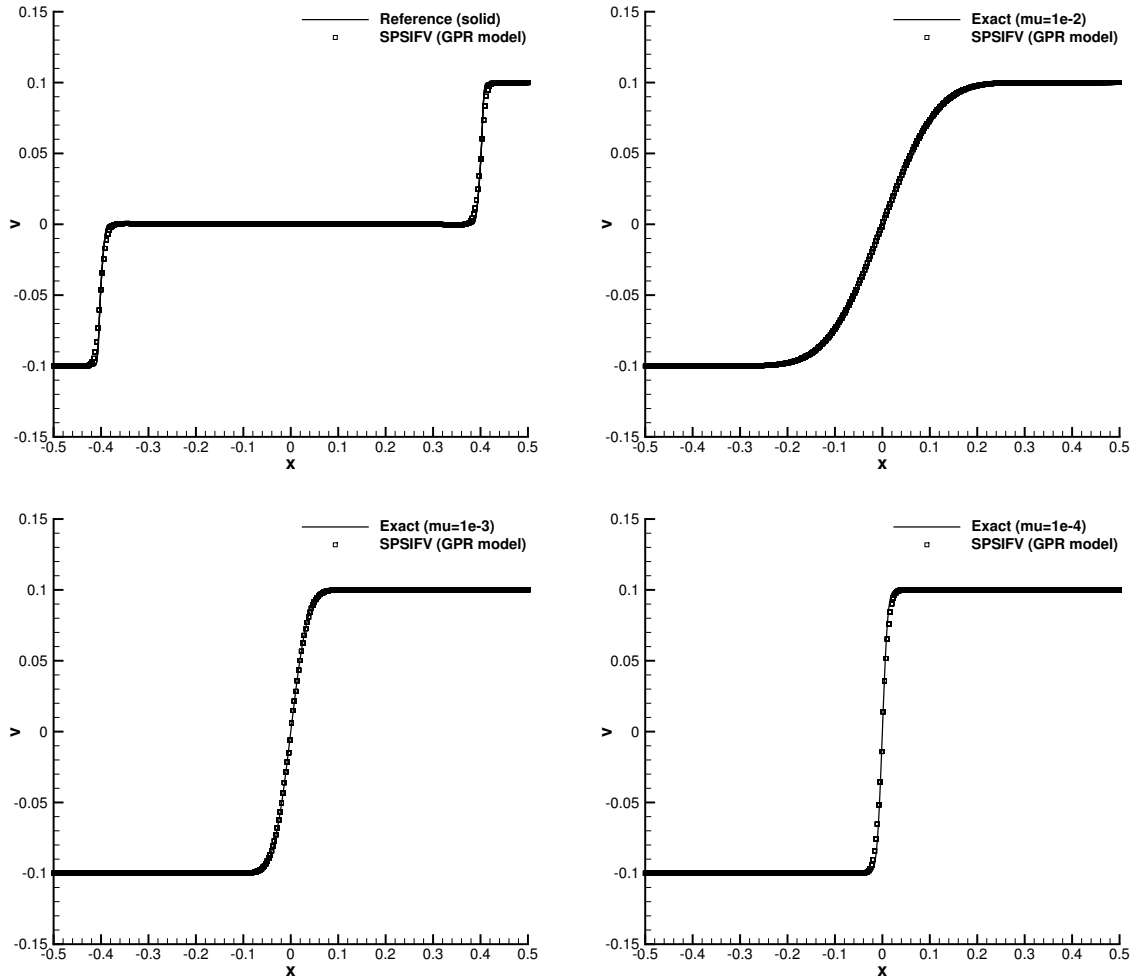


Figure 6: Numerical solution obtained with the structure-preserving semi-implicit finite volume (SPSIFV) scheme for the GPR model for a simple shear flow in fluids and in an elastic solid at time $t = 0.4$. Results for the solid (top left) and for fluids with different viscosities: $\mu = 10^{-2}$ (top right), $\mu = 10^{-3}$ (bottom left) and $\mu = 10^{-4}$ (bottom right). For fluids, this test corresponds to the first problem of Stokes, which has an exact solution.

5.3. Riemann problems for nearly inviscid fluids and ideal elastic solids

In this section we solve a set of one-dimensional Riemann problems in the fluid and solid limit of the GPR model, i.e. for $\tau \rightarrow 0$ and $\tau \rightarrow \infty$, respectively. In the case of the inviscid fluid limit ($\tau \rightarrow 0$) the source terms in the PDE for \mathbf{A} and \mathbf{J} become stiff and therefore an implicit treatment is mandatory. In this limit of the GPR model, the reference solution is given by the exact solution of the Riemann problem of the Euler equations of compressible gas dynamics, see [62] for details. In the case of an ideal elastic solid ($\tau \rightarrow \infty$), the governing PDE system becomes homogeneous and we simply compute a reference solution by solving the governing PDE system with a classical explicit second order accurate shock capturing TVD finite volume scheme on a very fine mesh composed of 10000 elements. While the Riemann problem of the 1D Euler equations contains only five waves (two acoustic waves, one $x - y$ shear wave, one $x - z$ shear wave and one entropy wave), the homogeneous GPR model contains much more waves (two fast thermo-acoustic waves, two slow thermo-acoustic waves, two $x - y$ shear waves, two $x - z$ shear waves, one entropy wave, and a set of waves associated with advection at speed u , see Appendix Appendix A). For the discussion of Riemann solvers and the exact and approximate solution of the Riemann problem for nonlinear hyperelasticity, the reader is referred to [73, 123].

The setup of all Riemann problems is described in the following. The computational domain is given by $\Omega = [-0.5, +0.5]^2$ and is discretized with a computational grid of 1000×20 elements. We use periodic boundary conditions in y direction and impose the initial condition as Dirichlet boundary condition in the x direction. The parameters of the GPR model are set to $\rho_0 = 1$, $\gamma = 1.4$ and $c_s = \alpha = 1$ for all Riemann problems apart from RP2, where we use $c_s = \alpha = 2$. The initial data for density, pressure and velocity are given in Table 1, where also the relaxation times τ_1 and τ_2 are provided. The remaining state variables are set to $w = 0$, $\mathbf{A} = \sqrt{\rho} \mathbf{I}$ and $\mathbf{J} = 0$.

RP1 and RP2 are the classical Sod and Lax shock tube problem, respectively, which are well-known in the context of compressible gas dynamics. The respective computational results obtained with the new SPSIFV scheme are presented in Figures 7 and 8, where we can in general observe a good agreement between the numerical solution of the GPR model and the exact solution of the Riemann problem of the compressible Euler equations.

Instead, RP3 and RP4 are the same Riemann problem with shear, once computed in the fluid limit (RP3) and once solved in the solid limit (RP4). The computational results are shown in Figures 9 and 10. In the fluid limit (Fig. 9 we can indeed observe four waves, namely one contact discontinuity, one shear wave and two acoustic waves (a rarefaction moving to the left and a shock wave moving to the right). The agreement with the exact solution of the Euler equations is excellent. In case of the homogeneous system (RP4), one can observe 7 waves in Figure 10, namely two fast thermo-acoustic waves (a right-moving shock and a left-moving rarefaction), two slow thermo-acoustic waves (again a right-moving shock and a left-moving rarefaction), two $x - y$ shear waves and one contact discontinuity. The agreement with the reference solution is very good also in this case.

Last but not least, we also report the time needed for one single element update as measured on one single CPU core of an Intel i9-7900X CPU with 3.3 GHz nominal clock speed and 32 GB of RAM. Since the first three Riemann problems contain stiff source terms, the necessary CPU time is higher than the one for RP4, where no source terms are present: The CPU time needed for one element update was $6.6 \mu\text{s}$ for RP1, $6.9 \mu\text{s}$ for RP2, $6.4 \mu\text{s}$ for RP3 and $3.1 \mu\text{s}$ for RP4.

5.4. Viscous shock wave

Here we simulate the problem of a stationary viscous shock wave at a shock Mach number of $M_s = 2$. For the special case of Prandtl number $\text{Pr} = 0.75$, there exists an exact solution of the compressible Navier-Stokes equation that was first found by Becker [124] in 1923, see [124, 125, 1] for details.

The computational domain $\Omega = [0, 1]^2$ is discretized with 400×10 cells and the shock wave is centered at $x = 0.5$. We suppose that the pre-shocked fluid is moving from right to left into the shock wave.

The values of the fluid in front of the shock wave are chosen as $\rho_0 = 1$, $u_0 = -2$, $v_0 = w_0 = 0$ and $p_0 = 1/\gamma$, hence $c_0 = 1$. The Reynolds number based on the flow speed u_0 and a unitary reference length ($L = 1$) is given by $Re_s = \frac{\rho_0 c_0 M_s L}{\mu}$. The parameters of the GPR model are chosen as $\gamma = 1.4$, $c_v = 2.5$, $\alpha = c_s = 50$, $\mu = 2 \cdot 10^{-2}$ and

Table 1: Initial states left (L) and right (R) for density ρ , velocity $\mathbf{v} = (u, v, 0)$ and pressure p for a set of Riemann problems solved on the domain $\Omega = [-\frac{1}{2}, +\frac{1}{2}]$ using the new structure-preserving semi-implicit FV scheme. The remaining variables of the GPR model are initialized as $\mathbf{A} = \sqrt[3]{\rho} \mathbf{I}$ and $\mathbf{J} = 0$. The Riemann problems include the fluid limit (RP1-RP3) as well as the solid limit (RP4). The relaxation times τ_1 and τ_2 are also specified. In all cases we set $\gamma = 1.4$.

RP	ρ_L	u_L	v_L	p_L	ρ_R	u_R	v_R	p_R	τ_1	τ_2
RP1	1.0	0.0	0.0	1.0	0.125	0.0	0.0	0.1	10^{-6}	10^{-6}
RP2	0.445	0.698	0.0	3.528	0.5	0.0	0.0	0.571	10^{-6}	10^{-6}
RP3	1.0	0.0	-0.2	1.0	0.5	0.0	+0.2	0.5	10^{-6}	10^{-6}
RP4	1.0	0.0	-0.2	1.0	0.5	0.0	+0.2	0.5	10^{20}	10^{20}

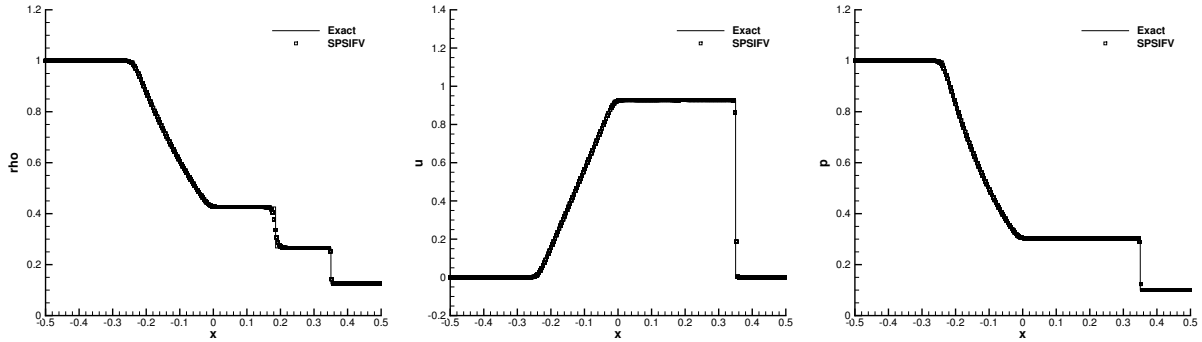


Figure 7: Exact solution of the Euler equations and numerical solution of the GPR model in the stiff relaxation limit ($\tau_1 = \tau_2 = 10^{-6}$) for Riemann problem RP1 (Sod shock tube). The density ρ , the velocity component u and the pressure p are shown at a final time of $t = 0.2$.

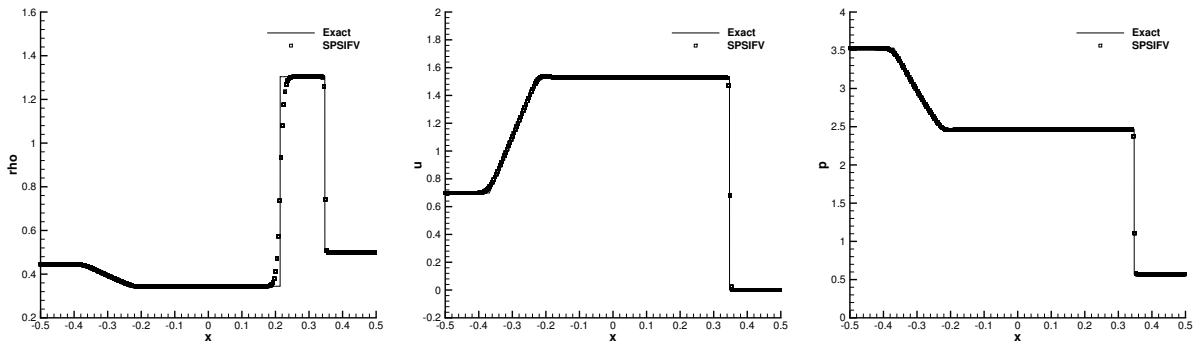


Figure 8: Exact solution of the Euler equations and numerical solution of the GPR model in the stiff relaxation limit ($\tau_1 = \tau_2 = 10^{-6}$) for Riemann problem RP2 (Lax shock tube). The density ρ , the velocity component u and the pressure p are shown at a final time of $t = 0.14$.

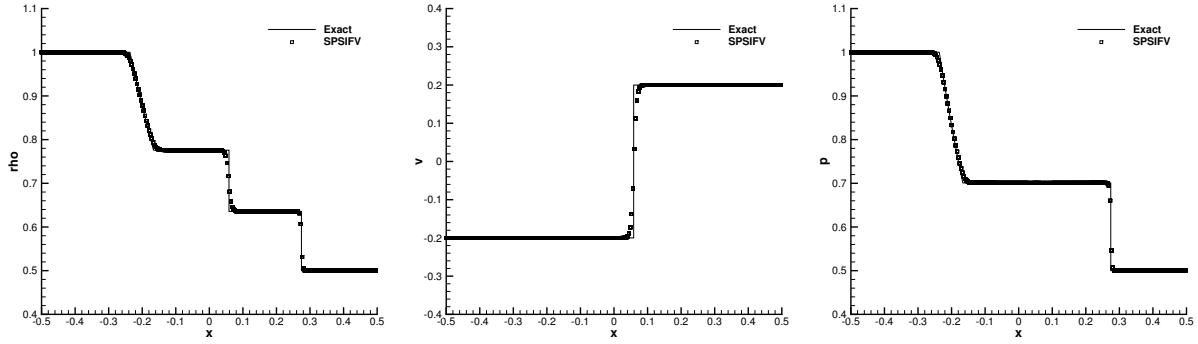


Figure 9: Exact solution of the Euler equations and numerical solution of the GPR model in the stiff relaxation limit ($\tau_1 = \tau_2 = 10^{-6}$) for Riemann problem RP3. The density ρ , the velocity component u and the pressure p are shown at a final time of $t = 0.2$.

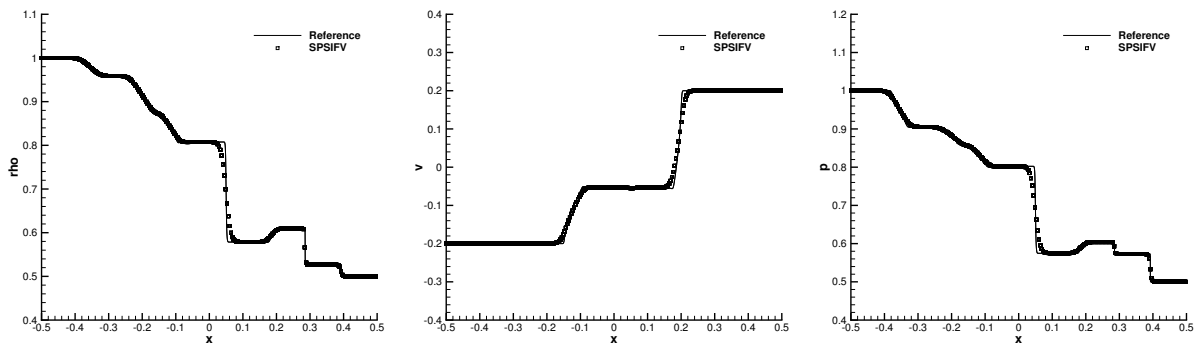


Figure 10: Reference solution and numerical solution of the homogeneous GPR model without source terms ($\tau_1 = \tau_2 = 10^{20}$) for Riemann problem RP4. The density ρ , the velocity component v and the pressure p are shown at a final time of $t = 0.2$. One can note seven waves that are contained in the homogeneous part of the GPR model.

$\lambda = 9\frac{1}{3} \cdot 10^{-2}$. The shock Reynolds number is therefore $Re_s = 100$. The distortion field and the thermal impulse are initially set to $\mathbf{A} = \sqrt[3]{\rho} \mathbf{I}$ and $\mathbf{J} = 0$, respectively. The simulation with the new SPSIFV scheme is run until a final time of $t = 0.2$. The comparison between the numerical solution of the first order hyperbolic GPR model and the exact solution of the compressible Navier-Stokes equations is shown for density ρ , velocity u and pressure p in Fig. 11. One can note an excellent agreement for all quantities.

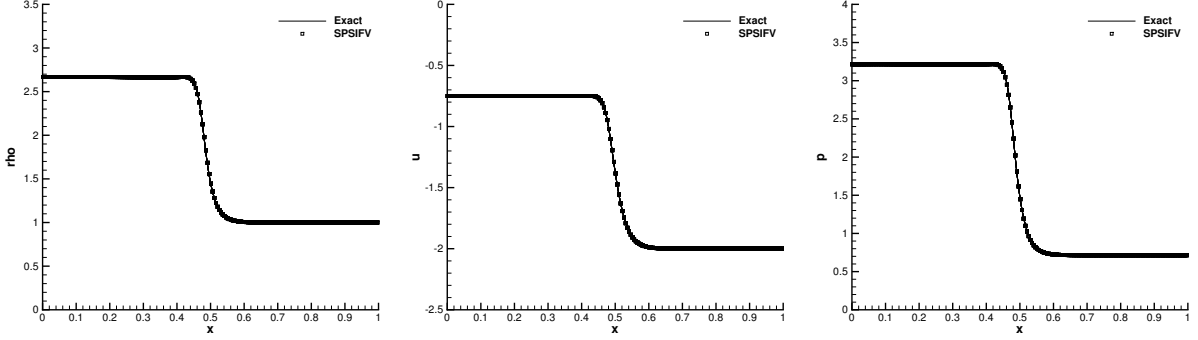


Figure 11: Exact solution of the compressible Navier-Stokes equations and numerical solution of the GPR model for a viscous shock profile at $M = 2$, $Re = 100$ and $Pr = 0.75$.

5.5. 2D Taylor-Green vortex at low Mach number

Here we solve the two-dimensional Taylor-Green vortex at very low Mach numbers, which has an exact solution in the incompressible Navier-Stokes limit (i.e. for $M \rightarrow 0$) that reads

$$u(x, y, t) = \sin(x) \cos(y) e^{-2\gamma t}, \quad (89)$$

$$v(x, y, t) = -\cos(x) \sin(y) e^{-2\gamma t}, \quad (90)$$

$$p(x, y, t) = C + \frac{1}{4}(\cos(2x) + \cos(2y)) e^{-4\gamma t}. \quad (91)$$

In our numerical simulations, the computational domain is chosen as $\Omega = [0, 2\pi]^2$ with periodic boundaries in x and y direction. The GPR model is solved with the new structure-preserving semi-implicit scheme up to a final time of $t = 10$ using a computational grid composed of 200×200 cells. The following set of parameters is used for this test case: $\gamma = 1.4$, $\rho_0 = 1$, $\mu = 10^{-2}$, $c_v = 1$, $c_s = 10$, $\alpha = 1$, $Pr = 1$. The initial conditions for the velocity and the pressure are given by (89)–(91), where the additive constant in the pressure field is set to $C = 10^5$, so that the maximal Mach number in this test problem is $M = 0.0027$. The distortion field and the heat flux are initialized as usual with $\mathbf{A} = \mathbf{I}$ and $\mathbf{J} = 0$.

The L_p error norm of a quantity q with respect to the exact solution q_e at time t^n is in the following defined as

$$L_p(q, t^n) = \sqrt[p]{\frac{1}{|\Omega|} \sum_{r,s} \Delta x \Delta y |q^{n,r,s} - q_e(x^r, y^s, t^n)|^p}, \quad (92)$$

while the L_∞ norm is given as usual by

$$L_\infty(q, t^n) = \max_{r,s} |q^{n,r,s} - q_e(x^r, y^s, t^n)|. \quad (93)$$

The computational results obtained with the new structure-preserving semi-implicit scheme are shown in Fig. 12 at time $t = 10$, where also a comparison with the exact solution of the incompressible Navier-Stokes equations is provided. An excellent agreement between the numerical results and the reference solution can be observed. The distortion field component A_{11} shown in Fig. 12 matches the one presented in [1] very well and reveals the vortex

Table 2: Numerical convergence results of the structure-preserving semi-implicit FV scheme for the GPR model in the stiff relaxation limit using the 2D Taylor-Green vortex problem. The L_1 , L_2 and L_∞ error norms refer to the velocity component u at a final time of $t = 0.2$.

$N_x = N_y$	$L_1(u, 0.2)$	$O(u)$	$L_2(u, 0.2)$	$O(u)$	$L_\infty(u, 0.2)$	$O(u)$
25	9.9081E-03		1.2214E-02		2.4335E-02	
50	2.1079E-03	2.2	2.5905E-03	2.2	5.1097E-03	2.3
100	5.1362E-04	2.0	6.2444E-04	2.1	1.1784E-03	2.1
200	1.3577E-04	1.9	1.6400E-04	1.9	2.9661E-04	2.0

structures of the flow. The total CPU time required by the semi-implicit scheme for this low Mach number test problem on one single CPU core of an Intel i9-7940X CPU was 8607.7s. The entire simulation required 8466 time steps. The time needed for one degree of freedom (element) update (TDU) with the SPSIFV scheme was therefore 25.4 μ s. The L_∞ errors measured for the velocity component u and for the pressure p at the final time $t = 10$ were $L_\infty(u, 10) = 3.6 \cdot 10^{-3}$ and $L_\infty(p, 10) = 3.7 \cdot 10^{-2}$, respectively.

For comparison, we have rerun the same test problem also with an explicit second order accurate MUSCL-Hancock-type TVD finite volume scheme [62], which required 111126.8 s of wall clock time on one core of an Intel i9-7940X CPU. In order to reach the final time a total number of 265418 time steps was necessary, i.e. the time needed to update one degree of freedom with the explicit scheme was TDU = 10.5 μ s. We can conclude that in terms of total wall clock time the new SPSIFV scheme is a factor of **12.9** faster than the explicit scheme for this low Mach number test case. However, in terms of CPU time per degree of freedom update, the semi-implicit finite volume method is only a factor of 2.4 times more expensive than the explicit scheme, despite the need to solve a linear system for the pressure in each Picard iteration in each time step. Last but not least, we also report the L_∞ error norms obtained with the explicit scheme at the final time. They were $L_\infty(u, 10) = 0.49$ and $L_\infty(p, 10) = 0.34$, respectively, which are up to two orders of magnitude larger than the errors obtained with the structure-preserving semi-implicit scheme. It is indeed very well-known that the low Mach number problem affects explicit density-based schemes in a very negative way not only in terms of computational efficiency, but also in terms of accuracy.

We finally use this test problem also in order to perform a numerical convergence study of our scheme in the stiff relaxation limit at low Mach numbers. For this purpose, we set the effective viscosity in the GPR model to $\mu = 10^{-5}$ and run the 2D Taylor-Green vortex on a sequence of successively refined meshes until a final time of $t = 0.2$. We measure the error norms for the velocity component u and compute the resulting convergence order, see Table 2. As expected, the obtained results indicate that the scheme achieves second order of accuracy in space.

5.6. Double shear layer at low Mach number

Here we solve the double shear layer test problem, see [126, 127, 1]. The computational domain is $\Omega = [0, 1]^2$ with periodic boundary conditions everywhere. The initial condition reads

$$u = \begin{cases} \tanh(\tilde{\rho}(y - 0.25)), & \text{if } y \leq 0.5, \\ \tanh(\tilde{\rho}(0.75 - y)), & \text{if } y > 0.5, \end{cases} \quad (94)$$

$$v = \delta \sin(2\pi x), \quad w = 0, \quad \rho = \rho_0 = 1, \quad p = 10^5. \quad (95)$$

With this initial data, the maximum Mach number of the problem is $M = 2.67 \cdot 10^{-3}$, which is about two orders of magnitude less than the Mach number used in [1]. For this test case we set the parameters that determine the shape of the velocity field to $\delta = 0.05$ and $\tilde{\rho} = 30$. Furthermore, we set the viscosity coefficient to $\nu = \mu/\rho_0 = 2 \cdot 10^{-4}$. The other parameters of the GPR model are chosen as $\gamma = 1.4$, $\rho_0 = 1$, $c_v = 1$, $c_s = 8$ and $\alpha = 0$. The initial condition for the distortion field is $\mathbf{A} = \mathbf{I}$ and furthermore we initialize the thermal impulse with $\mathbf{J} = 0$. Simulations are carried out with the new structure-preserving semi-implicit finite volume scheme up to a final time of $t = 1.8$. The computational mesh is composed of 250×250 control volumes. In Fig. 13 the computational results obtained with the SPSIFV

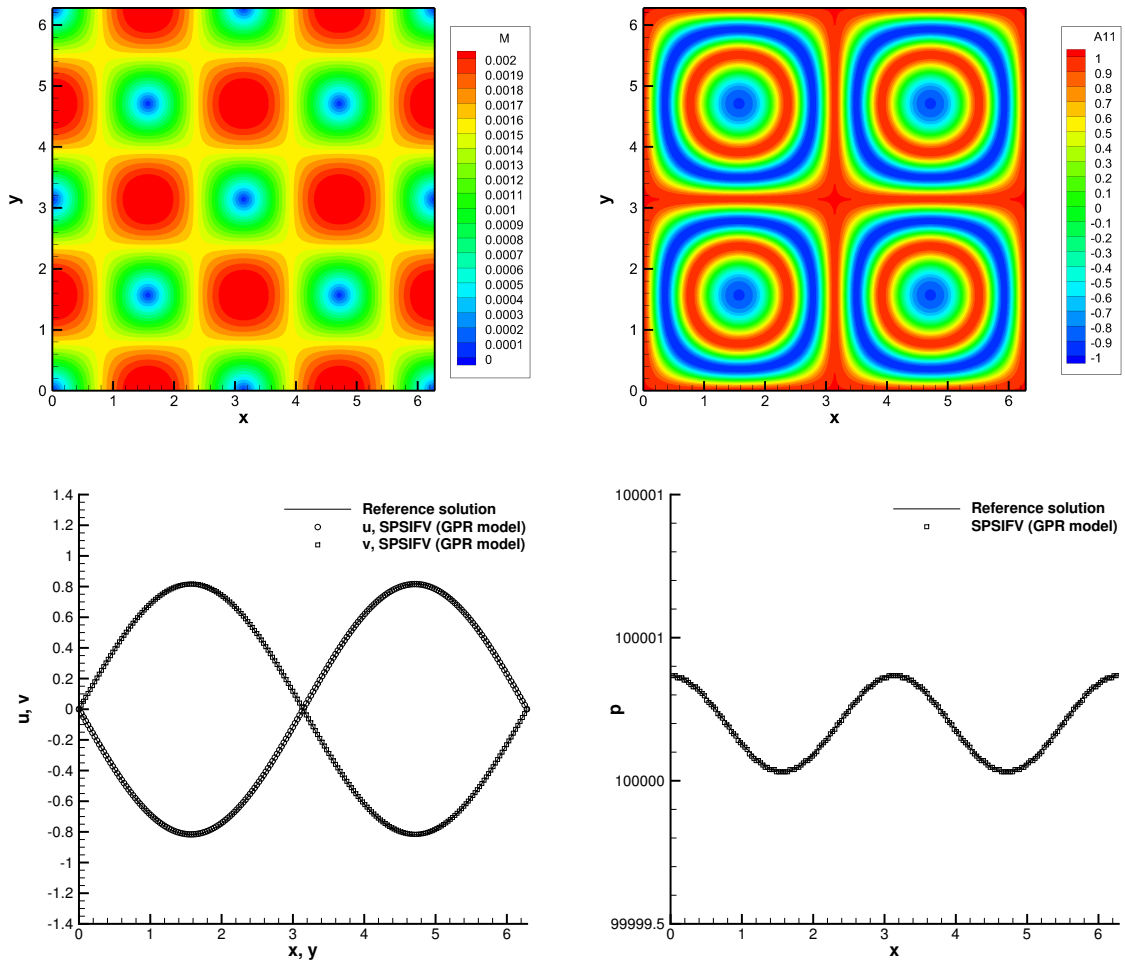


Figure 12: Numerical solution of the GPR model for the Taylor-Green vortex with an effective viscosity of $\nu = 10^{-2}$ at a final time of $t = 10$ using the pressure-based structure-preserving semi-implicit finite volume scheme. Mach number contours (top left) and 21 color contours in the interval $[-1,1]$ of the distortion field component A_{11} (top right). 1D cuts along the x and the y axis and comparison with the exact solution of the incompressible Navier-Stokes equations for the velocity components u and v (bottom left) and 1D cut along the x -axis for the pressure p (bottom right).

scheme applied to the GPR model are compared with a numerical reference solution that is based on the solution of the incompressible Navier-Stokes equations and that has been obtained by a high order staggered semi-implicit space-time discontinuous Galerkin scheme, see [127] for details. The flow dynamics has already been described in [126] and [127] and can be summarized by the development of several vortices from the initially perturbed shear layers. We can note an excellent agreement between the Navier-Stokes reference solution and the numerical solution of the GPR model obtained with the new SPSIFV scheme.

In Fig. 14 we show the temporal evolution of the distortion field component A_{12} , which matches well with the results shown in [1]. As already observed in [1], the components of the field \mathbf{A} seem to be excellent candidates for *flow visualization*, since they reveal even more details of the flow structures than the vorticity plotted in the previous Figure 13. Another major advantage is that the field \mathbf{A} is part of the state vector \mathbf{Q} that is directly evolved in time via the governing PDE. It is *not* a derived flow quantity as the vorticity, which needs to be computed from the velocity field via appropriate post-processing techniques.

5.7. Couette flow at low Mach number

In this section we discuss the Couette flow [130], which is a very elementary but important flow that allows to measure the viscosity of a fluid in rotational viscometers. The setup of the problem used in this paper is as follows: the computational domain is $\Omega = [-0.5, +0.5]^2$, covered by 4×100 control volumes. The boundary conditions in x -direction are periodic. The initial condition for the velocity is $\mathbf{v} = 0$, while density is set to $\rho = 1$ and pressure to $p = 10^4/\gamma$ everywhere in Ω . The initial condition for the distortion field is $\mathbf{A} = \mathbf{I}$ and the thermal impulse is set to $\mathbf{J} = 0$. The remaining parameters of the GPR model are chosen as $\gamma = 1.4$, $\rho_0 = 1$, $c_s = 8$ and $\alpha = 0$. The fluid is set in motion via the upper wall that is moving with velocity $\mathbf{v} = (1, 0, 0)$, while the lower wall in $y = -0.5$ is a non-moving no-slip wall. We set the relaxation time τ_1 so that the viscosity coefficient results as $\mu = 0.1$, hence the Reynolds number based on the wall velocity and the characteristic length of the problem is $Re = 10$. The obtained computational results are shown for various times in Fig. 15, where we also compare the results of the new SPSIFV scheme applied to the GPR model with the semi-implicit finite volume scheme proposed in [67] for the compressible Navier-Stokes equations. We report data for the velocity profile $u(y)$ and of the shear stress tensor component $\sigma_{12}(y)$. One can observe that the match between the numerical solution of the GPR model and the Navier-Stokes reference solution is excellent. For long times ($t = 100$), the well-known linear velocity profile of the Couette flow is reached in both cases and the shear stress becomes constant along the y axis. At this point, it is very interesting to note that the shear stress becomes a constant in both space and time, but the distortion field \mathbf{A} is *not* constant, neither in space nor in time, see Fig. 16, where the time evolution of the shear stress component σ_{12} is plotted together with the time evolution of A_{12} at late times ($95 \leq t \leq 100$). This behaviour was already discussed in [4] and explained by the rotations of fluid elements, which is a geometric information that is contained in the GPR model, but not in the Navier-Stokes equations. Therefore, the Couette flow is *not* a stationary solution of the GPR model, while it is a stationary solution of the Navier-Stokes equations.

5.8. Poiseuille flow at low Mach number

The test case considered here is the steady flow of a viscous Newtonian fluid in a rectangular duct of length L and diameter d in the presence of a constant source term $\mathbf{S} = (0, \mathbf{g}, 0, 0, \mathbf{g} \cdot \mathbf{v})^T$ that is added to the right hand side of the PDE system (1) in order to drive the flow and which can be discretized explicitly together with the convective terms without changing anything else in the numerical scheme. We choose $\mathbf{g} = (1, 0, 0)^T$ and a computational domain $\Omega = [-L/2, L/2] \times [0, d]$ with $L = 1$ and $d = 0.25$ and periodic boundary conditions in x -direction. The source term replaces the pressure gradient $\partial p/\partial x$ that usually drives the *Hagen-Poiseuille flow*, which is a well-known solution of the Navier-Stokes equations and which leads to the parabolic velocity profile

$$u(y) = -\frac{1}{2} \frac{1}{L} \frac{\rho}{\mu} y(y-d). \quad (96)$$

If we run the problem in the low Mach number regime, we can expect Eqn. (96), which is valid for an incompressible fluid, to hold also for the weakly compressible case. We therefore choose the following initial data and set of parameters: $\gamma = 1.4$, $\rho_0 = 1$, $c_v = 1$, $c_s = 8$, $p = 10^4$, $u = v = 0$, $\mathbf{A} = \mathbf{I}$, $\mathbf{J} = 0$, $\alpha = \kappa = 0$ and $\mu = 10^{-2}$. The maximum

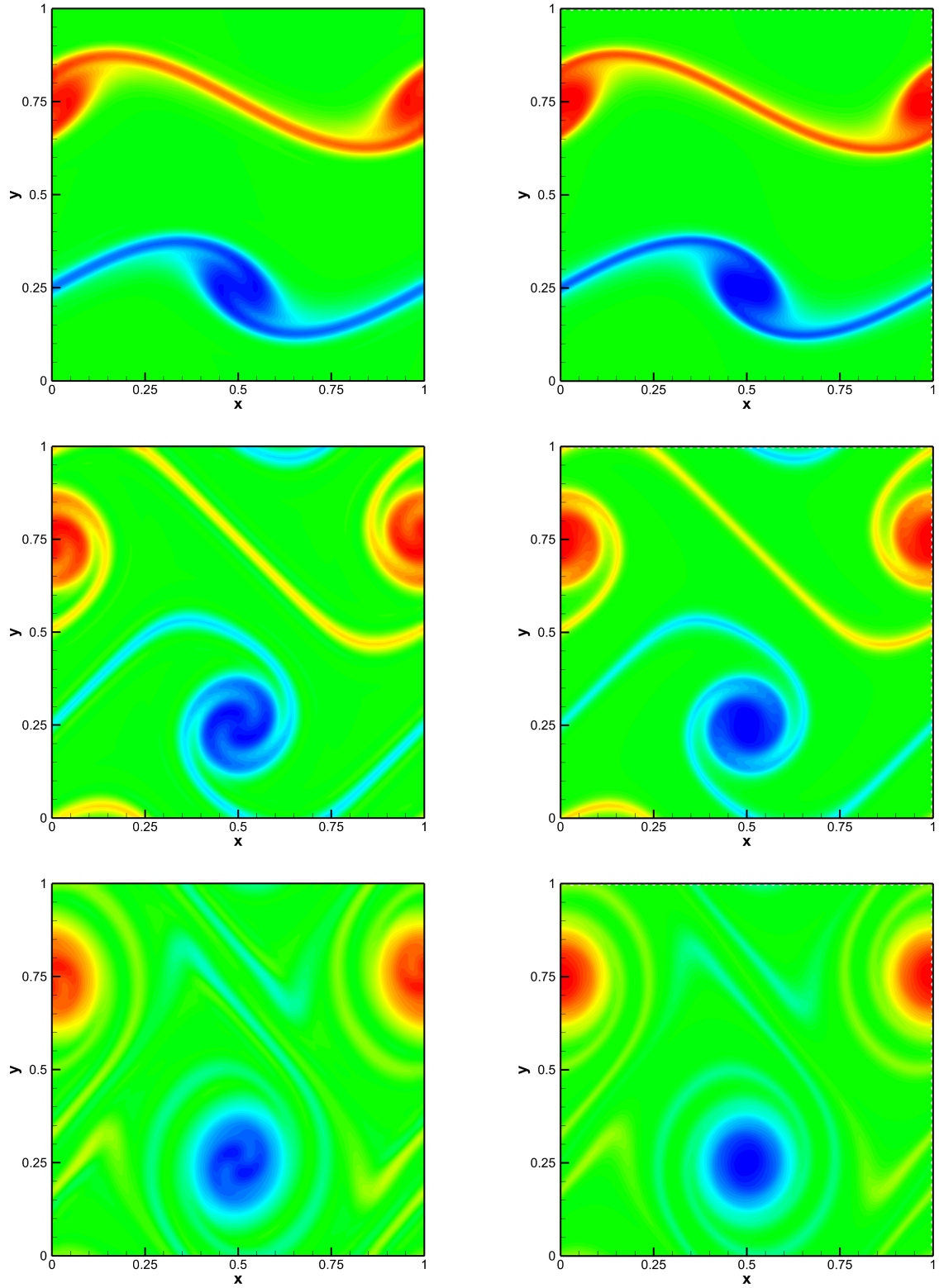


Figure 13: Vorticity contours for the double shear layer with a viscosity of $\mu = 2 \cdot 10^{-4}$ at times $t = 0.8$, $t = 1.2$ and $t = 1.8$ (from top to bottom). Right: reference solution obtained by solving the incompressible Navier-Stokes equations with the staggered semi-implicit space-time DG scheme of Tavelli and Dumbser [128, 129]. Left: numerical solution of the GPR model obtained with the new structure-preserving semi-implicit finite volume scheme.

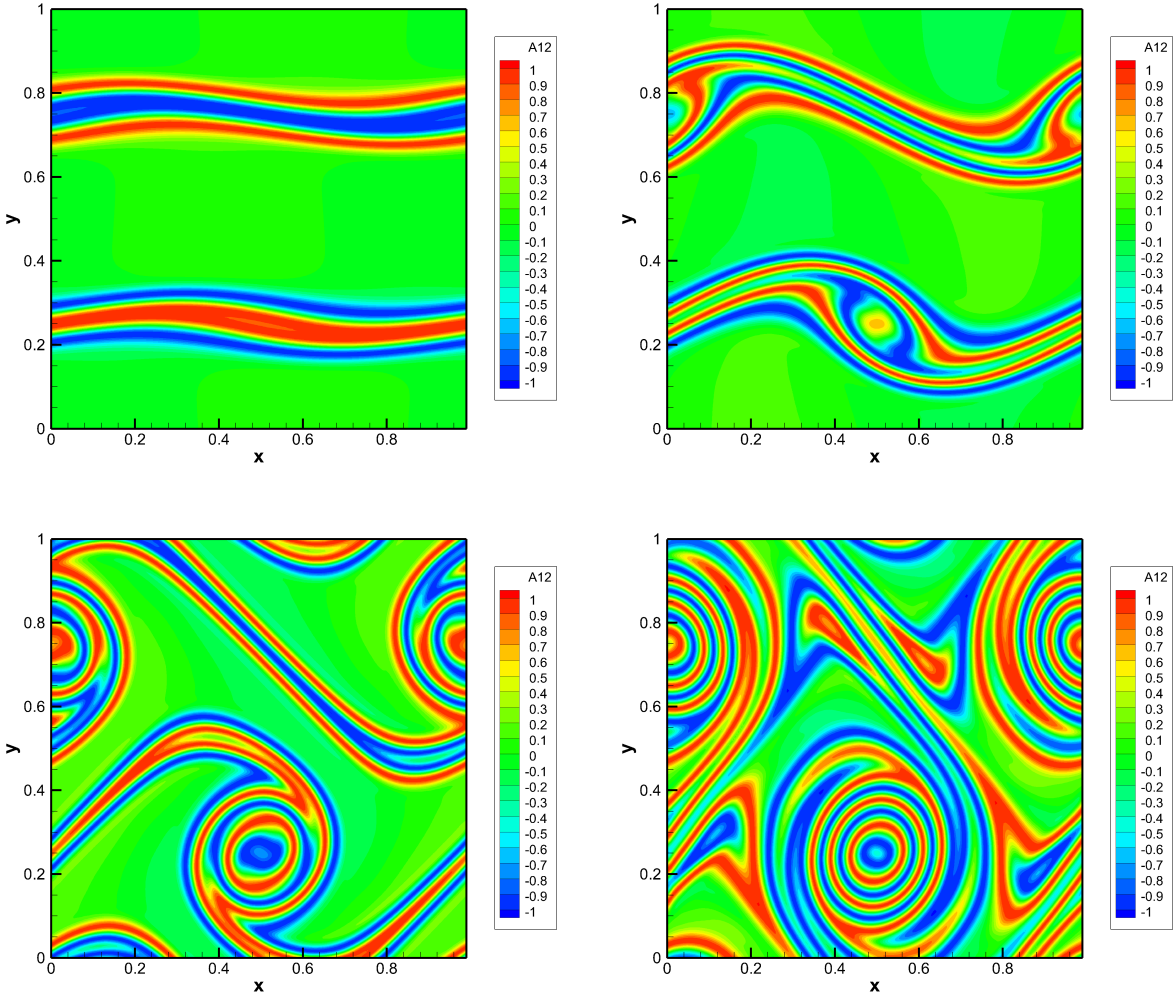


Figure 14: Distortion field component A_{12} obtained for the double shear layer problem at times $t = 0.4$, $t = 0.8$, $t = 1.2$ and $t = 1.8$ by solving the GPR model with the structure-preserving semi-implicit finite volume scheme in the stiff relaxation limit ($\mu = 2 \cdot 10^{-4}$).

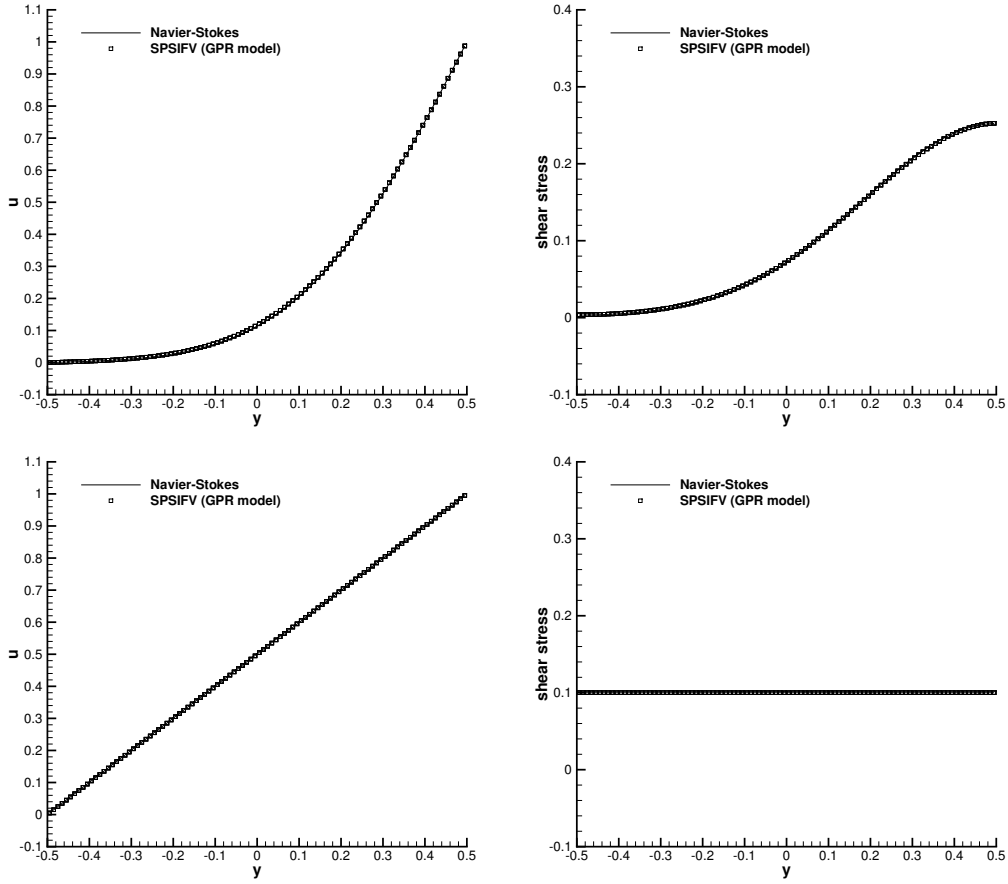


Figure 15: Couette flow at Mach number $M = 10^{-2}$ and Reynolds number $Re = 10$. Results obtained with the new SPSIFV scheme applied to the GPR model and comparison with the Navier-Stokes reference solution at time $t = 0.5$ (top row) and $t = 100$ (bottom row). Velocity component u (left) and shear stress tensor component σ_{12} (right).

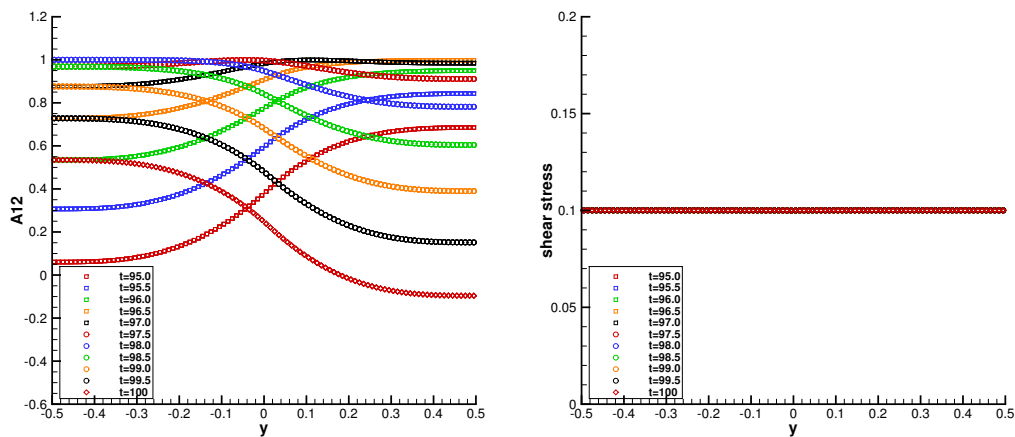


Figure 16: Couette flow at Mach number $M = 10^{-2}$ and Reynolds number $Re = 10$. Temporal evolution of the distortion field component A_{12} from $t = 95$ to $t = 100$ (left) and corresponding temporal evolution of the shear stress component σ_{12} (right). It can clearly be noticed how the unsteady distortion field A_{ik} corresponds to a perfectly stationary shear stress σ_{ik} .

flow velocity is $u_{\max} = 0.78125$, which means the Mach number is $M = 6.6 \cdot 10^{-3}$ and the Reynolds number based on the diameter is $Re_d = u_{\max}d/\nu = 19.5$. The computational domain was discretized with the new structure-preserving semi-implicit finite volume scheme using 10×150 cells and running the problem until a final time of $t = 10$ so that the solution becomes stationary. The obtained computational results are shown in Figure 17, where the velocity contours, the velocity vectors and a comparison with the exact solution of the Hagen-Poiseuille profile (96) are shown. One can observe that the obtained numerical results are in good agreement with the reference solution. Similar to the previous examples of fluid flows, we note a highly heterogeneous profile of the distortion field in Figure 17 despite homogeneous and stationary profile of the velocity and thus, of the viscous stress.

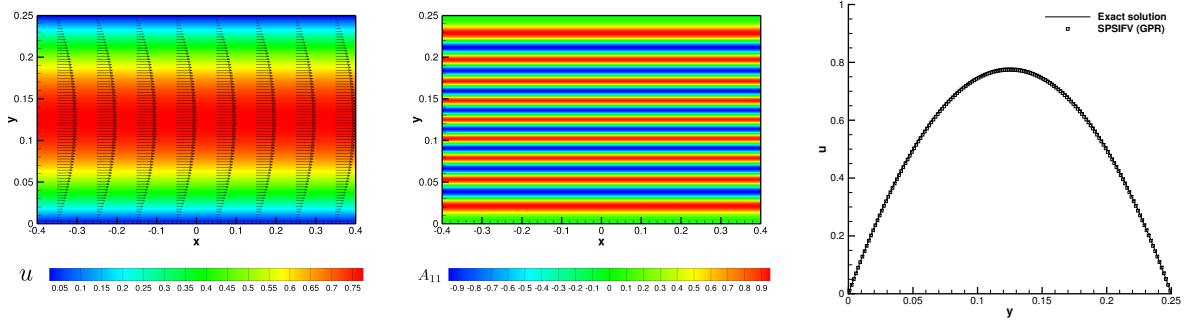


Figure 17: Poiseuille flow at Mach number $M = 6.6 \cdot 10^{-3}$ and Reynolds number $Re_d = 19.5$. Results obtained at time $t = 10$ with the new SPSIFV scheme applied to the GPR model. Velocity vectors and color contours of the velocity component u (left), A_{11} component for the distortion field (middle), and comparison of the velocity component u on a 1D cut along the y axis with the exact solution of the Hagen-Poiseuille flow (right).

5.9. Lid-driven cavity at low Mach number

A classical benchmark problem for the numerical solution of the incompressible Navier-Stokes equations is the well-known lid-driven cavity problem, see e.g. [131, 128]. It can also be used to validate compressible flow solvers in the low Mach number regime, see e.g. [1, 132, 67]. For the computational setup in this paper the computational domain is given by $\Omega = [-0.5, 0.5] \times [-0.5, 0.5]$. The initial condition is simply given by $\rho = 1$, $\mathbf{v} = 0$, $p = 10^4/\gamma$, $\mathbf{A} = \mathbf{I}$ and $\mathbf{J} = 0$. The parameters of the GPR model are set to $\gamma = 1.4$, $c_v = 1$, $c_s = 8$, $\rho_0 = 1$ and $\alpha = 0$, i.e. heat conduction is neglected. The dynamic viscosity is chosen as $\mu = 10^{-2}$ so that the Reynolds number of the test problem is $Re = 100$. The fluid flow inside the cavity is induced by the moving upper boundary, whose velocity is set to $\mathbf{v} = (1, 0, 0)$. On all other boundaries, a no-slip wall boundary condition with $\mathbf{v} = 0$ is imposed. With the chosen initial and boundary conditions, the Mach number of this test problem is $M = 10^{-2}$ with respect to the lid velocity.

The new structure-preserving semi-implicit finite volume scheme is run until a final time of $t = 10$ using a computational grid composed of 200×200 elements. The numerical results are shown in Fig. 18, where also a comparison with the Navier-Stokes reference solution of Ghia *et al.* [131] is provided. We note a very good agreement between the numerical solution of the GPR model and the incompressible Navier-Stokes reference solution. At this point we would like to stress that the new SPSIFV scheme is able to solve this test problem efficiently also at low Mach number, while an explicit method as the one used in [1] would require a very large number of time steps due to the CFL condition based on the sound speed.

At this point, we also provide a quantitative performance comparison of the new SPSIFV scheme with a classical second order MUSCL-Hancock TVD finite volume method, see [62]. All runs are performed on one single core of an Intel i9-7900X CPU with 3.3 GHz nominal clock speed and 32 GB of RAM. The total wall clock time needed by the SPSIFV scheme to reach the final simulation time of $t = 10$ was 2031 s, while the explicit second order MUSCL-Hancock scheme needed 5641 s to complete the simulation. The time needed to update one single control volume was $4.2\mu\text{s}$ for the SPSIFV scheme and $1.9\mu\text{s}$ for the explicit second order TVD method.

The computational efficiency of the semi-implicit scheme can be highlighted even further when increasing the initial pressure to $p = 10^5$, i.e. by further reducing the Mach number of the test problem. In this case, the total wall clock

time needed by the new SPSIFV scheme to reach $t = 10$ was 2666 s, while the explicit MUSCL-Hancock scheme needed 20392 s to complete the simulation. Here, the CPU time for one single element update was $5.5\mu\text{s}$ for the semi-implicit scheme and $1.9\mu\text{s}$ for the explicit TVD scheme.

These results clearly show that the semi-implicit scheme is not only faster for this type of low Mach number problem, as expected, but that also the absolute computational cost per element and time step is quite competitive with the one of the explicit scheme, despite the need to solve a global pressure system in each time step.

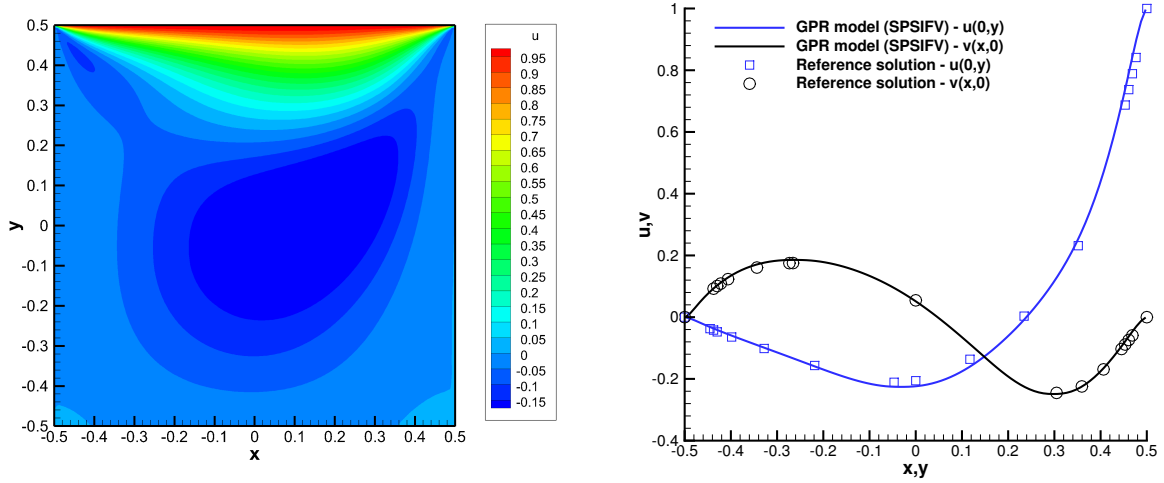


Figure 18: Lid-driven cavity problem at Mach number $M = 10^{-2}$ and Reynolds number $Re = 100$. Results obtained at time $t = 10$ with the new SPSIFV scheme applied to the GPR model. Color contours of the velocity component u (left) and comparison of the velocity components u and v on 1D cuts along the x and y axis with the reference solution of Ghia *et al.* [131] (right).

5.10. 2D explosion problems

In this subsection we consider two circular explosion problems (EP1 and EP2), one in the fluid limit of the model, one in the solid limit. Given the computational domain $\Omega = [-1; 1]^2$ the initial condition reads

$$\mathbf{Q}(x, y, 0) = \begin{cases} \mathbf{Q}_{in} & \text{if } r \leq R \\ \mathbf{Q}_{out} & \text{if } r > R. \end{cases} \quad (97)$$

where \mathbf{Q}_{in} and \mathbf{Q}_{out} are the internal and external states, respectively, and $r = \sqrt{x^2 + y^2}$ is the radial coordinate, while $R = 0.5$.

EP1: Fluid limit of the model. We first solve the governing PDE system in the fluid limit, i.e. $\tau_1 \ll 1$ and $\tau_2 \ll 1$. In the inner state, the density and the pressure are $\rho_{in} = 1$ and $p_{in} = 1$, while in the outer state we impose $\rho_{out} = 0.125$ and $p_{out} = 0.1$. In addition, in the entire domain the initial velocity is set to $\mathbf{v} = 0$, the initial thermal impulse vector is equal to $\mathbf{J} = 0$ and the initial distortion field is imposed as $\mathbf{A} = \sqrt[3]{\rho} \mathbf{I}$. The other parameters of the GPR model are set to $\gamma = 1.4$, $c_v = 2.5$, $\rho_0 = 1$, $\tau_1 = \tau_2 = 10^{-5}$. The computational mesh is composed by 1000×1000 control volumes and the final time of the simulation is $t = 0.2$. Moreover, we compute a reference solution by solving the 1D Euler equations of gasdynamics, where the cylindrical symmetry was properly accounted for via an algebraic source term in the PDE system, see [62] for details. In this case the numerical solution has been obtained by using a robust second order TVD finite volume scheme (see [133, 62]) on a very fine grid. In Figure 19 a density contour plot at the final time is depicted and the numerical results obtained with the SPSIFV scheme are compared against the 1D reference solution. From the obtained results we can observe that the agreement is very good.

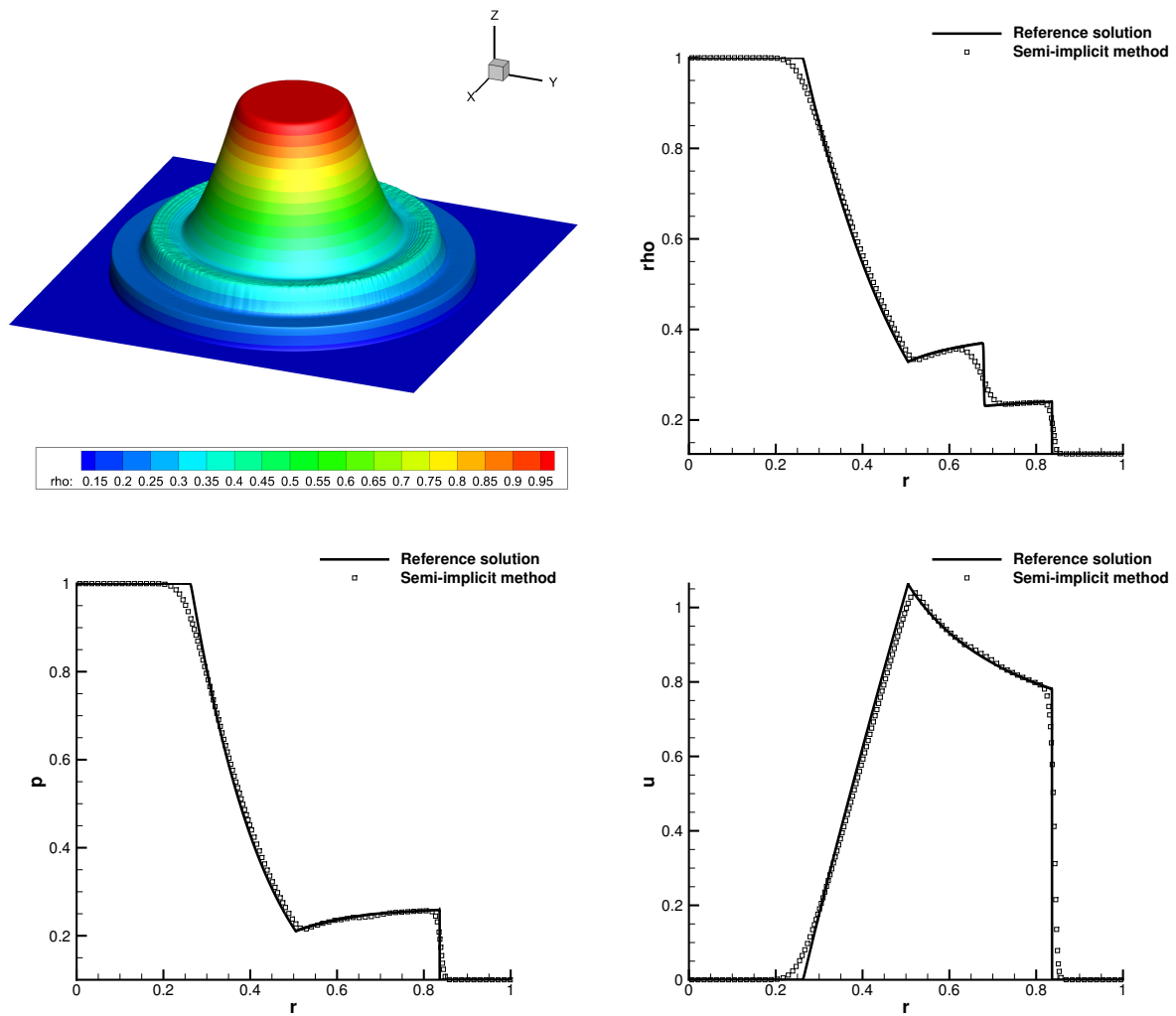


Figure 19: 2D explosion problem EP1 at time $t = 0.2$. 3D density contour color plot (top left) and 1D cut along the x axis with a comparison of the Euler reference solution (solid line) against the numerical solution of the GPR model obtained with the new SPSIFV scheme (square symbols) in the stiff relaxation limit ($\tau_1 = \tau_2 = 10^{-3}$).

EP2: Solid limit of the model. We now solve the governing PDE system in the solid limit, i.e. $\tau_1 \rightarrow \infty$ and $\tau_2 \rightarrow \infty$. Here, we choose the following initial condition. We set $\rho = 1$, $\mathbf{v} = 0$, $\mathbf{A} = \mathbf{I}$ and $\mathbf{J} = 0$ everywhere in the computational domain, while we choose $p_{in} = 2$ and $p_{out} = 1$ for the pressure. The other parameters of the GPR model are set to $\gamma = 1.4$, $c_v = 2.5$, $\rho_0 = 1$, $\tau_1 = \tau_2 = 10^{20}$. The computational mesh is composed of 500×500 and the final simulation time is set to $t = 0.15$. We solve the problem twice, once with the new SPSIFV scheme and another time with a standard second order accurate MUSCL-Hancock finite volume scheme, see [62]. The computational results obtained with both schemes are shown via contour plots and 1D cuts along the x -axis in Figs. 20 and 21, respectively. Overall, we can observe a good agreement between the two solutions. Since we run the present test case with $\tau_1 = \tau_2 = 10^{20}$, i.e. the governing PDE system becomes homogeneous, we can again compare the L_1 error norms of the curl of \mathbf{A} and \mathbf{J} obtained with the two different schemes. As already shown in the first test problem, the new SPSIFV method is able to maintain the error close to machine zero, while the standard TVD finite volume scheme produces errors in the curl of \mathbf{A} and \mathbf{J} that are about ten orders of magnitude larger.

Finally, we also provide detailed CPU times for the two schemes so that the reader can assess the computational efficiency of the proposed SPSIFV scheme. The present test problem is *not* a low Mach number problem, i.e. we expect the semi-implicit scheme to be less efficient than the explicit method. The total CPU time needed by the SPSIFV method on one single core of an Intel i9-7900X CPU with 3.3 GHz of clock frequency and 32 GB of RAM was 298.3 s, while the explicit second order TVD scheme needed 207.2 s, which is only about 31 % less than the semi-implicit scheme. Note that the new semi-implicit scheme needs to solve an implicit pressure system in each time step. The total wall clock time can also be normalized by the number of time steps and by the number of elements, leading to the time that is needed to update one element. The time needed by the SPSIFV scheme for one single element update was $4.4\mu\text{s}$, while it was $2.39\mu\text{s}$ for the explicit second order TVD scheme. From these results we can conclude that the computational efficiency of the proposed semi-implicit finite volume scheme is still competitive even for non low Mach number flows, while it is obviously much faster than an explicit scheme for low Mach number flow problems, see the results obtained for the Taylor-Green vortex and for the lid-driven cavity problem.

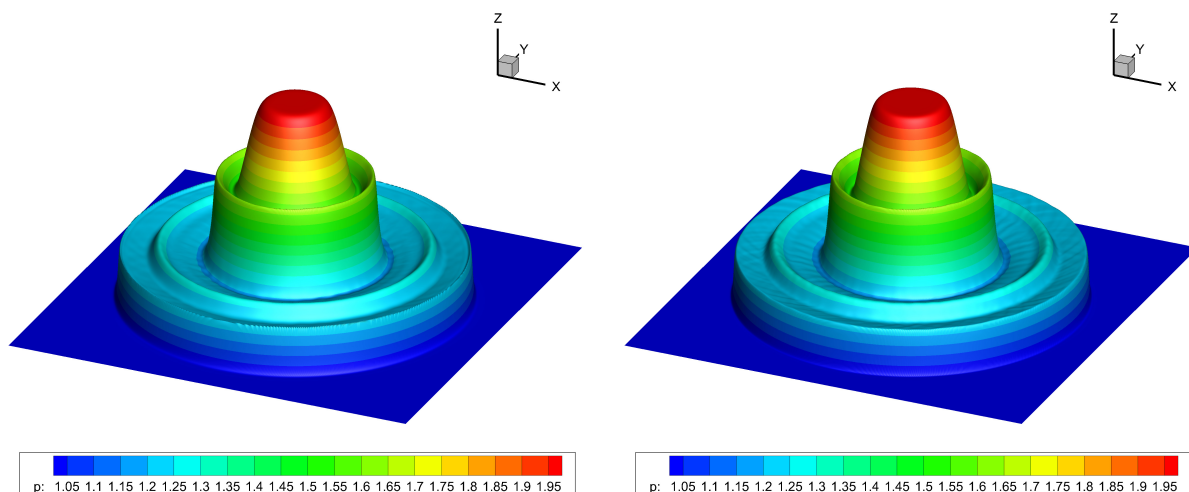


Figure 20: 2D explosion problem EP2 for the homogeneous GPR model with $\tau_1 = \tau_2 = 10^{20}$ at time $t = 0.15$. 3D pressure contour color plot for the new SPSIFV scheme (left) and a standard explicit MUSCL TVD finite volume method (right).

6. Conclusions

We have presented a new structure-preserving staggered semi-implicit finite volume method for the unified GPR model of continuum mechanics. The scheme is consistent with the low Mach number limit of the equations, it is

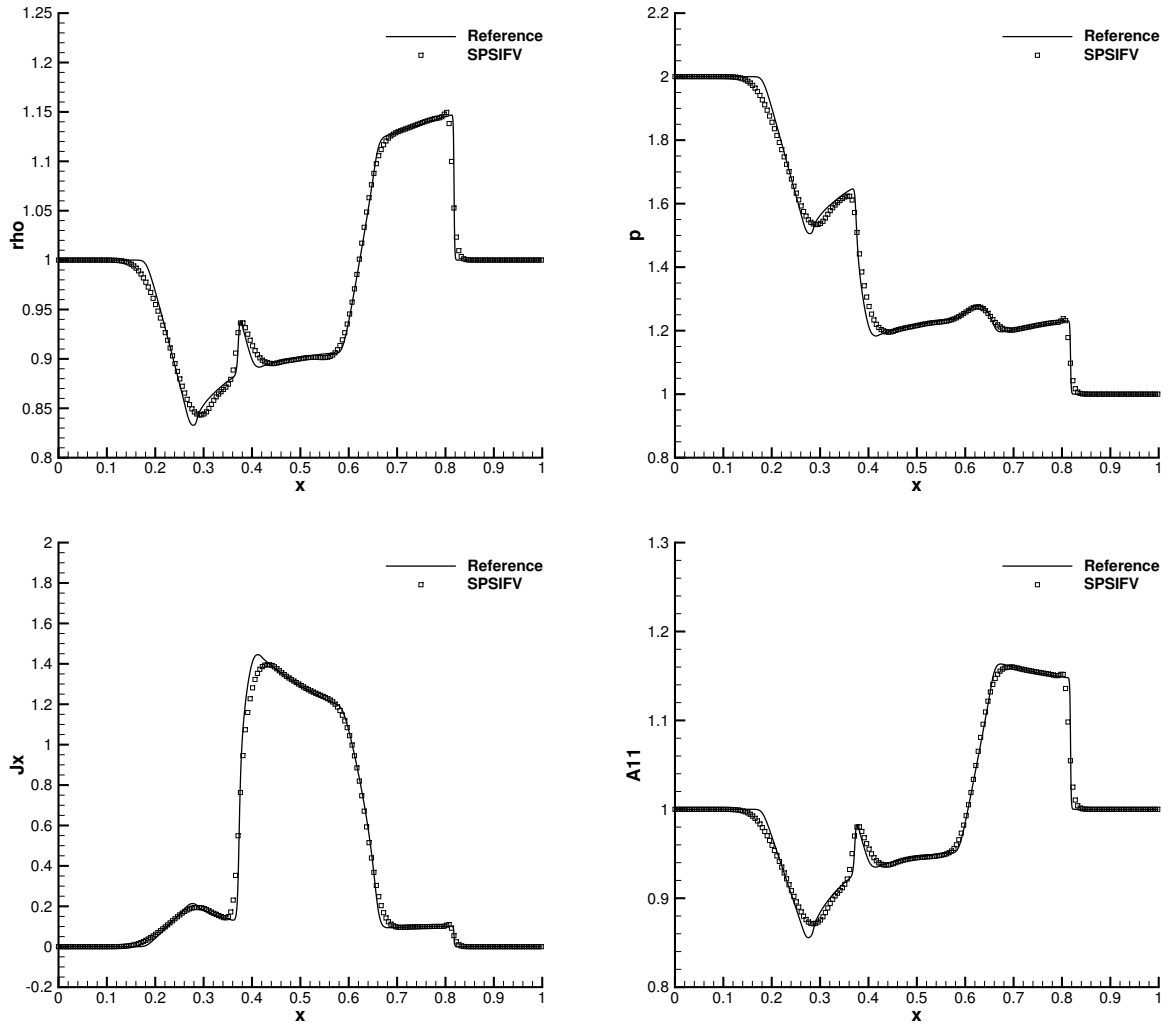


Figure 21: Cut along the x axis for the 2D explosion problem EP2 at time $t = 0.15$. Comparison of a fine grid reference solution (solid line) against the numerical solution of the homogeneous GPR model ($\tau_1 = \tau_2 = 10^{20}$) obtained with the new SPSIFV scheme (square symbols). Density ρ (top left), pressure p (top right), thermal impulse component J_1 (bottom left) and distortion field component A_{11} (bottom right).

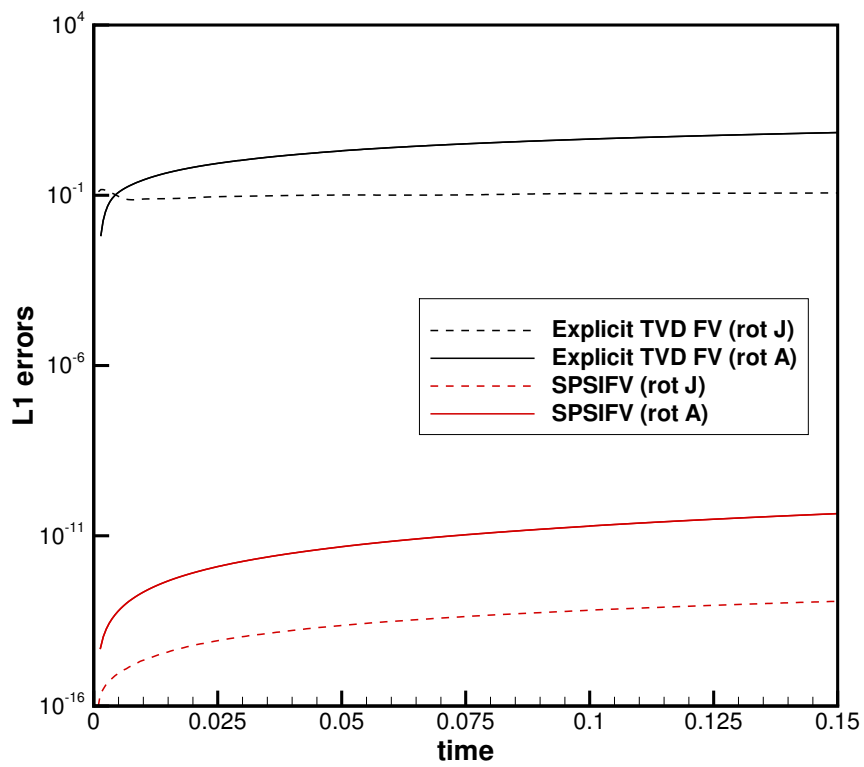


Figure 22: Time series of the L_1 error norms of the curl of \mathbf{A} and \mathbf{J} for the 2D explosion problem EP2 until time $t = 0.15$ using a standard second order MUSCL-Hancock-type TVD finite volume scheme (black) and the new structure-preserving semi-implicit finite volume scheme (red). The new structure-preserving method is able to preserve all curl-free conditions of the GPR model essentially up to machine precision.

exactly curl-free for the homogeneous part of the PDE system in the absence of source terms and is consistent with the Navier-Stokes-Fourier limit of the model in the stiff relaxation limit when $\tau_1 \rightarrow 0$ and $\tau_2 \rightarrow 0$. To the best knowledge of the authors, this is the first time that an exactly curl-free scheme has been proposed for the equations of nonlinear large-strain hyperelasticity in Eulerian coordinates.

Future work will consist in an extension of the present approach to general unstructured meshes in multiple space dimensions and to higher order of accuracy at the aid of staggered semi-implicit discontinuous Galerkin (DG) finite element schemes, following the ideas outlined in [134, 129, 132, 135, 136]. In the near future we also plan an extension of this new family of efficient semi-implicit finite volume schemes to Baer-Nunziato-type models of compressible multi-phase flows [137, 138, 139, 140] and to the conservative two-phase flow model [141, 142], where low Mach number problems are particularly important due to the simultaneous presence of two different phases with substantially different sound speeds. Further extensions will also concern compressible multi-phase flow models with surface tension [99, 34], as well as a recent hyperbolic reformulation of the Schrödinger equation [100], which are also endowed with curl constraints. First preliminary results of the authors indicate that the use of exactly curl-free schemes for hyperbolic models with curl involutions, like the ones proposed in [99, 100] might be as important as the use of exactly divergence-free schemes in the context of the magnetohydrodynamics (MHD) equations.

Acknowledgements

The research presented in this paper was partially funded by the European Union's Horizon 2020 Research and Innovation Programme under the project *ExaHyPE*, grant no. 671698 (call FETHPC-1-2014). The authors also acknowledge funding from the Istituto Nazionale di Alta Matematica (INdAM) through the GNCS group and the program *Young Researchers Funding 2018* via the research project *Semi-implicit structure-preserving schemes for continuum mechanics*. Results by E.R. obtained in Sec. 2 were carried out within the framework of the state contract of the Sobolev Institute of Mathematics (project no. 0314-2019-0012). M.D. and I.P. acknowledges the financial support received from the Italian Ministry of Education, University and Research (MIUR) in the frame of the Departments of Excellence Initiative 2018–2022 attributed to DICAM of the University of Trento (grant L. 232/2016). W.B., M.D. and I.P. also received financial support in the frame of the PRIN Project 2017 (No. 2017KKJP4X entitled *Innovative numerical methods for evolutionary partial differential equations and applications*). MD has also received funding from the University of Trento via the *Strategic Initiative Modeling and Simulation*. I.P. has further received funding from the University of Trento via the *UniTN Starting Grant initiative*.

Appendix A. Sound speeds at the equilibrium

It is likely impossible to get analytical expression for the characteristic speeds of the GPR model (1) in the general case. However, for understanding the type of the waves the model can have, it might be useful to have the formulas for characteristic speeds at the equilibrium, i.e. $\rho = \rho_0$, $\mathbf{A} = \mathbf{I}$, $\mathbf{J} = 0$. Thus, in the equilibrium, the characteristic polynomial reads

$$\tilde{\lambda}^9 (c_s^2 - \tilde{\lambda}^2)^2 (a_0 + a_2 \tilde{\lambda}^2 - a_4 \tilde{\lambda}^4) = 0, \quad (\text{A.1})$$

with $\tilde{\lambda} = \lambda - u$ and where

$$a_0 = \alpha^2 T (4c_s^2 + 3c_v(\gamma - 1)T), \quad (\text{A.2a})$$

$$a_2 = 4c_s^2 c_v + 3(\alpha^2 + c_v^2(\gamma - 1)\gamma)T, \quad (\text{A.2b})$$

$$a_4 = 3c_v, \quad (\text{A.2c})$$

and $T = \partial E_1(\rho, s)/\partial S$ is the equilibrium temperature. Thus, there are 8 types of wave: pure advective waves corresponding to λ^9 , 2 shear waves with characteristic speed $\lambda_s = u \pm c_s$, which may be different out of equilibrium, corresponding to $(c_s^2 - \lambda^2)^2$, 4 thermo-acoustic waves

$$\lambda_{ta} = u \pm \sqrt{\frac{a_2 \mp \sqrt{a_2^2 + 4a_0a_4}}{2a_4}} \quad (\text{A.3})$$

corresponding to $a_0 + a_2\lambda^2 + a_4\lambda^4 = 0$ which couple the the longitudinal waves and two (fast and slow) thermal waves. Note that if we put $\alpha = 0$, then the speeds of the thermo-acoustic waves reduce to $c_l^2 = c_0^2 + \frac{4}{3}c_s^2$, i.e. to the standard expression for the equilibrium speeds of longitudinal waves in solids. The remaining eigenvalues are $\lambda_a = u$ associated with pure advection.

References

- [1] M. Dumbser, I. Peshkov, E. Romenski, O. Zanotti, High order ADER schemes for a unified first order hyperbolic formulation of continuum mechanics: Viscous heat-conducting fluids and elastic solids, *Journal of Computational Physics* 314 (2016) 824–862.
- [2] S. Godunov, An interesting class of quasilinear systems, *Dokl. Akad. Nauk SSSR* 139(3) (1961) 521–523.
- [3] S. K. Godunov, E. I. Romenski, Nonstationary equations of the nonlinear theory of elasticity in Euler coordinates., *Journal of Applied Mechanics and Technical Physics* 13 (1972) 868–885.
- [4] I. Peshkov, E. Romenski, A hyperbolic model for viscous Newtonian flows, *Continuum Mechanics and Thermodynamics* 28 (2016) 85–104.
- [5] E. Romenski, Hyperbolic systems of thermodynamically compatible conservation laws in continuum mechanics, *Mathematical and computer modelling* 28(10) (1998) 115–130.
- [6] K. Yee, Numerical solution of initial voundary value problems involving Maxwell equation in isotropic media, *IEEE Trans. Antenna Propagation* 14 (1966) 302–307.
- [7] C. DeVore, Flux-corrected transport techniques for multidimensional compressible magnetohydrodynamics, *Journal of Computational Physics* 92 (1991) 142–160.
- [8] D. Balsara, D. Spicer, A staggered mesh algorithm using high order godunov fluxes to ensure solenoidal magnetic fields in magnetohydrodynamic simulations, *Journal of Computational Physics* 149 (1999) 270–292.
- [9] D. Balsara, Second-order accurate schemes for magnetohydrodynamics with divergence-free reconstruction, *The Astrophysical Journal Supplement Series* 151 (2004) 149–184.
- [10] T. Gardiner, J. Stone, An unsplit Godunov method for ideal MHD via constrained transport, *Journal of Computational Physics* 205 (2005) 509–539.
- [11] D. Balsara, Multidimensional HLLE Riemann solver: Application to Euler and magnetohydrodynamic flows, *Journal of Computational Physics* 229 (2010) 1970–1993.
- [12] D. Balsara, M. Dumbser, Divergence-free MHD on unstructured meshes using high order finite volume schemes based on multidimensional Riemann solvers, *Journal of Computational Physics* 299 (2015) 687–715.
- [13] K. Powell, An approximate Riemann solver for magnetohydrodynamics (that works in more than one dimension), *Tech. Rep. ICASE-Report 94-24 (NASA CR-194902)*, NASA Langley Research Center, Hampton, VA (1994).
- [14] S. Godunov, Symmetric form of the magnetohydrodynamic equation, *Numerical Methods for Mechanics of Continuum Medium* 3 (1) (1972) 26–34.
- [15] C. Munz, P. Omnes, R. Schneider, E. Sonnendrücker, U. Voss, Divergence Correction Techniques for Maxwell Solvers Based on a Hyperbolic Model, *Journal of Computational Physics* 161 (2000) 484–511.
- [16] A. Dedner, F. Kemm, D. Kröner, C. D. Munz, T. Schnitzer, M. Wesenberg, Hyperbolic divergence cleaning for the MHD equations, *Journal of Computational Physics* 175 (2002) 645–673.
- [17] N. Favrie, S. Gavriljuk, S. Ndanou, A thermodynamically compatible splitting procedure in hyperelasticity, *Journal of Computational Physics* 270 (2014) 300–324.
- [18] J. Haider, C. Lee, A. Gil, J. Bonet, A first-order hyperbolic framework for large strain computational solid dynamics: An upwind cell centred total Lagrangian scheme, *International Journal for Numerical Methods in Engineering* 109 (2017) 407–456.
- [19] J. Hyman, M. Shashkov, Natural discretizations for the divergence, gradient, and curl on logically rectangular grids, *Computers and Mathematics with Applications* 33 (1997) 81–104.
- [20] R. Jeltsch, M. Torrilhon, On curl-preserving finite volume discretizations for shallow water equations, *BIT Numerical Mathematics* 46 (2006) S35–S53.
- [21] M. Torrilhon, M. Fey, Constraint-preserving upwind methods for multidimensional advection equations, *SIAM Journal on Numerical Analysis* 42 (2004) 1694–1728.
- [22] G. Margolin, M. Shashkov, P. Smolarkiewicz, A discrete operator calculus for finite difference approximations, *Computer Methods in Applied Mechanics and Engineering* 187 (2000) 365–383.
- [23] K. Lipnikov, G. Manzini, M. Shashkov, Mimetic finite difference method, *Journal of Computational Physics* 257 (2014) 1163–1227.
- [24] T. Carney, N. Morgan, S. Sambasivan, M. Shashkov, A cell-centered Lagrangian Godunov-like method for solid dynamics, *Computers and Fluids* 83 (2013) 33–47.
- [25] E. Deriaz, V. Perrier, Orthogonal helmholtz decomposition in arbitrary dimension using divergence-free and curl-free wavelets, *Applied and Computational Harmonic Analysis* 26 (2009) 249–269.
- [26] J. Nédélec, Mixed finite elements in R3, *Numerische Mathematik* 35 (1980) 315–341.
- [27] J. Nédélec, A new family of mixed finite elements in R3, *Numerische Mathematik* 50 (1986) 57–81.
- [28] J. Cantarella, D. DeTurck, H. Gluck, Vector calculus and the topology of domains in 3-space, *Am. Math. Mon.* 109 (2002) 409–442.
- [29] R. Hiptmair, Finite elements in computational electromagnetism, *Acta Numerica* 11 (2002) 237–339.
- [30] P. Monk, *Finite Element Methods for Maxwell’s Equations*, Oxford University Press, Oxford, 2003.
- [31] D. Arnold, R. Falk, R. Winther, Finite element exterior calculus, homological techniques, and applications, *Acta Numerica* 15 (2006) 1–155.
- [32] A. A. Rodriguez, A. Valli, Finite element potentials, *Applied Numerical Mathematics* 95 (2015) 2–14.
- [33] M. Dumbser, F. Fambri, E. Gaburro, A. Reinartz, On GLM curl cleaning for a first order reduction of the CCZ4 formulation of the Einstein field equations, *Journal of Computational Physics* 404 (2020) 109088.

- [34] S. Chiochetti, I. Peshkov, S. Gavrilyuk, M. Dumbser, High order ADER schemes and GLM curl cleaning for a first order hyperbolic formulation of compressible flow with surface tension (2020).
URL <http://arxiv.org/abs/2002.08818>
- [35] M. Dumbser, S. Chiochetti, I. Peshkov, On numerical methods for hyperbolic PDE with curl involutions, in: G. Demidenko, E. Romenski, E. Toro, M. Dumbser (Eds.), *Continuum Mechanics, Applied Mathematics and Scientific Computing: Godunov's Legacy*, Springer, 2020, pp. 125–134.
- [36] F. Harlow, J. Welch, Numerical calculation of time-dependent viscous incompressible flow of fluid with a free surface, *Physics of Fluids* 8 (1965) 2182–2189.
- [37] A. Chorin, A numerical method for solving incompressible viscous flow problems, *Journal of Computational Physics* 2 (1967) 12–26.
- [38] A. Chorin, Numerical solution of the Navier–Stokes equations, *Mathematics of Computation* 23 (1968) 341–354.
- [39] V. Patankar, *Numerical Heat Transfer and Fluid Flow*, Hemisphere Publishing Corporation, 1980.
- [40] V. Patankar, B. Spalding, A calculation procedure for heat, mass and momentum transfer in three-dimensional parabolic flows, *International Journal of Heat and Mass Transfer* 15 (1972) 1787–1806.
- [41] J. Bell, P. Colella, H. Glaz, A second-order projection method for the incompressible Navier–Stokes equations, *Journal of Computational Physics* 85 (1989) 257–283.
- [42] J. van Kan, A second-order accurate pressure correction method for viscous incompressible flow, *SIAM Journal on Scientific and Statistical Computing* 7 (1986) 870–891.
- [43] C. W. Hirt, B. D. Nichols, Volume of fluid (VOF) method for dynamics of free boundaries, *Journal of Computational Physics* 39 (1981) 201–225.
- [44] V. Casulli, Semi-implicit finite difference methods for the two-dimensional shallow water equations, *Journal of Computational Physics* 86 (1990) 56–74.
- [45] V. Casulli, R. T. Cheng, Semi-implicit finite difference methods for three-dimensional shallow water flow, *International Journal for Numerical Methods in Fluids* 15 (1992) 629–648.
- [46] V. Casulli, A semi-implicit finite difference method for non-hydrostatic free-surface flows, *International Journal for Numerical Methods in Fluids* 30 (1999) 425–440.
- [47] V. Casulli, R. A. Walters, An unstructured grid, three-dimensional model based on the shallow water equations, *International Journal for Numerical Methods in Fluids* 32 (2000) 331–348.
- [48] V. Casulli, A high-resolution wetting and drying algorithm for free-surface hydrodynamics, *International Journal for Numerical Methods in Fluids* 60 (2009) 391–408.
- [49] V. Casulli, A semi-implicit numerical method for the free-surface Navier–Stokes equations, *International Journal for Numerical Methods in Fluids* 74 (2014) 605–622.
- [50] S. Busto, J. Ferrín, E. Toro, M. Vázquez-Cendón, A projection hybrid high order finite volume/finite element method for incompressible turbulent flows, *Journal of Computational Physics* 353 (2018) 169 – 192.
- [51] A. Bermúdez, S. Busto, M. Dumbser, J. Ferrín, L. Saavedra, M. Vázquez-Cendón, A projection hybrid high order finite volume/finite element method for incompressible turbulent flows, *Journal of Computational Physics*.
- [52] V. Casulli, D. Greenspan, Pressure method for the numerical solution of transient, compressible fluid flows, *International Journal for Numerical Methods in Fluids* 4 (11) (1984) 1001–1012.
- [53] P. Lax, B. Wendroff, Systems of conservation laws, *Communications in Pure and Applied Mathematics* 13 (1960) 217–237.
- [54] S. Godunov, Finite difference methods for the computation of discontinuous solutions of the equations of fluid dynamics, *Mat. Sb.* 47 (1959) 271–306.
- [55] P. Roe, Approximate Riemann solvers, parameter vectors, and difference schemes, *Journal of Computational Physics* 43 (1981) 357–372.
- [56] S. Osher, F. Solomon, Upwind difference schemes for hyperbolic conservation laws, *Math. Comput.* 38 (1982) 339–374.
- [57] A. Harten, P. Lax, B. van Leer, On upstream differencing and Godunov-type schemes for hyperbolic conservation laws, *SIAM Review* 25 (1) (1983) 35–61.
- [58] B. Einfeldt, C. D. Munz, P. L. Roe, B. Sjögren, On Godunov-type methods near low densities, *Journal of Computational Physics* 92 (1991) 273–295.
- [59] C. D. Munz, On Godunov-type schemes for Lagrangian gas dynamics, *SIAM Journal on Numerical Analysis* 31 (1994) 17–42.
- [60] E. F. Toro, M. Spruce, W. Speares, Restoration of the contact surface in the Harten-Lax-van Leer Riemann solver, *Journal of Shock Waves* 4 (1994) 25–34.
- [61] R. J. LeVeque, *Finite Volume Methods for Hyperbolic Problems*, Cambridge University Press, 2002.
- [62] E. F. Toro, *Riemann Solvers and Numerical Methods for Fluid Dynamics*, 3rd Edition, Springer, 2009.
- [63] J. Park, C. Munz, Multiple pressure variables methods for fluid flow at all mach numbers, *International Journal for Numerical Methods in Fluids* 49 (2005) 905–931.
- [64] F. Cordier, P. Degond, A. Kumbaro, An Asymptotic-Preserving all-speed scheme for the Euler and Navier-Stokes equations, *Journal of Computational Physics* 231 (2012) 5685–5704.
- [65] N. Kwatra, J. Su, J. Grétarsson, R. Fedkiw, A method for avoiding the acoustic time step restriction in compressible flow, *Journal of Computational Physics* 228 (2009) 4146–4161.
- [66] P. Smolarkiewicz, J. Szmelter, Iterated upwind schemes for gas dynamics, *Journal of Computational Physics* 228 (2009) 33–54.
- [67] M. Dumbser, V. Casulli, A conservative, weakly nonlinear semi-implicit finite volume method for the compressible Navier-Stokes equations with general equation of state, *Applied Mathematics and Computation* 272 (2016) 479–497.
- [68] S. Boscarino, G. Russo, L. Scandurra, All Mach number second order semi-implicit scheme for the Euler equations of gasdynamics, *Journal of Scientific Computing* 77 (2018) 850–884.
- [69] M. Dumbser, D. Balsara, M. Tavelli, F. Fambri, A divergence-free semi-implicit finite volume scheme for ideal, viscous and resistive magnetohydrodynamics, *International Journal for Numerical Methods in Fluids* 89 (2019) 16–42.
- [70] E. Abbate, A. Iollo, G. Puppo, An asymptotic-preserving all-speed scheme for fluid dynamics and nonlinear elasticity, *SIAM Journal on*

- Scientific Computing 41 (2019) A2850–A2879.
- [71] S. K. Godunov, E. I. Romenski, Thermodynamics, conservation laws, and symmetric forms of differential equations in mechanics of continuous media, in: *Computational Fluid Dynamics Review* 95, John Wiley, NY, 1995, pp. 19–31.
 - [72] S. K. Godunov, E. I. Romenski, *Elements of Continuum Mechanics and Conservation Laws*, Kluwer Academic/ Plenum Publishers, 2003.
 - [73] P. T. Barton, D. Drikakis, E. Romenski, V. A. Titarev, Exact and approximate solutions of riemann problems in non-linear elasticity, *Journal of Computational Physics* 228 (2009) 7046–7068.
 - [74] N. Favrie, S. L. Gavrilyuk, R. Saurel, Solid–fluid diffuse interface model in cases of extreme deformations, *Journal of computational physics* 228 (16) (2009) 6037–6077.
 - [75] G. Kluth, B. Després, Discretization of hyperelasticity on unstructured mesh with a cell-centered Lagrangian scheme, *Journal of Computational Physics* 229 (24) (2010) 9092–9118.
 - [76] N. Favrie, S. Gavrilyuk, Diffuse interface model for compressible fluid-compressible elastic-plastic solid interaction, *Journal of Computational Physics* 231 (2012) 2695–2723.
 - [77] S. Ndanou, N. Favrie, S. Gavrilyuk, Criterion of hyperbolicity in hyperelasticity in the case of the stored energy in separable form, *Journal of Elasticity* 115 (2014) 1–25.
 - [78] W. Boscheri, M. Dumbser, R. Loubère, Cell centered direct Arbitrary-Lagrangian-Eulerian ADER-WENO finite volume schemes for non-linear hyperelasticity, *Computers and Fluids* 134–135 (2016) 111–129.
 - [79] I. Peshkov, M. Pavelka, E. Romenski, M. Grmela, Continuum mechanics and thermodynamics in the Hamilton and the Godunov-type formulations, *Continuum Mechanics and Thermodynamics* 30 (6) (2018) 1343–1378.
 - [80] A. de Brauer, A. Iollo, T. Milcent, A Cartesian Scheme for Compressible Multimaterial Hyperelastic Models with Plasticity, *Communications in Computational Physics* 22 (2017) 1362–1384.
 - [81] I. Peshkov, W. Boscheri, R. Loubère, E. Romenski, M. Dumbser, Theoretical and numerical comparison of hyperelastic and hypoelastic formulations for Eulerian non-linear elastoplasticity, *Journal of Computational Physics* 387 (2019) 481–521.
 - [82] H. Jackson, N. Nikiforakis, A unified Eulerian framework for multimaterial continuum mechanics, *Journal of Computational Physics* 401 (2019) 109022.
 - [83] H. Jackson, N. Nikiforakis, A numerical scheme for non-Newtonian fluids and plastic solids under the GPR model, *Journal of Computational Physics* 387 (2019) 410–429.
 - [84] P. Barton, D. Drikakis, E. Romenski, An Eulerian finite-volume scheme for large elastoplastic deformations in solids, *International Journal for Numerical Methods in Engineering* 81 (2010) 453–484.
 - [85] P. Barton, B. Obadia, D. Drikakis, A conservative level-set based method for compressible solid/fluid problems on fixed grids, *Journal of Computational Physics* 230 (2011) 7867–7890.
 - [86] P. Barton, An interface-capturing Godunov method for the simulation of compressible solid-fluid problems, *Journal of Computational Physics* 390 (2019) 25–50.
 - [87] S. Busto, S. Chiochetti, M. Dumbser, E. Gaburro, I. Peshkov, High order ader schemes for continuum mechanics, *Frontiers in Physics* 8 (2020) 32. doi : 10. 3389/ fphy . 2020. 00032.
 - [88] J. Bonet, A. Gil, C. Lee, M. Aguirre, R. Ortigosa, A first order hyperbolic framework for large strain computational solid dynamics. Part I: Total Lagrangian isothermal elasticity, *Computer Methods in Applied Mechanics and Engineering* 283 (2015) 689–732.
 - [89] J. Haider, C. H. Lee, A. J. Gil, J. Bonet, A first-order hyperbolic framework for large strain computational solid dynamics: An upwind cell centred Total Lagrangian scheme, *International Journal for Numerical Methods in Engineering* 109 (3) (2017) 407–456.
 - [90] L. Brugnano, V. Casulli, Iterative solution of piecewise linear systems, *SIAM Journal on Scientific Computing* 30 (2007) 463–472.
 - [91] L. Brugnano, V. Casulli, Iterative solution of piecewise linear systems and applications to flows in porous media, *SIAM Journal on Scientific Computing* 31 (2009) 1858–1873.
 - [92] V. Casulli, P. Zanolli, A nested Newton–type algorithm for finite volume methods solving Richards’ equation in mixed form, *SIAM Journal on Scientific Computing* 32 (2009) 2255–2273.
 - [93] V. Casulli, P. Zanolli, Iterative solutions of mildly nonlinear systems, *Journal of Computational and Applied Mathematics* 236 (2012) 3937–3947.
 - [94] D. Balsara, R. Käppeli, W. Boscheri, M. Dumbser, Curl constraint-preserving reconstruction and the guidance it gives for mimetic scheme designSubmitted.
 - [95] M. Dumbser, I. Peshkov, E. Romenski, O. Zanotti, High order ADER schemes for a unified first order hyperbolic formulation of Newtonian continuum mechanics coupled with electro-dynamics, *Journal of Computational Physics* 348 (2017) 298–342.
 - [96] H. C. Öttinger, *Beyond Equilibrium Thermodynamics*, John Wiley and Sons, Inc., 2005.
 - [97] M. Pavelka, V. Klika, M. Grmela, *Multiscale Thermo-Dynamics*, De Gruyter, Berlin, Boston, 2018. doi : 10. 1515/9783110350951.
 - [98] E. Romenski, A. A. Belozarov, I. M. Peshkov, Conservative formulation for compressible multiphase flows, *Quarterly of Applied Mathematics* 74 (1) (2016) 113–136.
 - [99] K. Schmidmayer, F. Petitpas, E. Daniel, N. Favrie, S. Gavrilyuk, A model and numerical method for compressible flows with capillary effects, *Journal of Computational Physics* 334 (2017) 468–496.
 - [100] F. Dhaouadi, N. Favrie, S. Gavrilyuk, Extended Lagrangian approach for the defocusing nonlinear Schrödinger equation, *Studies in Applied Mathematics* (2018) 1–20.
 - [101] S. K. Godunov, T. Y. Mikhaïlova, E. I. Romenskii, Systems of thermodynamically coordinated laws of conservation invariant under rotations, *Siberian Mathematical Journal* 37 (4) (1996) 690–705. doi : 10. 1007/BF02104662.
 - [102] E. I. Romenski, Thermodynamics and hyperbolic systems of balance laws in continuum mechanics, in: E. Toro (Ed.), *Godunov Methods: Theory and Applications*, Springer US, New York, 2001, pp. 745–761. doi : 10. 1007/978-1-4615-0663-8.
 - [103] I. Peshkov, E. Romenski, M. Dumbser, Continuum mechanics with torsion, *Continuum Mechanics and Thermodynamics* 31 (2019) 1517–1541.
 - [104] K. Powell, P. Roe, T. Linde, T. Gombosi, D. D. Zeeuw, A solution-adaptive upwind scheme for ideal magnetohydrodynamics, *Journal of Computational Physics* 154 (1999) 284–309.

- [105] S. K. Godunov, Symmetric form of the magnetohydrodynamic equation, *Numerical Methods for Mechanics of Continuum Medium* 3 (1) (1972) 26–34.
- [106] P. J. Morrison, Structure and structure-preserving algorithms for plasma physics, *Physics of Plasmas* 24 (5) (2017) 055502.
- [107] E. Toro, M. Vázquez-Cendón, Flux splitting schemes for the Euler equations, *Computers and Fluids* 70 (2012) 1–12.
- [108] S. Klainermann, A. Majda, Singular limits of quasilinear hyperbolic systems with large parameters and the incompressible limit of compressible fluid, *Communications on Pure and Applied Mathematics* 34 (1981) 481–524.
- [109] S. Klainermann, A. Majda, Compressible and incompressible fluids, *Communications on Pure and Applied Mathematics* 35 (1982) 629–651.
- [110] R. Klein, N. Botta, T. Schneider, C. Munz, S. Roller, A. Meister, L. Hoffmann, T. Sonar, Asymptotic adaptive methods for multi-scale problems in fluid mechanics, *Journal of Engineering Mathematics* 39 (2001) 261–343.
- [111] C. Munz, S. Roller, R. Klein, K. Geratz, The extension of incompressible flow solvers to the weakly compressible regime, *Computers and Fluids* 32 (2003) 173–196.
- [112] C. Munz, M. Dumbser, S. Roller, Linearized acoustic perturbation equations for low Mach number flow with variable density and temperature, *Journal of Computational Physics* 224 (2007) 352–364.
- [113] S. Jin, Z. Xin, The relaxation schemes for systems of conservation laws in arbitrary space dimensions, *Communications on Pure and Applied Mathematics* 48 (1995) 235–277.
- [114] C. Buet, B. Després, Asymptotic preserving and positive schemes for radiation hydrodynamics, *Journal of computational Physics* 215 (2) (2006) 717–740.
- [115] E. Burman, L. Sainsaulieu, Numerical analysis of two operator splitting methods for an hyperbolic system of conservation laws with stiff relaxation, *Computer Methods in Applied Mechanics and Engineering* 128 (1995) 291–314.
- [116] L. Pareschi, G. Russo, Implicit-explicit Runge-Kutta schemes for stiff systems of differential equations, *Advances in the Theory of Computational Mathematics* 3 (2000) 269–288.
- [117] L. Pareschi, G. Russo, Implicit-explicit Runge-Kutta schemes and applications to hyperbolic systems with relaxation, *Journal of Scientific Computing* 25 (2005) 129–155.
- [118] S. Jin, L. Pareschi, G. Toscani, Uniformly accurate diffusive relaxation scheme! for multiscale transport equations, *SIAM Journal on Numerical Analysis* 38 (3) (2001) 913–936.
- [119] G. Naldi, L. Pareschi, Numerical schemes for hyperbolic systems of conservation laws with stiff diffusive relaxation, *SIAM Journal on Numerical Analysis* 37 (4) (2000) 1246–1270.
- [120] G. Chen, C. Levermore, T. Liu, Hyperbolic conservation laws with stiff relaxation terms and entropy, *Communications on Pure and Applied Mathematics* 47 (6) (1994) 787–830.
- [121] M. Dumbser, D. S. Balsara, E. F. Toro, C. D. Munz, A unified framework for the construction of one-step finite-volume and discontinuous Galerkin schemes, *Journal of Computational Physics* 227 (2008) 8209–8253.
- [122] H. Schlichting, K. Gersten, *Grenzschichttheorie*, Springer Verlag, 2005.
- [123] V. A. Titarev, E. I. Romenski, E. F. Toro, MUSTA-type upwind fluxes for non-linear elasticity, *International Journal for Numerical Methods in Engineering* 73 (2008) 897–926.
- [124] R. Becker, Stosswelle und Detonation, *Physik* 8 (1923) 321.
- [125] A. Bonnet, J. Luneau, *Aérodynamique. Théories de la dynamique des fluides*, Cepadues Editions, Toulouse, 1989, ISBN: 2.85428.218.3.
- [126] J. B. Bell, P. Coletta, H. M. Glaz, A second-order projection method for the incompressible Navier-Stokes equations, *Journal of Computational Physics* 85 (1989) 257–283.
- [127] M. Tavelli, M. Dumbser, A staggered space-time discontinuous Galerkin method for the incompressible Navier-Stokes equations on two-dimensional triangular meshes, *Computers and Fluids* 119 (2015) 235–249.
- [128] M. Tavelli, M. Dumbser, A staggered semi-implicit discontinuous Galerkin method for the two dimensional incompressible Navier-Stokes equations, *Applied Mathematics and Computation* 248 (2014) 70–92.
- [129] M. Tavelli, M. Dumbser, A staggered space-time discontinuous Galerkin method for the three-dimensional incompressible Navier-Stokes equations on unstructured tetrahedral meshes, *Journal of Computational Physics* 319 (2016) 294 – 323.
- [130] H. Schlichting, K. Gersten, *Boundary-Layer Theory*, Springer, 2018.
- [131] U. Ghia, K. N. Ghia, C. T. Shin, High-Re solutions for incompressible flow using Navier-Stokes equations and multigrid method, *Journal of Computational Physics* 48 (1982) 387–411.
- [132] M. Tavelli, M. Dumbser, A pressure-based semi-implicit space-time discontinuous Galerkin method on staggered unstructured meshes for the solution of the compressible Navier-Stokes equations at all Mach numbers, *Journal of Computational Physics* 341 (2017) 341–376.
- [133] B. van Leer, Towards the ultimate conservative difference scheme V: A second order sequel to Godunov’s method, *Journal of Computational Physics* 32 (1979) 101–136.
- [134] M. Dumbser, V. Casulli, A staggered semi-implicit spectral discontinuous galerkin scheme for the shallow water equations, *Applied Mathematics and Computation* 219 (15) (2013) 8057–8077.
- [135] F. Fambri, M. Dumbser, Spectral semi-implicit and space-time discontinuous Galerkin methods for the incompressible Navier-Stokes equations on staggered Cartesian grids, *Applied Numerical Mathematics* 110 (2016) 41–74.
- [136] F. Fambri, M. Dumbser, Semi-implicit discontinuous Galerkin methods for the incompressible Navier-Stokes equations on adaptive staggered Cartesian grids, *Computer Methods in Applied Mechanics and Engineering* 324 (2017) 170–203.
- [137] M. R. Baer, J. W. Nunziato, A two-phase mixture theory for the deflagration-to-detonation transition (DDT) in reactive granular materials, *J. Multiphase Flow* 12 (1986) 861–889.
- [138] R. Saurel, R. Abgrall, A Multiphase Godunov Method for Compressible Multifluid and Multiphase Flows, *Journal of Computational Physics* 150 (1999) 425–467.
- [139] R. Saurel, R. Abgrall, A Simple Method for Compressible Multifluid Flows, *SIAM Journal on Scientific Computing* 21 (1999) 1115–1145.
- [140] G. Perigaud, R. Saurel, A compressible flow model with capillary effects, *Journal of Computational Physics* 209 (2005) 139–178.
- [141] E. Romenski, A. Resnyansky, E. Toro, Conservative hyperbolic formulation for compressible two-phase flow with different phase pressures and temperatures, *Quarterly of Applied Mathematics* 65 (2007) 259–279.

- [142] E. Romenski, D. Drikakis, E. Toro, Conservative models and numerical methods for compressible two-phase flow, *Journal of Scientific Computing* 42 (2010) 68–95.